Determining the atmospheric composition of the ultra-hot Jupiter WASP-178b with ESPRESSO

Yuri Damasceno
Master's Degree in Astrophysics and Astronomy
Department of Physics and Astronomy
Faculty of Sciences of the University of Porto
2024

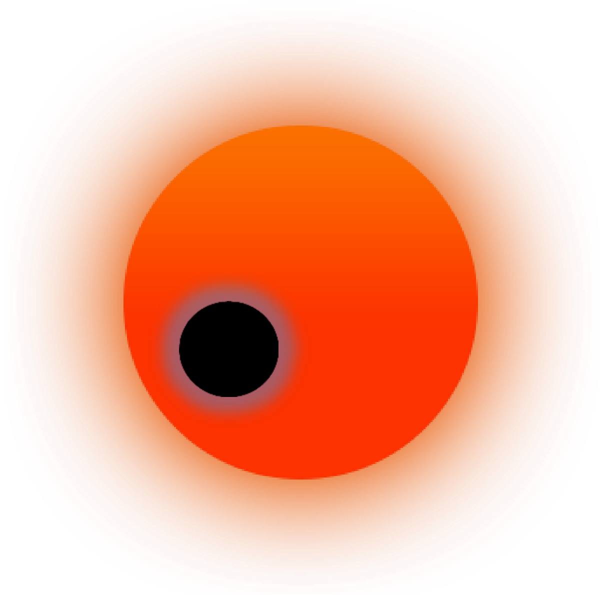

Determining the atmospheric composition of the ultra-hot Jupiter WASP-178b with ESPRESSO

Yuri Damasceno

Dissertation carried out as part of the Master's Degree in Astronomy and Astrophysics

Department of Physics and Astronomy

2024

Supervisor

Julia Seidel, Dr., European Southern Observatory

Co-supervisor

Nuno Santos, Prof. Dr., Faculty of Sciences of the University of Porto, Instituto de Astrofísica e Ciências do Espaço

UNIVERSITY OF PORTO

MASTER'S THESIS

Determining the atmospheric composition of the ultra-hot Jupiter WASP-178 b with ESPRESSO

Author:
Yuri DAMASCENO

Supervisor:
Dr. Julia SEIDEL

Co-supervisor:
Prof. Dr. Nuno SANTOS

A thesis submitted in fulfilment of the requirements
for the degree of MSc. Astronomy and Astrophysics

at the

Faculty of Sciences of the University of Porto
Department of Physics and Astronomy

July 14, 2024

Acknowledgements

The achievements accomplished during this project are largely thanks to a set of people without whom this would not be the same. My immense gratitude goes to Dr. Julia Seidel, Dr. Nuno Santos and Bibiana Prinoth for their unconditional support and guidance throughout the entire process and for believing in me. I am thankful to the people from IA/CAUP, ESO Santiago and the ESPRESSO consortium for having received me with open arms.

I am grateful to the close friends I've made throughout this journey who always found reason for laughter in the peaks of tension and in times of confinement. It is needless to state this would never be possible without the support and incentive of my family in every front. I reserve a separate gratitude towards my parents, who raised and cheered me on the whole way, and towards my girlfriend, who never seized to make me go after my goals and encouraged me to get into this adventure to begin with.

Acknowledgements are owed to the European Union for funding this project (ERC, FIERCE, 101052347). Views and opinions expressed are however those of the author(s) only and do not necessarily reflect those of the European Union or the European Research Council. Neither the European Union nor the granting authority can be held responsible for them. This work was supported by FCT - Fundação para a Ciência e a Tecnologia through national funds and by FEDER through COMPETE2020 - Programa Operacional Competitividade e Internacionalização by these grants: UIDB/04434/2020; UIDP/04434/2020.

UNIVERSITY OF PORTO

Resumo

Faculty of Sciences of the University of Porto

Department of Physics and Astronomy

Mestrado em Astronomia e Astrofísica

Determinação da composição atmosférica do Júpiter ultra-quente WASP-178 b com o ESPRESSO

por Yuri DAMASCENO

Os avanços observados no ramo de sistemas planetários nos seus anos de vida recentes têm sido surpreendentes. Desde a primeira deteção de um exoplaneta em torno de uma estrela como o Sol, há quase 30 anos, até à primeira deteção de uma atmosféra num exoplaneta ainda neste século, foram descobertos milhares de outros mundos, dezenas dos quais com atmosferas confirmadas. O estudo das atmosferas dos exoplanetas passou da observação de absorção ampla de sódio à busca detalhada de inúmeras espécies atómicas e moleculares e à compreensão da dinâmica atmosférica e de ventos, impulsionada pela ambição humana, bem como por enormes saltos em ambos instrumentos terrestres como espaciais.

Estudar a atmosfera de um planeta fornece informações sobre a sua composição e comportamento que, segundo se prevê, estão ligados a teorias de formação planetária, evaporação planetária, propriedades estelares e inclusivamente à busca por vida fora da Terra. Desenvolver este ramo recente e em expansão das ciências planetárias é, portanto, imperativo de forma a obter informações sobre alguns dos seus enigmas mais intrigantes. Com isto em mente, fazemos uma revisão do método principal para estudar atmosferas de exoplanetas, a espectroscopia de transmissão, explorando os seus sucessos, desenvolvimentos, obstáculos e fraquezas. Em seguida, utilizamos este método para analisar a composição e as propriedades da atmosfera do Júpiter ultra-quente WASP-178 b visto pelo espectrógrafo de alta resolução de última geração ESPRESSO e do telescópio de 8-m ESO-VLT. Em particular, procuramos as assinaturas de absorção de magnésio, sódio, hidrogénio e lítio e utilizamos as suas propriedades observadas para inferir o comportamento geral da atmosfera.

Conseguimos detectar a presença de hidrogénio e sódio nas camadas superiores da atmosfera, com uma deteção possível de magnésio e uma não-deteção de lítio. Os resultados revelaram dinâmica atmosférica diferencial com a altura, com uma possível perda atmosférica ligeira de hidrogénio. As conclusões deste trabalho fornecem uma motivação clara para futuras observações de alta resolução do WASP-178 b, abrindo caminho para um futuro projeto de doutoramento na área.

UNIVERSITY OF PORTO

Abstract

Faculty of Sciences of the University of Porto
Department of Physics and Astronomy

MSc. Astronomy and Astrophysics

Determining the atmospheric composition of the ultra-hot Jupiter WASP-178 b with ESPRESSO

by Yuri DAMASCENO

The advancements seen in the planetary systems branch over its recent years have been astounding. Since the first exoplanet detection nearly 30 years ago to the first atmospheric detection in this century, thousands more have been discovered, hundreds of those with detected atmospheres. The study of exoplanet atmospheres has gone from the observation of broad sodium absorption to the detailed search for a multitude of atomic and molecular species and an understanding of atmospheric dynamics and winds, impulsed by human ambition as well as by great leaps in both ground- and space-based instruments.

Studying a planet's atmosphere provides information regarding its composition and behaviour which has been predicted to link to planet formation theories, planet evaporation, stellar properties and even the search for life beyond Earth. It is thus imperative to develop this recent and booming branch of planetary sciences to gain insight into some of its most puzzling problems. With this in mind, we take a look at the principal method to study exoplanet atmospheres, the transmission spectroscopy, exploring its successes, developments, challenges and shortcomings. We then employ this method to analyse the composition and properties of the atmosphere of the ultra-hot Jupiter WASP-178 b through the eyes of the state-of-the-art high-resolution spectrograph ESPRESSO and the 8-m class ESO-VLT telescopes. In particular, we search for the absorption signatures of magnesium, sodium, hydrogen and lithium and use their observed properties to infer the general behaviour of the atmosphere.

We were able to detect the presence of hydrogen and sodium high up in the atmosphere, with a tentative detection of magnesium and a non-detection of lithium. The

results revealed differential atmospheric dynamics with height, with a possible slight atmospheric escape from hydrogen. This work's conclusions provide a clear motivation for further high-resolution observations of WASP-178 b, laying the path for a future PhD project.

Contents

List of Figures

Glossary

au	Astronomical unit
amu	Atomic mass unit
BERV	Barycentric Earth RV
CCD	Charge-coupled device
CCF	Cross-correlation function
DRS	Data Reduction Software
FWHM	Full width at half-maximum
HR	High resolution
ISM	Interstellar medium
LDC	Limb darkening coefficients
LOS	Line of sight
MR	Medium resolution
NUV	Near ultraviolet
PRF	Planetary rest-frame
RV	Radial velocity
S/N	Signal-to-noise ratio
SRF	Stellar rest-frame
SSB	Solar System barycentre
UHJ	Ultra-hot Jupiter
UHR	Ultra-high resolution
UT	Unit telescope

VLT Very large telescope

Chapter 1

Introduction

The wonder about where we came from and how all that we know has come to exist is but a small sample of thoughts that impulsed the expansion of astronomy. When fueled by its curiosity, humanity has proved capable of remarkable achievements, having sent centimetre-sized satellites to the nearby star Alpha Centauri, probed all planets in the Solar System and even planning to build radio telescopes on the moon. The question of whether there is life outside of Earth might be one of humanity's most profound wonders. We are in a transition age where searching for signs of life on other planets has become possible driven by advancements in instrumentation, knowledge and international cooperation. Searching for signs of biology outside our home involves several fields, starting with the study of the planets themselves. With over 5000* planets found beyond the Solar System, the focus has shifted towards the robust characterisation of these worlds, which is an indispensable step for studying more complex aspects. An absolutely essential component for the characterisation of planets is their atmosphere, as it has the ability to affect the environment radically. Examples of this lie very close to home. In the Solar System, all planets but Mercury possess an atmosphere at their disposal, each with its own bizarre properties. Taking Venus as an example, its high temperature is a consequence of a runaway greenhouse effect due to the high concentration of CO_2 (Adams and Dunham, 1932), making it the hottest planet in our system although it is farther from the Sun than Mercury. On Earth, the proliferation of life, including us, owes its existence to Earth's atmosphere which regulates the temperatures and protects against harmful radiation and small body impacts.

*http://www.exoplanet.eu/

When it comes to planets beyond the Solar System, the great distance makes it difficult to probe the thin sheets of gas surrounding exoplanets, even with current cutting-edge instruments. It is imperative to evolve our techniques alongside our technology, and this means to master the methods used to detect and characterise exoplanet atmospheres, and how they evolved since the beginning.

1.1 Background

The study of exoplanet atmospheres was born with the first successful detection made by Charbonneau et al. (2002) for the hot Jupiter HD 209458 b. This was achieved using data from the Space Telescope Imaging Spectrograph (STIS) on the 2.4-m Hubble Space Telescope (HST), later confirmed by (Snellen et al., 2008). To do so they measured the amount of light received in different wavelength bands and verified the depth of the transit varied by a small value relative to the mean value, in the order of 10^{-3}, around the location of the sodium Fraunhofer lines, in the visible. Following the successful detection of sodium on HD 209458 b came those of hydrogen, oxygen and carbon (Vidal-Madjar et al., 2003, 2004). During the years that followed the first detection, successful atmosphere observations were conducted using space-based telescopes due to the significant and time variable contamination induced by Earth's own atmosphere. Ground-based atmospheric detections saw their beginning when Redfield et al. (2008) detected sodium on HD 189733b using the High Resolution Spectrograph (HRS) on the 9.2 m Hobby-Eberly Telescope, and when Snellen et al. (2008) reached the same conclusions for HD 209458b with the High Dispersion Spectrograph (HDS) on the Subaru telescope. Since then, different techniques were developed to not only detect, but characterise the exoplanetary atmospheres' complex compositions and dynamics. Currently, multiple approaches can be used, each customised to its own purpose and for different kinds of targets. Along with advances in instrumentation and methodology, theoretical formulae have been developed over time to interpret the observations of atmospheric signals (as a non-exhaustive list of references relevant to this thesis, see Ehrenreich et al. (2006, 2012); Wyttenbach et al. (2015); Heng et al. (2015); Pino et al. (2018); Seidel, J. V (2021); Azevedo Silva et al. (2022)).

Successfully detecting an exoplanet's atmosphere involves a series of concepts which are necessary to extract the atmosphere's faint signal, starting with the planet's observation and characterisation.

1.1.1 Transit Method

Prior to studying an atmosphere comes the proper detection and characterisation of the host planet. Various methods and techniques are used with this objective in mind, such as the transit method. This planet-finding technique saw its first successful detections* with HD 209458 b (Henry et al., 2000; Charbonneau et al., 2000) and is extremely powerful for certain system architectures. A transit occurs when a planet passes between its host star and the observer's line of sight, blocking part of the star's visible surface, which is often refered to as the stellar disk. This method, however, can only be applied to systems where the orbit is seen close to edge-on, which corresponds to an orbital inclination close to $i = 90°$. The transit method consists of measuring the variation of observed flux from the star before, during and after the planet's transit. The amount of light blocked and the duration of the transit provides information on properties of the planet and the system architecture. The duration of the transit informs on the orbital period, P, which relates to the semi-major axis, a, and the system's mass, M, through Kepler's third law (Equation 1.1). Longer period orbits will result in longer transits.

$$\frac{P^2}{a^3} = \frac{4\pi^2}{GM} \tag{1.1}$$

The depth δ relates to the amount of light blocked by the planet's opaque disk. Considering the simple case of a homogeneously luminous stellar disk, the maximum relative depth would be the surface area blocked by the planet, given by equation 1.2, where R_p and $R_\star$ are the radii of the planet and star, L represents the luminosity of the star and ΔL is the difference in luminosity during transit.

$$\delta = \frac{\Delta L}{L} \propto \frac{R_p^2}{R_\star^2} \tag{1.2}$$

Since the depth corresponds to the relative amount of light blocked behind the planet this means it is affected by any stellar variation or effects happening in the area covered during transit. The previous depth relation presented thus serves as a crude approximation of reality since there are several effects and brightness variations throughout the stellar disk that affect the shape of the light curve. One of these effects is the limb darkening (de Pater and Lissauer, 2015), where the edges of the star's disk are slightly dimmer than the central region, usually described using a quadratic polynomial approximation.

*HD 209458 b was detected before using the radial velocities method by Henry et al. (2000)

Other effects that might be important to consider depending on the star and system architecture include the limb darkening as well as active regions, which will be discussed further along this thesis. A more detailed description of the lightcurve's shape modelling can be found in Winn et al. (2008).

From photometric observations, we would observe a curve similar to that illustrated in Figure 1.1. A transit can be characterised by four contact points, T_1 to T_4. Between the first and second contact points, when the planet's disk is not fully in front of the stellar disk, we observe a progressively decreasing flux, in a phase called ingress. The counterpart can be found between the third and fourth contact points, during the egress phase. Between the second and third contact points the entire planet is in front of the stellar disk and in this stage any variation in the lightcurve's depth is related to flux variations throughout the star's surface.

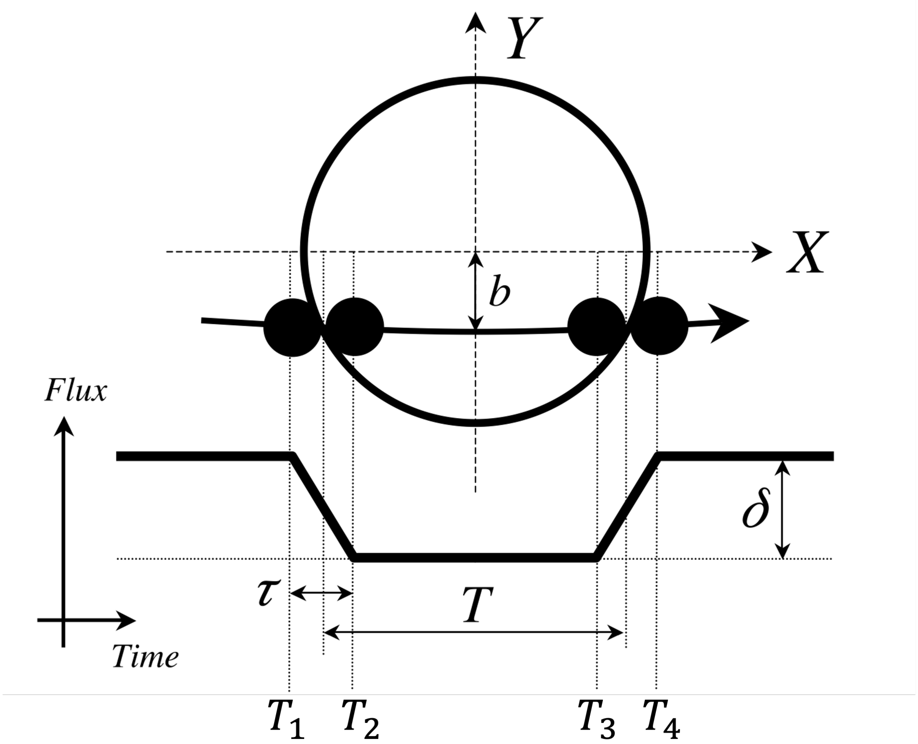

FIGURE 1.1: Adapted Figure 2 from Winn (2010), showing a diagram of a transit. The planet, marked as the dark circle, is shown in the four contact point phases of a transit with an impact parameter b. The reference is placed at the centre of the stellar disk. Beneath is the lightcurve of the transit, with the contact points marked. The transit duration, T, transit depth, δ, and ingress phase, τ, are represented.

The transit method comes with an observational bias, since it only detects planets whose orbits cross the stellar disk in the observers line of sight. This restriction makes some targets easier to detect than others. Assuming that the orbits are randomly oriented in space, we find that smaller orbits have a higher probability $\mathcal{P}$ of being in a transiting configuration, with $\mathcal{P} \propto R_\star/a$. Making use of Equation 1.1, this translates to planets having smaller period orbits being more likely to transit and thus more likely to be detectable through the transit method. Another advantage of smaller period orbits is the higher frequency at which transit events occur, making a detection more likely as well as allowing to record most, if not the entire transit in a single round of observations. The transit method also favours bigger planets with a higher $R_p/R_\star$ ratio, since these would leave a deeper and more noticeable flux variation. Overall the transit method is best at detecting large, Jupiter-sized planets that orbit very close to their stars.

Once the targets are detected they can be characterised via other techniques that take advantage of the abundant information hidden in the light.

1.1.2 Spectroscopy

An extremely powerful way of studying stars and their orbiting planets is by looking at their spectra through spectroscopic measurements. The spectrum of an object can be acquired by exploiting the fact that different wavelengths are refracted, reflected and diffracted differently, meaning that light can be split into its several components. From an object's spectrum we can derive its physical properties, such as the temperature, as well as its composition through the absorption/emission features, and velocity profiles by analysing the position and width of spectral lines imprinted within. In the field of stellar and exoplanetary astronomy, spectroscopy is frequently used for composition, dynamics and activity studies, being a crucial piece for the study of exoplanet atmospheres. Further to this, one of the most bountiful exoplanet detection and characterisation methods, alongside the transit method, is the radial velocities method, which is often used together with the transit method to provide complementary information and a more complete planet characterisation. This method requires spectra measurements to determine the average Doppler shift of the entire stellar spectrum with time and translate this shift into a velocity in the line of sight (Santos et al., 2020).

One of the main characteristics of a spectrograph is its spectral resolution, expressed as $\mathcal{R} = \lambda/\Delta\lambda$, which describes the instrument's ability to distinguish between two wavelengths separated by $\Delta\lambda$. The resolution is related to the dispersion since a higher dispersion corresponds to a higher separation in the wavelength direction (also called the dispersion direction). A higher resolution instrument is capable of resolving finer structures in the spectra and variations induced in it. On the other hand, a higher resolution means a smaller interval of the spectra is available. When considering narrow features, such as atomic lines, high-resolution is a necessity to be able to measure the line shape properly and to extract information from it. One of the most powerful instruments currently in use for high-resolution spectroscopy is the Echelle SPectrograph for Rocky Exoplanets and Stable Spectroscopic Observations (ESPRESSO).

1.1.2.1 ESPRESSO Instrument

The ESPRESSO instrument is an ultra-stable, high-resolution spectrograph installed at the Paranal Observatory and connected to the Very Large Telescope (VLT). ESPRESSO is capable of capturing light from one or all four of the VLT telescopes, producing spectra with a resolution between 70.000 and 190.000, depending on the mode it is used on (Pepe et al., 2021). The spectral resolution, $\mathcal{R}$, is defined by the smallest wavelength interval that can be distinguished in a measurement, $\Delta\lambda$, at a wavelength λ. The resolution is thus given by $\mathcal{R} = \lambda/\Delta\lambda$. ESPRESSO operates mainly in the visible band, specifically in the wavelength range 380-788 nm. The extreme stability and resolution this instrument provides allow for ultra-precise radial velocity measurements (at the level of 10 cm s^{-1}) and for accurate resolution of thin spectral lines. The instrumental line broadening of ESPRESSO is 2 km s^{-1}, while its very stable charge-coupled device (CCD) detector has a pixel size of 500 m s^{-1}. Combined with the light-gathering power of the VLT 8-m telescopes, ESPRESSO was designed with the ultimate goal of detecting Earth-like planets in the habitable zone of Sun-like stars, which is equivalent to detecting an RV signal with a 10 cm s^{-1} semi-amplitude.

ESPRESSO is the only high-resolution instrument that is able to make observations connected to all four unit telescopes (UT), and in such configuration operates with a light collecting power equivalent to that of a 16-m telescope. The spectra can be measured in three different modes: 1-UT Ultra-High Resolution (Single-UHR), 1-UT High Resolution (Single-HR) and the 4-UT Medium Resolution (Multi-MR). The difference between the modes is the equivalent fibre size, which doubles between 70 μm for UHR, 140 μm for HR and 280 for μm MR. This doubling of the fibre width reduces the resolution, however it increases the signal. The choice of operating mode depends on the particular goal of the observations. While UHR was made to achieve an extremely large spectral resolution it is the one with the least signal-to-noise ratio (S/N). On the other hand the MR setting presents the highest signal, as it is operated with all four UT telescopes, compromising resolution for such and being more adequate for fainter targets. The HR mode is a compromise between resolution and signal, made for precise RV measurements. The pupil slicer, an optical component within ESPRESSO, is responsible for slicing the pupil of light into two nearly identical portions. This results in a virtually doubled number of orders, since the real number of orders with a different wavelength range are all divided into two slices. This division of the pupil allows for the observation of brighter targets for longer without saturating the detector. For a more extensive description of ESPRESSO we refer to the ESPRESSO user manuals *.

ESPRESSO has a large impact on exoplanet research, by providing spectra and RV measurements with extreme precision. This is as well crucially valuable for the study of exoplanet atmospheres, since by resolving narrow lines we may detect and analyse specific features and infer the characteristics of the environment in which these features are formed.

1.2 Exoplanetary Atmospheres

Since the first atmosphere detection and with the rise of stable instruments, such as ESPRESSO, the field has grown vastly. The detection and afterwards the characterisation of exoplanetary atmospheres have been used to infer the dynamics and properties of the environment (Wyttenbach et al., 2015; Seidel et al., 2023). Unfortunately, it is far more difficult to analyse atmospheres with distance, as they become nearly impossible to spatially resolve. Furthermore, the presence of thick clouds and hazes acts as a barrier for all wavelengths of light, essentially becoming indistinguishable from the opaque planetary disk (Deming et al., 2013; Sing et al., 2013). Due to these factors, not all exoplanets are suitable for atmospheric detection and analysis. In order to retrieve information, light must be able to pass through the atmosphere without being completely blocked, meaning it cannot be fully opaque. Elements such as clouds and hazes can act as opaque layers, since they block light across the spectrum, and so can be confused with the planet's body. It should also not be too thin as in this case the signal would be too faint to detect. Having this in mind, we ideally require planets with an extended atmosphere above clouds and other opaque layers of the atmosphere. These conditions can be achieved with high temperatures, as

*https://www.eso.org/sci/facilities/paranal/instruments/espresso/doc.html the molecules that form thick clouds and hazes would be dissociated into atomic or ionized form and the high kinetic energy would drive the atmosphere outwards, providing more detectable surface area. Among the most commonly detected species in exoplanet atmospheres are atomic sodium (e.g. Snellen et al. (2008); Wyttenbach et al. (2015)), water (e.g. Deming et al. (2013); McCullough et al. (2014)) and CO (e.g. Snellen et al. (2010a); Brogi et al. (2016)).

Grounded by the limited information we can extract from a great distance, an atmosphere composed of an ideal gas in hydrostatic equilibrium is often assumed, which gives the vectorial Equation 1.3, where $\mathbf{p}$ is the pressure, ρ is the gas density and $\mathbf{g}$ is the gravitational acceleration.

$$\nabla \mathbf{p} = -\rho \mathbf{g} \tag{1.3}$$

Considering the surface gravity is purely vertical and taking on the vertical altitude component of Equation 1.3, these assumptions allow us to describe the pressure p at a height h in terms of the particles' mass m, the temperature T and the gravitational acceleration g. This is expressed in Equation 1.5, considering the general case of an altitude dependent temperature $T(h')$.

$$\frac{dp}{dh} = -\rho g \tag{1.4}$$

$$p(h) = p(h=0)e^{\int_{h'=0}^{h'=h} \frac{mg}{k_B T(h')} dh'} \tag{1.5}$$

It is usual to assume a temperature profile in order to fulfill the integral expressed in Equation 1.5, the most elementary being a constant temperature with altitude, giving rise to Equation 1.6.

$$p(h) = p(h=0)e^{\frac{mg}{k_B T}h}$$

$$p(h) = p(h=0)e^{\frac{h}{H}} \tag{1.6}$$

This approximation is not entirely accurate since the temperature is known to vary with altitude, as has been found observationally (Wyttenbach et al., 2015; Heng et al., 2015), however it is still capable of crudely describing observations and serves as a ground level from which more sophisticated studies can be conducted. It is frequent to define the scale height quantity $H = \frac{k_B T}{gm}$ which, in hydrostatic equilibrium, represents the height at which the pressure decreases by a factor of e. This relation can be obtained in an equivalent way for the gas density ρ.

The composing elements can be found distributed through different layers in the atmosphere. Generally, lighter elements reside higher up in the atmosphere, such as H and He, while heavier atoms and molecules remain mostly in the lower layers, for instance Fe or CO (see e.g. Azevedo Silva et al. (2022)). This stratification is used to probe different regions of the atmosphere via the detection of different elements. On top of this, the strength of the lines determines the region they probe, with weaker lines revealing more the lower layers and stronger lines probing higher up. For instance, the atomic lithium resonance doublet is weaker than the sodium Fraunhofer lines (or D doublet) so the sodium atoms will absorb light far more efficiently at high altitudes, despite lithium being lighter and likely more abundant higher up than sodium. For this reason, the sodium absorption lines are used to probe the upper layers and the lithium lines for the lower ones. The existence of certain chemical species also provides an indication on physical properties with height. The detection of ionised iron Fe II, for example, is expected for regions where the temperature is above 3000 K, at which absorption from Fe II starts becoming significant (Prinoth et al., 2023).

At high temperatures, the target planet's mass also matters as its gravitational pull determines how hot it can get before beginning to lose its atmosphere through atmospheric escape. A threshold for atmospheric loss to happen can be set using the balance between the escape velocity and the velocity profile of the gases contained in the atmosphere. The escape velocity v_{esc} is defined, as stated in Equation 1.7, by the mass of the planet M_p, and the altitude at which the object attempting escape is, given by the sum of the planet's radius R_p and the altitude h above.

$$v_{esc} = \sqrt{\frac{2GM_p}{(R_p + h)}} \tag{1.7}$$

On the other hand, the most likely speed v_p of a gas that follows a Maxwell-Boltzmann distribution is given by Equation 1.8, in terms of the temperature of the gas T, the mass m of the particles composing the gas and the Boltzmann constant k_B.

$$v_p = \sqrt{\frac{2k_B T}{m}} \tag{1.8}$$

These two quantities give us an idea of the conditions at which atmospheric escape becomes more likely. If the temperature is too high, the average velocity of the gas particles in the upper layers, occupied by lighter elements such as hydrogen, can surpass the planet's escape velocity and thus these layers are stripped from the atmosphere. This phenomenon can also be caused by the host star's radiation pressure, mainly for planets orbiting close to their stars, in a process usually designated atmospheric evaporation which has been observed to occur, for example, in HD 189733 b (Lecavelier Des Etangs et al., 2010; Bourrier et al., 2013). Considering this, a combination of hot and massive provides the ideal targets for exoplanet atmospheric studies: enter the hot Jupiter and ultra-hot Jupiter families of exoplanets.

1.2.1 Ultra-hot Jupiters

Ultra-hot Jupiters (UHJ) are a class of exoplanets characterised by having a size and mass similar to those of Jupiter, however orbiting extremely close to their host star, with periods below three days (Gaudi et al., 2005) and temperatures around and above 2000 K (Parmentier et al., 2018). A planet this close to its star will have very high temperatures due to the extremely high irradiation which drive their atmospheres high up, making them bloated and very desirable for atmospheric studies. These planets, due to their high mass, are also not expected to lose their atmospheres as easily compared to lower-mass planets. UHJ, therefore, appear as ideal targets for atmospheric studies, such that several techniques were developed using data from UHJ observations, including the detection of multiple chemical species (Hoeijmakers et al., 2019; Borsa et al., 2021; Prinoth et al., 2022), the observation of atmospheric dynamics (Borsa et al., 2019; Ehrenreich et al., 2020; Seidel et al., 2020a, 2023), the retrieval of abundances (Gandhi et al., 2022; Gibson et al., 2022) and the detection of emission (Pino et al., 2020, 2022).

The study of planets this close to their host stars brings a set of restrictions to the problem. Their rotation is tidally locked to their orbit around the star and these are practically circular (but see e.g. Correia and Robutel (2013)). Tidal locking implies half of the planet's surface is constantly facing the star while the other remains in permanent night. This creates a steep temperature gradient between the hot dayside and the cold nightside, which influences the dynamics of the atmosphere. We can expect the dayside to be more extended or bloated with several species condensing on the transition region or terminator in some cases. Due to the differential atmospheric extension, we can also expect to probe different regions of the atmosphere throughout the transit. The two terminators are designated the morning or leading terminator, which is the first to intersect the stellar disk during transit, and the evening or trailing terminator. During the ingress phase, the transmitted light will be predominantly from the redshifted morning terminator while the transmission will be dominated by the blueshifted evening terminator during egress, with the centre of transit having approximately equal contributions. We can determine at which phases of the orbit transit will begin and end, taking advantage of the fact the orbit is circular, via Equations 1.9 and 1.10.

$$\alpha_1 = -\alpha_4 = -\arcsin\left(\frac{\sqrt{(R_\star - R_p)^2 - (bR_\star)^2}}{a}\right) \tag{1.9}$$

$$\alpha_2 = -\alpha_3 = -\arcsin\left(\frac{\sqrt{(R_\star + R_p)^2 - (bR_\star)^2}}{a}\right) \tag{1.10}$$

Each angle α_i corresponds to the orbital angle of its corresponding contact point T_i for a planet with radius R_p orbiting with an impact parameter b at a distance a from the system centre. A representation of this is shown in Figure 1.2.

The atmospheres of UHJ are expected to be dissociated into atomic or ionised components along with certain molecules, mainly H_2O or CO. For these classes of planets it is frequent to take a set of assumptions: that the atmosphere is in hydrostatic equilibrium, local thermodynamic equilibrium (LTE) as well as chemical equilibrium. Assuming hydrostatic equilibrium implies the atmosphere's pressure gradient balances out the planet's gravity, thus globally the atmosphere is static. LTE implies that at small scales the temperature of surrounding fluid is approximately the same, giving locally a null transfer of thermal energy. Lastly, chemical equilibrium entails the abundances are maintained since the chemical reactions and their reverses all occur at the same rate. At high temperatures ($T \gtrsim 2500$ K) it has been verified that LTE is a good representation of the atmospheres' state (Wyttenbach et al., 2020) and chemical equilibrium is also expected (Miguel and Kaltenegger, 2014; Lothringer and Barman, 2019). A downside of UHJ for atmospheric studies is the number of potential targets. With such extreme conditions, only dozens of UHJ are known to transit and have been verified to contain an atmosphere, with the most commonly studied targets being WASP-121 b (Delrez et al., 2016; Azevedo Silva et al., 2022; Seidel et al., 2023), WASP-76 b (West et al., 2016; Tabernero et al., 2021), WASP-189 b

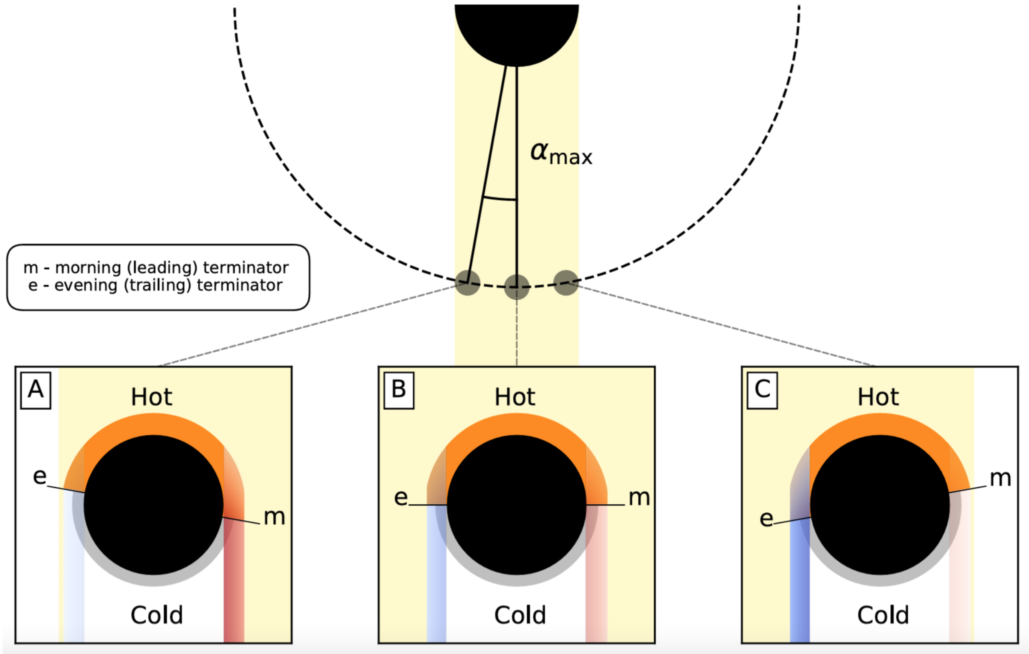

FIGURE 1.2: Figure 1 from Prinoth et al. (2022) showing a schematic of the transmitted light through a transiting hot exoplanet and the contributions from both terminators. A tidally locked and close-in planet will have a significantly hotter dayside hemisphere, marked in orange) and a cooler nightside (marked in grey). During ingress (Panel A) the transmitted light is predominantly from the morning terminator, during egress (Panel C) the dominance passes over to the evening terminator, while at transit centre (Panel B) contributions from both are balanced. Light transmitted from the morning terminator will have a redshift due to the planet's rotation and the evening will appear blueshifted for the same reason. These shifts are represented by the red and blue shades. The intensity of these shades represents their higher contribution at each phase. Here α_{max} corresponds to the second and third contact point angles α_2 and α_3

(Lendl et al., 2012; Prinoth et al., 2022) and KELT-9 b (Gaudi et al., 2017; Hoeijmakers et al., 2018; Borsato et al., 2023). Given the optimal conditions of UHJ for atmospheric observations, different methods and techniques can be employed to draw out complementary information.

1.2.2 Atmosphere detection methods

The detection of an exoplanet's atmosphere is a delicate process as the signals are usually very faint. There are multiple spectroscopy-based ways to detect and analyse an atmosphere, able to probe different regions and can be used to complement each other. The most used methods are transmission, emission and reflectance spectroscopy.

1.2.2.1 Transmission

When a transit occurs and the planet blocks a portion of the star's surface we notice an overall dimming of the observed brightness, as mentioned in section 1.1.1. If we now consider a planet with an atmosphere above, it will further dim the brightness coming from the star. In the same fashion as the transit method, the absorption depth will depend on the projected area of the atmosphere and so this method favours extended atmospheres. In this case, however, since the atmosphere is not fully opaque to all light, we expect it to block light differently across the spectrum depending on the composition and properties of the atmosphere. A schematic of the transmission method is presented in Figure 1.3, showing some light from the star passing through the transiting atmosphere and coming out altered on its way to us.

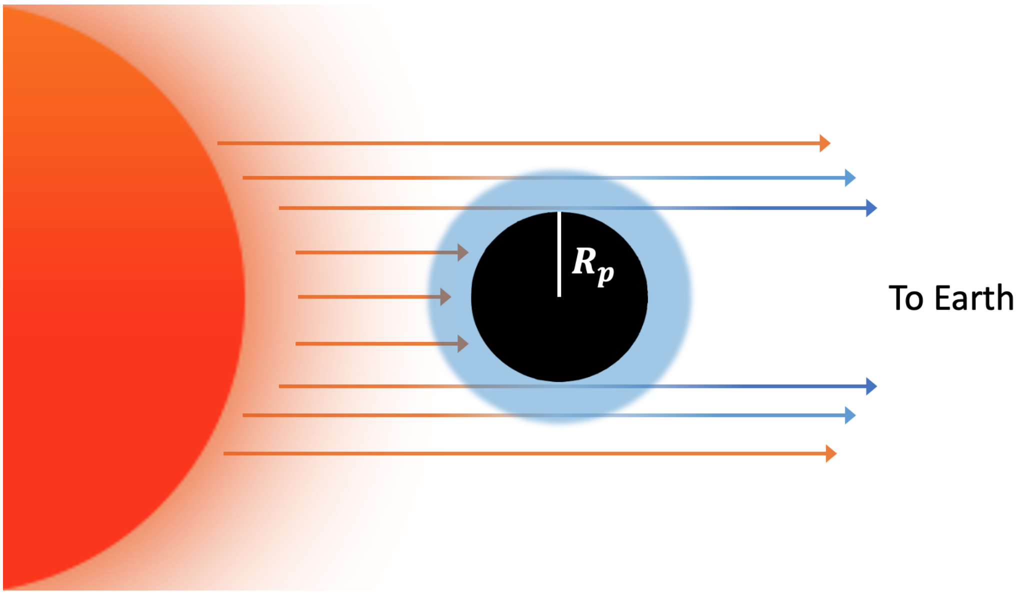

FIGURE 1.3: Schematic of light transmitted through a transiting planet's atmosphere. Some of the light will hit and not cross the opaque planetary disk, represented in black with a radius of R_p, while a portion will cross the atmosphere around the planet. The transmitted light interacts with the atmosphere and comes altered on the other side towards Earth.

To illustrate this, if we consider a planet with only hydrogen there could be an additional absorption from the atmosphere in the hydrogen lines, however not elsewhere, meaning we would observe higher dimming in the hydrogen absorption line wavelength ranges relative to elsewhere in the spectrum. The reason for this is that during the transit the light passes through the atmosphere, which absorbs part of it and imprints the signal from the planet on it in the form of absorption features. Essentially this method is used during a transit event to probe the terminators which are seen as a gas ring attached to the planet's projected disk, as represented in Figure 1.2. Transmission spectroscopy was the method employed in the first exoplanet atmosphere detection by Charbonneau et al. (2002) and is still vastly used. In these observations the planet's nightside is facing us, however, dayside observations can also be made by adopting different strategies.

1.2.2.2 Emission and Reflectance

Emission spectroscopy is a method used to detect and analyse the spectra originated in the target planet's atmosphere. The luminosity of the planet L_p is given by its temperature T_p, via the blackbody emission shown in Equation 1.11. Likewise the luminosity of the star is given by Equation 1.12 in terms of its radius and effective temperature T_{eff}.

$$L_p = 4\pi R_p^2 \sigma T_p^4 \tag{1.11}$$

$$L_\star = 4\pi R_\star^2 \sigma T_{eff}^4 \tag{1.12}$$

The ratio between the two luminosities grows with the radius of the planet and its temperature. Unlike transmission spectroscopy, emission spectroscopy consists of observing the dayside of the planet, right before and after it is occulted behind the star, half an orbit apart from the transit, since this side is the hottest and provides the best scenario for the detection of the atmosphere. In the infrared portion of the spectrum, the planet's spectrum is dominated by its own thermal emission, allowing to derive the properties of the hot dayside (e.g. Deming et al. (2005); Snellen et al. (2010a)).

Reflectance spectroscopy, on the other hand, consists of observing light reflected and scattered off the surface of the planet also during occultation. This component is relevant in the blue wavelengths where the planet's emission is lower and the continuum is associated to scattering processes of the incident stellar light (Madhusudhan et al., 2014). Planetary properties such as the albedo and mass can be determined by observing the spectral lines in the reflected light (Alonso et al., 2009; Rodler et al., 2013; Martins et al., 2015).

By following the methods discussed above, the planet atmosphere's spectrum can be obtained. With these measurements different techniques can be used to analyse the spectral signatures of the atmosphere, each tailored for distinct purposes.

1.2.3 Spectral analysis techniques

Spectral signatures left by elements and molecules vary greatly in shape and amplitude so the same technique may excel at detecting certain chemical species while it fails to detect others. The techniques applied to detecting different species vary depending on the amplitude of the spectral features, the abundance of lines and the abundance and distribution of the elements in cause. The principal ways to analyse the atmosphere's spectrum are through cross-correlation and narrow-band.

1.2.3.1 Cross-correlation

The cross-correlation method is a widely used technique to combine several spectral features in order to create a stronger signal. This technique consists of cross-correlating the observed spectra $\mathcal{F}(\lambda)$ with a model spectrum $\mathcal{M}(\lambda)$, and verifying how well they match. A shift in the wavelength $\Delta\lambda$ is added iteratively to the model spectrum, registering for each $\Delta\lambda$ the value of the cross-correlation as shown in Equation 1.13.

$$\mathrm{CCF}(\Delta\lambda) = \int_{\lambda_0}^{\lambda_1} \mathcal{F}(\lambda')\mathcal{M}(\lambda' + \Delta\lambda)d\lambda' \tag{1.13}$$

The final product is the cross-correlation function (CCF) which shows the match between the two spectra in function of the model's position. Since shifting the spectrum by $\Delta\lambda$ in wavelength corresponds to shifting it by a velocity (discussed in further detail in Chapter 2) the CCF is usually presented in velocity space.

The cross-correlation technique is applied to exoplanet atmospheres for the detection of elements and molecules. This is done by obtaining the CCF between the observed spectra and the model containing a set of features from the chemical species of interest (Snellen et al., 2010b; Hoeijmakers et al., 2020). In case the species exists in the atmosphere we expect to see a peak in the CCF at a shift equal to the radial velocity of the planet since its spectra will be shifted from the rest frame by this value. This technique is particularly useful for sets of weak absorption lines, as these are insufficiently deep and cannot be accurately detected individually in the atmosphere's spectrum. By cross-correlating the data with a template with several weak lines the combined signal will represent an average line with a far higher S/N. A caveat of this process is the loss of information contained in the individual lines due to combining them all together, sacrificing information for signal quality. This technique has been used to detect the presence of, among many, TiO (e.g.

Nugroho et al. (2017); Prinoth et al. (2023)), H_2O (e.g. Birkby et al. (2013, 2017)) and iron (e.g. Hoeijmakers et al. (2018); Ehrenreich et al. (2020); Borsato et al. (2024)).

1.2.3.2 Narrow-band

Another way of looking into the spectrum of an exoplanet's atmosphere is using the narrow-band technique. Unlike in cross-correlation, the narrow-band technique consists of detecting and analysing individual spectral lines from the atmosphere. Narrow-band is more effective for strong enough lines which can be detected individually. Since atmospheric signals are small compared to the star's spectrum, even for the largest features, it is frequent to combine several spectra measured during transit to increase the overall signal, at the cost of losing the temporal information between spectra. This technique is commonly used for various atomic species, such as the Na I D doublet (e.g. Seidel et al. (2019)) and the hydrogen Hα line (e.g. Wyttenbach et al. (2020)), as well as ionised species, such as Ca II H&K (e.g. Tabernero et al. (2021)). This technique will be discussed in further detail throughout this thesis.

1.3 This work

In this thesis, we focus on analysing the transmission spectra to probe the atmosphere of the UHJ WASP-178 b. Our target planet was first detected by Hellier et al. (2019) through transit photometry and its characterisation was complemented by the RV analysis. This planet was also independently discovered by Rodríguez Martínez et al. (2020) as KELT-26b. The host star, WASP-178, is the second hottest exoplanet host star known to date with an effective temperature of 9360 ± 150 K, only dethroned by KELT-9 (Gaudi et al., 2017). WASP-178 is a type A1 IV-V star with a mass of $2.169 \pm 0.089\ M_{\odot}$(Pagano et al., 2023). WASP-178 b is a $1.66 \pm 0.12\ M_J$ planet on a close-in orbit, with an orbital period of only 3.3448371 ± 0.0000011 days and an insolation of $5550^{+1250}_{-630}\ S_{\oplus}$, which puts its equilibrium temperature at 2470 ± 60 K (Hellier et al., 2019). WASP-178 b's high insolation places it among the highest radiation-receiving planets (see Figure 1.4). At such high temperatures and insolation levels, it is expected for WASP-178 b to present a very extended atmosphere, if existent, which makes it an ideal target for atmospheric studies.

We applied narrow-band spectroscopy techniques to a set of two transits observed with ESPRESSO in single-HR mode. We employed a transmission spectroscopy analysis

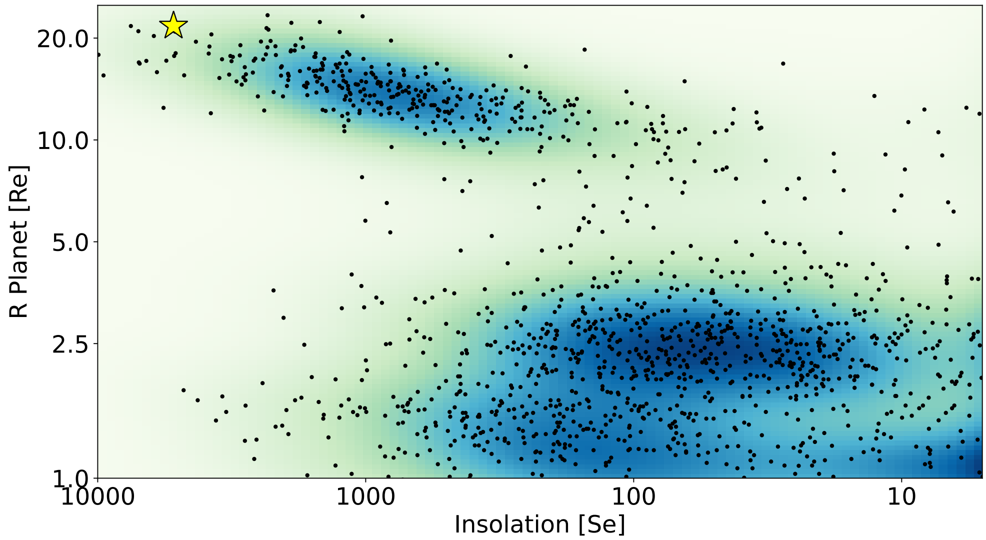

FIGURE 1.4: A subset of discovered exoplanets in a radius vs insolation plot, given in terms of Earth's values. WASP-178 b is marked by the yellow star.

to search for a set of elements in the atmosphere of WASP-178 b. The primary goal of this project was to detect and analyse the Na I Fraunhofer absorption lines. Incentivised by favourable results and progress, the study was expanded to encompass the detection and analysis of the Hα line, the Mg I b triplet and the Li I resonance line. In Chapter 2 we go over the general methodology and principles behind the construction of transmission spectra. We then discuss the data correction steps as well as some of the main obstacles and caveats that required caution in Chapter 3. We then move to Chapter 4 where we cover the application of the previous methods and corrections to our dataset, mentioning the particular challenges associated to them. In Chapter 5 the transmission spectrum absorption results are presented and analysed, leading to the discussion, conclusions as well as future work prospects in Chapter 6.

The results achieved in the elaboration of this thesis have led to a first-author publication in the Astronomy & Astrophysics (A&A) journal while collaborating with the ESPRESSO Consortium. The article, currently revised and resubmitted, counted with the contributions of several researchers, providing a more diverse view on the study of WASP-178 b and presenting further results and conclusions than those obtained for this thesis. On the other hand, the work presented in this thesis is more focused on the narrow-band detection and analysis of a selection of atomic elements, delving into it at a finer level of detail and further extension.

Chapter 2

Transmission spectroscopy principles

A series of procedures are necessary to optimize the data for atmospheric signal detections. In the current Chapter, we discuss the basis principles of transmission spectroscopy and how they are used to extract the planetary signals and optimize the transmission spectrum's quality. The methodology described in this Chapter can be found more in detail in Wyttenbach et al. (2015); Seidel et al. (2019).

2.1 Doppler shifting and reference frames

Considering a wave emitted from its source with a wavelength λ_e, the observed wavelength, λ_{obs}, can appear deviated from its original value due to the relative movement between the source and the observer. If we take the velocity vector of the source relative to the observer to be $\boldsymbol{u}$ and the line of sight (LOS) versor as $\hat{\boldsymbol{l}} = \frac{\boldsymbol{l}}{|\boldsymbol{l}|}$, the wavelength of a wave with a propagation speed of v measured by the observer is given by Equation 2.1.

$$\lambda_{obs} = \lambda_e \sqrt{\frac{1 + \frac{\boldsymbol{u}\cdot\hat{\boldsymbol{l}}}{v}}{1 - \frac{\boldsymbol{u}\cdot\hat{\boldsymbol{l}}}{v}}} \tag{2.1}$$

From this relation, the Doppler effect is a consequence of the component of the velocity parallel to the LOS ($\boldsymbol{u} \cdot \hat{\boldsymbol{l}} \neq 0$). Focusing on the case of an electromagnetic wave, such that $v = c$ with c representing the speed of light in vacuum, and defining the radial velocity as $u_r = \boldsymbol{u} \cdot \hat{\boldsymbol{l}}$, the resulting effect is as shown in Equation 2.2.

$$\lambda_{obs} = \lambda_e \sqrt{\frac{1 + \frac{u_r}{c}}{1 - \frac{u_r}{c}}} \tag{2.2}$$

For each wavelength λ_e we observe a shift $\Delta\lambda = \lambda_{obs} - \lambda_e$ which relates to the relative radial velocity of the light source, thus considering an entire spectrum. This entails a global shift, which is larger for higher wavelengths.

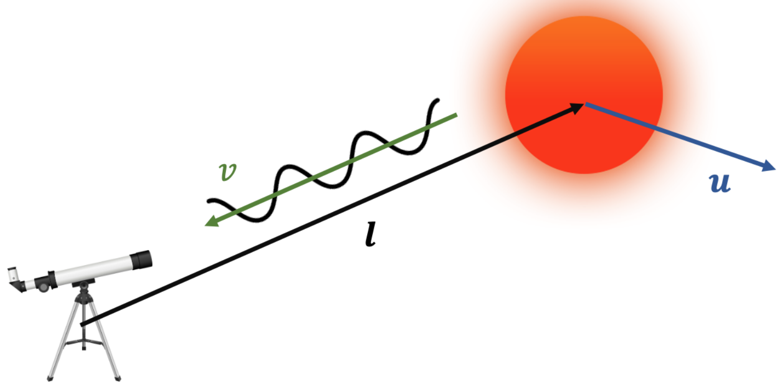

FIGURE 2.1: Schematic of a moving wave source relatively to the observer. The represented quantities are the velocity vector of the source, $\boldsymbol{u}$, the magnitude of the wave propagation velocity v and the LOS, shown as $\boldsymbol{l}$. The direction of the source is given by the versor of $\boldsymbol{l}$.

In the context of transmission spectroscopy of exoplanet atmospheres, the characteristic velocities, in the order of 100 $\mathrm{km\,s^{-1}}$, do not justify the inclusion of relativistic corrections. In fact, owing to the low velocities, such that $u_r/c \ll 1$, we can reasonably consider the first-order approximation, which greatly simplifies the expression for the Doppler effect. The approximated expression for small velocities is shown in Equation 2.3.

$$\lambda_{obs} = \lambda_e \left(1 + \frac{u_r}{c}\right) \tag{2.3}$$

The Doppler effect is an indispensable concept for transmission spectroscopy studies. In order to combine spectra and amplify the desired signal these need to be properly aligned which implies a careful consideration of all Doppler shift components, from the reference frame of the observer (Earth) to the reference frame of the target planet. This reference frame conversion involves correcting for Earth's movement around the Solar System barycentre (SSB) through the barycentric Earth RV (BERV) at the time of observation. From the SSB, we transfer over to the target system's barycentre through the systemic velocity and finally using the stellar and planetary orbital or Keplerian velocities to enter the Stellar Rest Frame (SRF) or the Planetary Rest Frame (PRF). A schematic illustrating the reference frame shifts needed in transmission spectroscopy is shown in Figure 2.2.

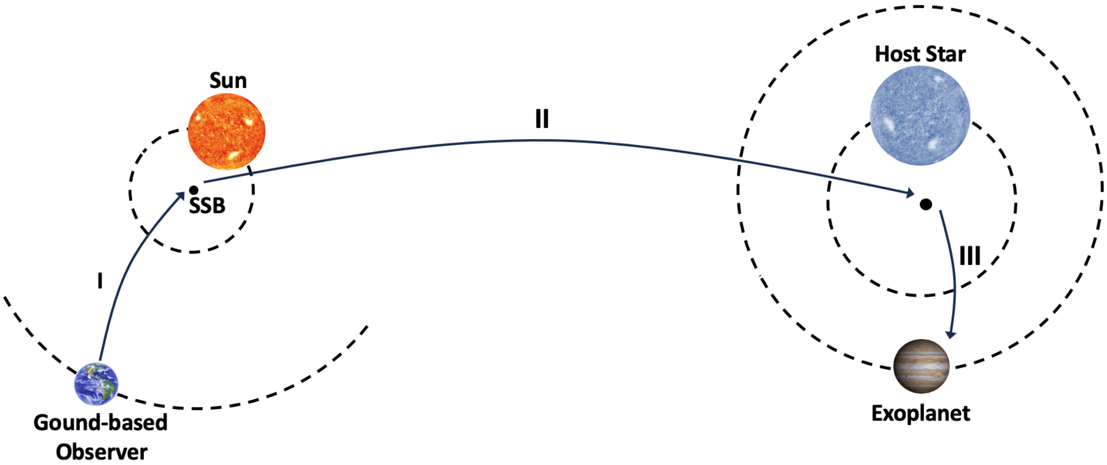

FIGURE 2.2: Adapted from Figure 1.9 from Seidel, J. V (2021). Schematic of reference frame shifts relevant for transmission spectroscopy. **I)** Correction of the Earth's movement around the SSB via the BERV. **II)** Shift to the reference frame of the target system's barycentre via the systemic velocity. **III)** Shift to the planetary rest frame using the derived orbital velocities.

The barycentric correction, which puts the frame of reference from the Earth to the SSB, takes into account Earth's velocity in the line of sight to the target during its orbital motion. The systemic velocity, v_{sys}, corresponds to the velocity between the two systems' barycentres. The next step involves passing from the target system barycentre to the star or planet via the orbital radial velocity derived from their Keplerian motion. In the case of short-period planets, such as UHJ, for which the eccentricity of their orbit can be taken approximately as null ($e \approx 0$), the radial component of the orbital velocity, $u_{r,pl}$, is described by Equation 2.4.

$$u_{r,\,pl} = \frac{2\pi a}{P}\sin(2\pi\phi)\sin(i) \tag{2.4}$$

The RV shows a sinusoidal variation with orbital phase ϕ, and depends on the inclination of the orbit i, the period P and the semi-major axis a. Similarly, the stellar RV can be derived from its semi-amplitude $K_{\star}$, by directly fitting the RV observations of the star. Throughout this thesis we define the orbital phase with reference to the transit centre, such that it varies between -0.5 and 0.5, both coinciding with the opposite point of transit centre in the orbit.

2.2 Stellar master-out spectra

The base principle of transmission spectroscopy is that the difference between the light entering and after it has crossed the atmosphere holds the information of the planetary absorption. As such, we require an accurate representation of the light before being transmitted through the atmosphere. Ideally, this corresponds to the area of the stellar disk directly behind the atmospheric ring that surrounds the opaque planetary disk. This is, however, impossible to measure directly. As such, some approximations have to be done. Under the crude assumption that the stellar disk is homogeneous, the properties of the local radiation before being transmitted are equal throughout the entire stellar disk, and thus equivalent to what we would observe outside of a transit. We discuss the effects of stellar variability and the caveats of its negligence further ahead in Section 3.3.

The spectrum of the light used to compute the transmission is commonly defined as the mean out-of-transit spectrum, which we designate the master-out spectrum, $\tilde{\mathcal{M}}_{out}(\lambda)$. As mentioned, this removes the time dependency of the out-of-transit exposures, $\mathcal{F}_{out}(t,\lambda)$, by stacking them into a higher S/N mean stellar spectrum in the SRF. This reveals the importance of having an abundance of out-of-transit measurements close in time to the transit itself. Prior to stacking the selected out-of-transit exposures, we must certify they are in the SRF, such that their spectral features align. This is done by making use of the reference frame transformations described in the previous section alongside the derived stellar radial velocities. Since the reduced ESPRESSO spectra is placed in the SSB reference frame, the transformation to the SRF is given by Equation 2.5.

$$\lambda_{SRF,i} = \lambda_{SSB,i}\left(1 - \frac{v_{sys}}{c}\right)\left(1 - \frac{u_{r,\star,i}}{c}\right) \tag{2.5}$$

The following step is to combine all spectra into the master-out by averaging them over time. In the practical and numerical realm, this process has an intermediate step which is placing all the spectra under the same wavelength grid. Due to the fact the star's velocity varies with time, all exposures will suffer a distinct shift, which misaligns the wavelength grids. With different wavelength grids, a simple average cannot be performed as the same bin indices will now correspond to different sections of the spectrum. There are two approaches possible to align the axes, either by interpolating all the grids onto a reference grid that can be arbitrarily chosen or executing the grid shift in velocity space by moving the data points the corresponding number of bins without altering the original wavelength grid.

The first method relies on a cubic splines fit on each of the shifted exposures, applied to a reference wavelength grid, which can be arbitrarily chosen, for example, as the grid of one of the exposures. A disadvantage of this method is the complexity associated with the uncertainty propagation, which acts as a computational bottleneck, thus different approaches to estimating the new uncertainties exist (Silva et al., 2022). A possible path is to perform an interpolation on the squared values of the uncertainties. An alternative to interpolation is aligning the grids by adding up the velocities and counting the equivalent number of bins this corresponds to. This approach takes advantage of ESPRESSO's precise bin size of 0.500 $\mathrm{km\,s^{-1}}$, such that a shift of 10 $\mathrm{km\,s^{-1}}$ would be equivalent to moving the data points 20 bins to the side while maintaining the wavelength grid intact. An illustration of this is shown in Figure 2.3, where a shift $\Delta\lambda$ of two bins is represented.

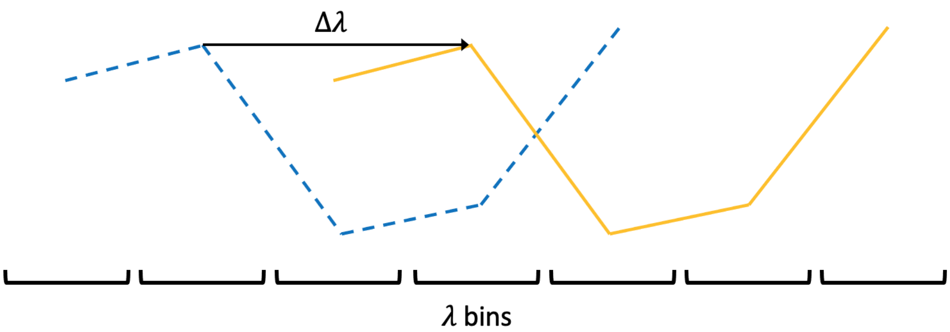

FIGURE 2.3: Illustration of shifting an initial spectrum array (dashed blue line) by two wavelength bins into the spectrum shown in orange, equivalent to $\sim$ 1 $\mathrm{km\,s^{-1}}$ for ESPRESSO.

This method avoids using interpolations altogether, however it does not fully align the spectra, since shifts below the instrument resolution would be rounded up to be assigned to the next available bin. Any shift in the interval $[0.75,\ 1.25]$ $\mathrm{km\,s^{-1}}$ would move the data points by 2 bins, meaning this method's precision is limited by ESPRESSO's bin size. Another approximation of the Doppler effect is implicit in this process, by applying Equation 2.6.

$$\lambda_{SRF,i} = \lambda_{SSB}\left(1 - \frac{v_{sys}}{c} - \frac{u_{r,\star,i}}{c}\right) \tag{2.6}$$

It is worth noting either method adopted will result in border effects due to the most shifted spectra having empty bins on the edges. This creates a decreasing S/N trend close to the edges of each order which should be trimmed to avoid the excessive noise. Thanks to ESPRESSO's high stability and spectral resolution, both methods are expected to perform well and maintain the trustworthiness of the data.

2.3 Transmission spectrum construction

The transmission spectrum of a planet is a differential spectrum, obtained by the ratio between each of the in-transit spectra and the master-out spectrum, $\tilde{\mathcal{M}}_{out}(\lambda)$, assumed to be the stellar spectrum behind the atmosphere. Each exposure contains the atmospheric signatures in the SRF. The signal can be refined by stacking the individual differential spectra between the first and fourth contact points, T_1 and T_4 respectively, and aligned in the PRF via Equation 2.7, into a mean transmission spectrum, $\tilde{\mathfrak{R}}(\lambda)$, with a higher S/N, as described in Equation 2.8.

$$\lambda_{PRF,i} = \lambda_{SRF,i}\left(1+\frac{u_{r,\star,i}}{c}\right)\left(1-\frac{u_{r,pl,i}}{c}\right) \tag{2.7}$$

$$\tilde{\mathfrak{R}}(\lambda) = \sum_{T_1<t<T_4} \left.\frac{\mathcal{F}(t,\lambda)}{\tilde{\mathcal{M}}_{out}(\lambda)}\right|_{PRF} - 1 \tag{2.8}$$

From the transmission spectrum, we arbitrarily deduct 1 to set the relative continuum flux level at 0 and such that an absorption would be associated with negative values. As was done to build the master-out spectrum, due to the varying planet radial velocity the wavelength grids must be once again aligned before stacking the exposures.

The derived transmission spectrum should now contain only the effects that arise from the planet atmosphere's interaction with the transmitted light. It is worth emphasizing the transmission spectrum is a differential spectrum and thus shows flux levels relative to the lightcurve. The transmission line depth δ_T, as defined here ($\delta_T \leq 0$), corresponds now to the ratio between the atmosphere's area and the area of the stellar disk not covered by the opaque planetary disk, as shown in Equation 2.9.

$$\delta_T = -\frac{(R_p+h)^2 - R_p^2}{R_\star^2 - R_p^2} \tag{2.9}$$

Here the base radius of the planet R_p is that obtained by the transit lightcurve as the size of the disk that is opaque to all wavelengths of light. This can eventually include the size of the lowest region of the atmosphere if it is opaque, leading to an underestimation of the atmosphere's size. With this in mind, we can translate the absorption depths observed in the transmission as a wavelength dependent planetary disk size. We may define the variable $R_{atm}(\lambda) = \frac{R_p+h(\lambda)}{R_p}$ which yields the apparent size of the planet+atmosphere in terms of the planet's radius, and with it manipulate Equation 2.9 to derive Equation 2.10.

$$\begin{aligned}
\delta_T &= -\frac{R_p^2\left(\frac{(R_p+h)^2}{R_p^2}-1\right)}{R_p^2\left(\frac{R_\star^2}{R_p^2}-1\right)} \\
\Leftrightarrow \delta_T\left(1-\frac{R_\star^2}{R_p^2}\right) &= R_{atm}^2 - 1 \\
\Leftrightarrow \sqrt{\delta_T\left(1-\frac{R_\star^2}{R_p^2}\right)+1} &= R_{atm} \\
\Leftrightarrow \frac{R_\star}{R_p}\sqrt{\delta_T\left(\frac{R_p^2}{R_\star^2}-1\right)+\frac{R_p^2}{R_\star^2}} &= R_{atm} \\
\Leftrightarrow R_{atm} &= \frac{R_\star}{R_p}\sqrt{-\delta_T+\frac{R_p^2}{R_\star^2}(\delta_T+1)} \qquad (2.10)
\end{aligned}$$

This relation, however, assumes the area covered by the atmosphere is fully opaque, and that the absorption depth is a direct consequence of the extension. This consideration is more relevant when analysing resonant lines since their large strength even in smaller abundances helps to lift the degeneracy between abundance and distribution on the absorption depth.

2.4 Line profiles and atmospheric dynamics

Once the transmission spectrum has been extracted, not only can it be used to detect atmospheric absorption from its various constituents but also to infer properties of the atmosphere and its dynamics. The conditions under which the absorption lines are formed will alter their overall appearance. To be able to extract information about the atmosphere, we must understand how its properties affect the absorption lines. The basic properties of an absorption line are its depth, width and position.

The depth of the line is related to how much radiation is being absorbed, which increases with abundance and volume covered. A higher abundance corresponds to having more absorbing particles, thus increasing the total absorption. For a light source much larger than the absorbing element, which is the case for exoplanet atmospheres, the volume covered by the gas will also contribute positively towards the depth, as was introduced in Section 2.3. Since both variables increase the absorption depth they become hard to disentangle due to their degeneracy. This issue can be dodged when dealing with strong lines, such as resonance lines. These are lines associated with the passage of an electron from the ground state to the first excited state and are the most intense lines. Strong lines are formed even with a small amount of particles, since their ability to absorb light with the respective wavelength is very large, which helps to lift the degeneracy between abundance and volume. We may then assume the depth is only a consequence of the area of the stellar disk covered by the element in the atmosphere and use equation 2.10 to roughly estimate its distribution. The sodium D doublet is a commonly used set of resonant lines in narrow-band transmission spectroscopy (Wyttenbach et al., 2015; Seidel et al., 2019, 2022; Tabernero et al., 2021).

Although electronic transitions have a certain energy associated to them, they can still be induced by photons with slightly different energies, giving rise to a broadened absorption feature. There are multiple factors that affect the width of the lines. Absorption lines have an inherent natural broadening which is a consequence of Heisenberg's uncertainty principle and the finite lifetime of excited states, Δt. The natural broadening corresponds to the narrowest width possible as the excited state's lifetime relates to the energy uncertainty as $\Delta E \Delta t \geq \hbar/2$. States with a shorter lifetime will show increased widths. Natural broadening forms a line with a Lorentzian profile. For reference, the hydrogen Hα line, which is associated with the electronic transition between energy levels $n = 2$ and $n = 3$, has a natural broadening of 0.46 $m\mathring{A}$.

In environments with high pressure, particle collisions become important as a source of broadening. Collisions cause perturbations to the energy state of electrons, such as relaxing them back to the ground state as such reducing the lifetime of the excited state. The net effect of each particle or molecule results in a broadened absorption feature. This form of broadening induces a Lorentzian shape, which is characterised by wider wings (de Pater and Lissauer, 2015). Equation 2.11 shows the profile φ_L in function of frequency ν, from an absorption line centred around ν_0.

$$\varphi_L(\nu) = \frac{\frac{\gamma_{col}}{4\pi^2}}{(\nu - \nu_0)^2 + \left(\frac{\gamma_{col}}{4\pi}\right)^2} \tag{2.11}$$

The γ_{col} coefficient is inversely proportional to the mean collision time, so we can verify that for higher pressures, hence shorter collision times, we will observe broader lines.

Spectral lines can also be broadened due to the Doppler effect, discussed in Section 2.1. The constituent particles of a gas at a temperature T move in random directions with a certain speed distribution, some inducing a blueshift and others a redshift. The net effect is a broadened absorption feature which depends on the velocity dispersion Δu_r, as stated in Equation 2.12.

$$\frac{\Delta\lambda}{\lambda} = \frac{\Delta u_r}{c} \tag{2.12}$$

Considering the particles behave according to a Maxwell-Boltzmann distribution, the higher the temperature the higher the velocity dispersion will be, which leads to a broadening of the observed absorption line. This is denoted as thermal broadening and is a form of Doppler broadening. A gas of particles with individual mass m at temperature T that follows a Maxwell-Boltzmann distribution generates a Gaussian profile, represented in Equation 2.13, with a standard deviation σ equal to the distribution's maximizing velocity $v_{max} = \sqrt{\frac{2kT}{m}}$.

$$\varphi_G(\nu) = e^{-\frac{1}{2}\left(\frac{\nu-\nu_0}{\sigma}\right)^2} \tag{2.13}$$

This profile differs from the Lorentzian profile for having narrower wings, since farther from the centre ν_0 it decays exponentially, while the Lorentzian decays with $(\nu - \nu_0)^{-2}$.

A thermally and pressure broadened line presents a combination between the previously discussed profiles. Such a scenario can be represented by the Voigt profile obtained via Equation 2.14, through the convolution between a Gaussian and a Lorentzian profile (de Pater and Lissauer, 2015).

$$\varphi_V(\nu) = \int_{-\infty}^{\infty} \varphi_G(\nu)\varphi_L(\nu - \nu')d\nu' \tag{2.14}$$

The central region is dominated by the Gaussian profile while farther from the peak the Lorentzian wings take over.

Thermal broadening is a microscopic application of Doppler broadening, however, it can also be applied at a macroscopic scale, such as by rotation. A rotating gas will appear blueshifted on one side and redshifted on the other, which globally results in a broadening proportional to the rotational velocity. It is important to note this relation has other dependencies, such as the orientation of the rotation, since no shifts, thus no broadening, would be noticed if the observer's LOS is aligned with the rotation axis. Rotation is one of many possible movement configurations, each with a different imprint on the absorption line shapes.

In the context of exoplanet atmospheres, we may expect to have a mix of the previously mentioned processes, whereas higher in the atmosphere the contribution is predominantly from the Doppler profile, where the pressure is lower and the thermal broadening dominates, and deeper down the lines assume the pressure-induced profiles as this becomes the dominant component. We also expect macroscopic scale movement to contribute to the line shape, allowing for the study of winds and the atmospheric dynamics (Borsa et al., 2019; Ehrenreich et al., 2020; Seidel et al., 2020a, 2021, 2023).

By observing the shape and properties of the planetary absorption lines we can extract a large amount of information about how it was formed and the environment in which it was formed. This can be taken a step forward by including the analysis of multiple elements' signals. Different lines are formed in different regions of the atmosphere and at distinct temperatures (Borsa et al., 2021; Hoeijmakers et al., 2019; Wyttenbach et al., 2020) and can thus be used to analyse complementary aspects of the atmosphere. An example is shown in Figure 2.4 with the equivalent heights in terms of WASP-121 b's radius obtained from multiple absorption features via transmission spectroscopy (Borsa et al., 2021).

Strong lines are more feasible to detect and resolve but weaker lines are more sensitive to noise and contamination, thus the process of reducing and correcting the data from its various contamination sources is a delicate and crucial step that must be rigorously followed.

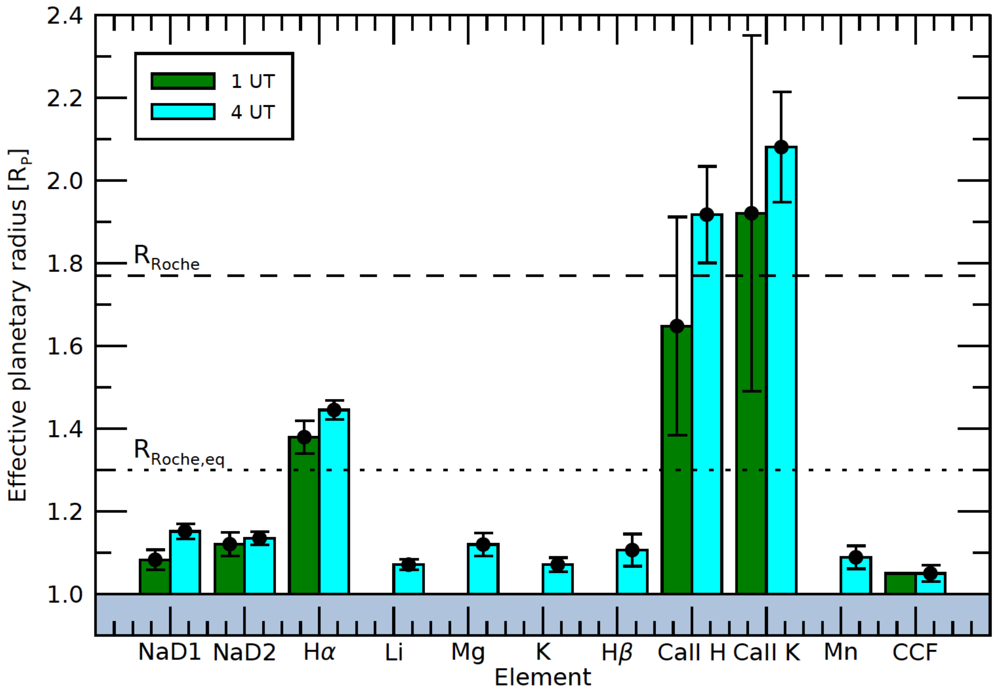

FIGURE 2.4: Figure 18 from Borsa et al. (2021) showing the equivalent planetary radius for several element absorption features in the atmosphere of WASP-121 b. The dashed line represents the equivalent Roche lobe radius of 1.77 R_p and the dotted line corresponds to the transit-equivalent Roche radius of $\sim 1.3\ R_p$.

Chapter 3

Data reduction and correction methods

The planetary signal in a transmission spectrum is faint, with excess absorption usually in the per cent order of magnitude or smaller. The construction of a planetary transmission spectrum is a delicate process where the corrections made have a tremendous effect on the outcome. A rigorous correction for sources of contamination is necessary, without over-correcting as this could affect an existing faint planetary signal. For ground-based observations, the Earth's atmosphere becomes a source of noise as its composing elements will interact with the incoming light, imprinting absorption and emission features on the spectra. An incomplete telluric correction has led to an overestimation of the sodium doublet absorption depth by 43% for WASP-127 b in Žák et al. (2019) compared to the results shown in Seidel et al. (2020b). The quality of the data has as well a very important role in the results. Low S/N data is capable of masking out signals from the planet's atmosphere, which likely was the principal cause for the non-detection of planetary sodium absorption features reported in Žák et al. (2019) for WASP-166 b (Seidel et al., 2020a). In the current Chapter, we explore the main data correction steps and sources of error essential to consider for transmission spectroscopy.

3.1 Telluric Correction

The vast majority of spectrographs used to analyse stellar and planetary spectra are ground-based. This implies the light from the target passes through Earth's atmosphere, interacting with its various composing atoms and molecules before reaching the instrument CCD.

Correcting for telluric absorption is a crucial step in analysing the target spectra as it can alter the line shapes of an eventual planetary signal due to insufficient or over-correction. In order to remove this contamination, a telluric spectrum is required. This spectrum can be obtained by pointing the telescope at a fast-rotating standard star and comparing the measured spectrum with a model of such star (Vidal-Madjar et al., 1986; Vacca et al., 2003; Ulmer-Moll et al., 2019). The telluric spectrum can then be extracted since the stellar lines would appear far broader than the narrow telluric lines, distinguishing them. However, the standard star calibration has several caveats: the standard star should be observed at a similar airmass as the target and close in time, in order to minimize telluric absorption deviations between the calibration frames and the science frames. This is especially significant for H_2O lines since these show hourly variability (Adelman et al., 2003; Wood, 2003). This method also implies the usage of observation time, which could have been used to observe scientific targets.

An alternative to this method is the fabrication of a synthetic telluric spectrum generated through models and taking into account local environmental conditions during the time of observations. This approach does not require telescope time and is capable of accurately replicating the contributions from our atmosphere on the data. For these reasons, the synthetic telluric spectra technique has claimed its ground in current instruments, such as those installed in the Paranal Observatory, which has been phasing out the standard telluric star method. A frequently used software to correct for tellurics is the ESO `molecfit` tool. A study conducted by Ulmer-Moll et al. (2019) with CRIRES data, measured in the J and K bands demonstrated the reliability of using synthetic spectra to model telluric H_2O and O_2 contamination. When compared to standard star observations, the synthetic methods, and particularly `molecfit`, performed better for the H_2O features and, although worse, still remarkably well for the O_2 lines.

3.1.1 `molecfit` Code

The `molecfit` code (Smette et al., 2015; Kausch et al., 2015) is a tool developed and used for telluric correction in the wavelength range $[0.3, 30]$ μm.

The code uses the atmospheric standard model, provided by the Reference Forward Model (RFM) (Remedios et al., 2001) which describes the pressure, temperature and molecular abundances in function of height for a given latitude. Global Data Assimilation System (GDAS) profiles, provided by the National Oceanic and Atmospheric Administration

(NOAA), are used to obtain information on the pressure, temperature, and relative humidity as a function of altitude, up until 26 km, for certain locations and are updated every three hours. A linear interpolation is used between the two measurements closest in time to the observations in order to estimate the conditions at this instant. A geographical interpolation is also made for the observatory using the four closest points and the accuracy of this step is assured by the $1^\circ \times 1^\circ$ geographical grid used. The specific observation conditions are provided within the header of the data files, which `molecfit` uses to model the telluric spectrum.

Once the target spectrum is imported a careful selection of isolated telluric lines must be done, avoiding any telluric lines that might be mixed with stellar features. The line regions fitted using `molecfit` for this work are shown in Figure 3.1, along with one of the exposures used to define these regions, containing the strongest isolated telluric lines in the Na I doublet order. The synthetic spectrum is produced by a Line-By-Line Radiative Transfer Model (LBLRTM) code described in (Clough et al., 2005) using the atmospheric model as an input. The line database used is an updated version of the HITRAN 2008 (Rothman et al., 2009) and HITRAN 2012 (Rothman et al., 2013) databases containing information on over 2.7 million lines of 42 molecular species. Some species' column density can be modelled by `molecfit`, such as H_2O, CO_2 or O_3, while others must be provided by the user, such as NH_3 or SO_2. The code then fits the designated fitting line regions using the C library MPFIT (Markwardt, 2009) through a least squares routine with the Levenberg-Marquardt technique. Having the telluric fit, the code constructs an ultra-high resolution telluric spectrum $\left(\frac{\lambda}{\Delta\lambda} = 4.000.000\right)$ which can then be used to remove the Earth's atmospheric features from the science data. The software was put in action for the first time for exoplanet studies in HARPS data (Allart et al., 2017) and has also been used on ESPRESSO data (Allart et al., 2020; Seidel et al., 2022, 2023). A more detailed description of `molecfit` can be found in Smette et al. (2015), Allart et al. (2017) and in the `molecfit` user manual *.

*https://www.eso.org/sci/software/pipelines/skytools/molecfit

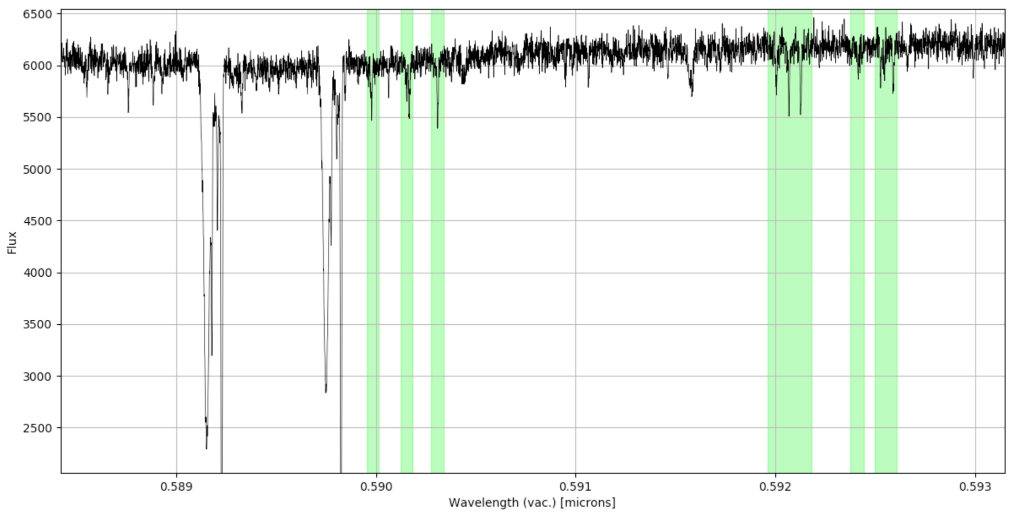

FIGURE 3.1: Image of the `molecfit` interface containing an observed spectrum from our data set (black line) and the regions which were be used to fit the telluric model (green shaded area).

3.2 Low S/N regions

An observation has several sources of uncertainty or error important to consider. The instrument itself has an error associated with the reading of the information, which is caused by the amplifier that translates the count of electrons, or charge, into a difference in voltage. This is called the read-out-noise (RON) and for ESPRESSO it is below 10 electrons per pixel. Another important source of uncertainty is photon noise, which is a physical source and not dependant on the instrument. Photon noise is a consequence of the source emitting photons at random meaning, even with a perfect instrument and no contamination whatsoever, we would measure fluctuations between exposures. The number of detected photons k in a fixed period of time from a source that emits, on average, N photons per said period follows a Poisson distribution, which has a standard deviation of $\sqrt{N}$. Therefore, the uncertainty induced by photon noise is taken as the square root of the number of photon detections in each pixel. A measurement is then said to be photon noise dominated if $\sqrt{N} \gg$ RON. For a given instrument with a set RON, the combination between the brightness of the source and the exposure time defines in which regime of noise dominance the data is. Unless very faint targets are being observed (magnitudes in the visible band below ~ 15 for ESPRESSO*), it is frequently the case that photon noise is the dominant source of uncertainty in astronomical observations.

*https://www.eso.org/sci/facilities/paranal/instruments/espresso/doc.html

The S/N, used to assess the quality of data corresponds to the ratio between the number of detections and the noise. In a photon noise dominated scenario the S/N can be approximated to $\mathcal{F}/\sqrt{\mathcal{F}}$, where $\mathcal{F}$ represents the measured flux for each pixel. Observations with a low S/N have low levels of flux or photon detections and the noise becomes comparable with the amplitude of the desired signal, consequently being able to mask out such signal. It is thus of great importance to have high S/N quality data to prevent high levels of noise from suffocating the information of interest. With this concern in mind, it is frequent to discard data sets with very high noise levels, or a low S/N.

Low signal can be a spectra-wide property of the data, in case it is of poor quality, however, it can also be localised to a part of the spectrum where low fluxes are observed, which is the case for very strong absorption lines. At the core of strong absorption features the flux level can be very low, leading to locally small S/N values. In the context of exoplanet atmospheres, these spectral regions can significantly affect the transmission spectrum (Barnes et al., 2016; Borsa and Zannoni, 2018). A possible solution is to simply mask these regions out, which on one hand removes part of the planetary signal from the total data set, though on the other it enhances the quality and reliability of the final result.

Common sources of locally low S/N are deep stellar absorption lines, as well as from interstellar medium (ISM) clouds in the line of sight between the target star and the observer.

3.3 Stellar variability

The assumption that the star is homogeneous throughout its surface is a rudimentary approximation since stars are known to have several effects providing the stellar disk with variations of different kinds and magnitudes. Stellar inhomogeneity implies the planet covers portions of the stellar disk with varying properties during its transit.

The most basic of these effects is the limb darkening, a geometric effect that causes the star to be brighter in the centre and dimmer towards the edges (Carroll and Ostlie, 2017). This effect is wavelength dependant and is caused by the fact photons observed near the limb are originated at a higher, and thus cooler, layer of the star, making this region appear dimmer. It is useful to define the angle θ between a position in the stellar disk and the centre, such that $\theta = 90^\circ$ at the edges and $\theta = 0^\circ$ at the centre, as well as the parametrisation $\mu = \cos(\theta)$. Considering the light intensity at the disk centre to be $I_0 = I(\mu = 1)$, limb darkening can be modelled using the quadratic polynomial approximation shown in Equation 3.1 (Espinoza and Jordán, 2015), where $I(\mu)/I_0$ is the ratio between the light intensity at a position μ from the centre and u_1, u_2 are the limb darkening coefficients (LDC).

$$\frac{I(\mu)}{I_0} = 1 - u_1(1-\mu) - u_2(1-\mu)^2 \tag{3.1}$$

This accounts for the impact of the limb darkening on the continuum, however, it has also been found that lines in the star's spectrum vary drastically between the limb and the disk centre, which is rarely taken into consideration (Pietrow and Pastor Yabar, 2023).

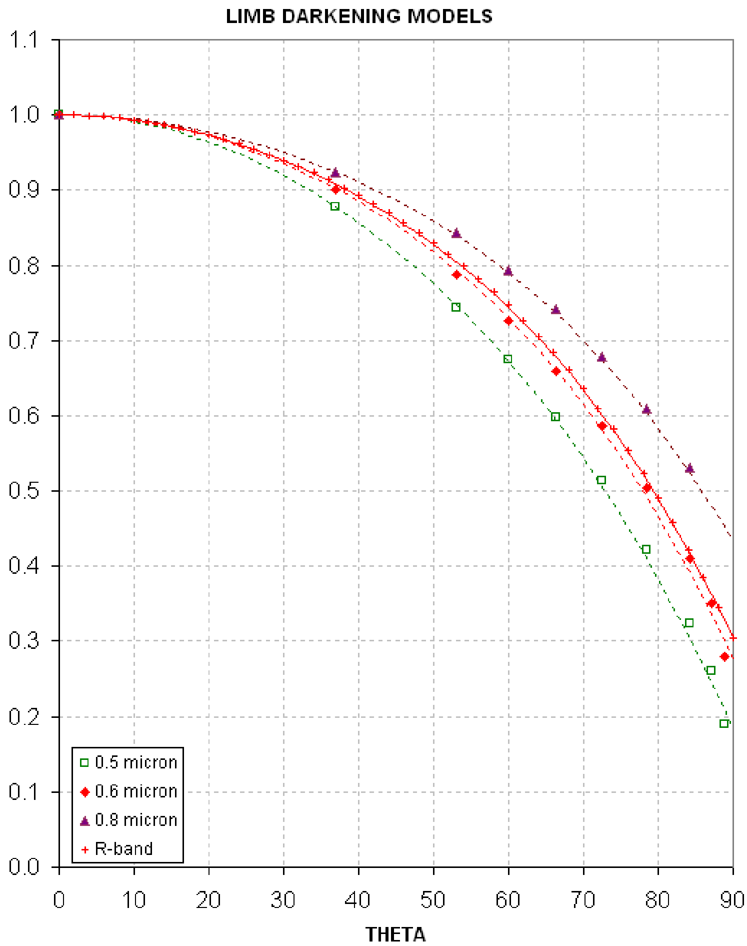

FIGURE 3.2: Figure taken from http://brucegary.net/XO1/PlanetSizeModel.htm showing the ratio $\frac{I(\mu)}{I_0}$ assuming quadratic limb darkening models for the Sun at 4 different wavelengths: 0.5 micron, 0.6 micron and 0.8 micron, represented by the green, red and purple dashed lines and markers. The solid red line illustrates the same effect integrating over the R band.

The star's rotation has a very important effect on its spectrum, locally and globally. As discussed in Section 2.4, rotation implies distinct parts of the rotating body show different radial velocities and thus different Doppler shifts. For a spherical shape, such as a star, the net effect is a centred yet broadened line. During a transit, the planet will block part of the stellar disk which will alter the stellar lines due to the asymmetry between redshifted and blueshifted contributions. As the planet crosses different portions, this will leave an imprint on the star's observed RV. This effect is called the Rossiter-McLaughlin (RM) effect (Holt, 1893; Rossiter, 1924; McLaughlin, 1924) and the pattern seen in the RV will depend on, among other variables, the orbital plane normal axis with respect to the stellar rotation axis, given by the obliquity angle λ, and the offset between the transit line and the parallel diameter of the stellar disk, represented by the impact parameter b (Winn et al., 2008; Triaud, 2018). The amplitude depends on the effective size of the planet (Snellen, 2004) and on the magnitude of the observed rotational velocity, which must take into account the stellar inclination, since a pole-on view would show no rotational broadening. Due to the degeneracy between the stellar rotation inclination and the rotation velocity, a joint parameter is commonly used and designated $v \sin(i_\star)$. Figure 3.3 shows three examples of distinct orbital configurations and their respective signal on the stellar RVs. In some cases, the planet only crosses one side of the star, which results in a pattern similar to the right-most example in Figure 3.3. We note that it is also possible to observe no effect in case the planet crosses along the rotation axis, with $\lambda = 90^\circ$ and $b = 0$. The comparison between the solid and dotted lines demonstrates how both the RM effect and limb darkening can act together to form the displayed signature.

The RM effect plays an important role in transmission spectroscopy, since it further breaks the assumption that the entire stellar surface is homogeneous and that the pre-transmitted light is equal to the mean stellar spectrum. The RM effect is known to interfere with transmission spectra observations, capable of producing false detection signals. Sodium was detected via the D doublet on the atmosphere of HD 209458 b in Charbonneau et al. (2002); Snellen et al. (2008); Albrecht et al. (2009), however Casasayas-Barris et al. (2020) found that the sodium doublet signals observed in high-resolution transmission spectra could be reproduced by a combination of the RM effect and limb darkening. Massive earlier type stars, such as A, B and O stars, have been noticed to present higher rotational velocities on average (McNally, 1965; Tassoul, 2000; Nielsen et al., 2013) and so the effect of their rotation on the spectra observations should be carefully evaluated.

The magnetic activity of stars also presents several challenges to exoplanet research by inducing inhomogeneities in the stellar surface in the form of several phenomena, such as

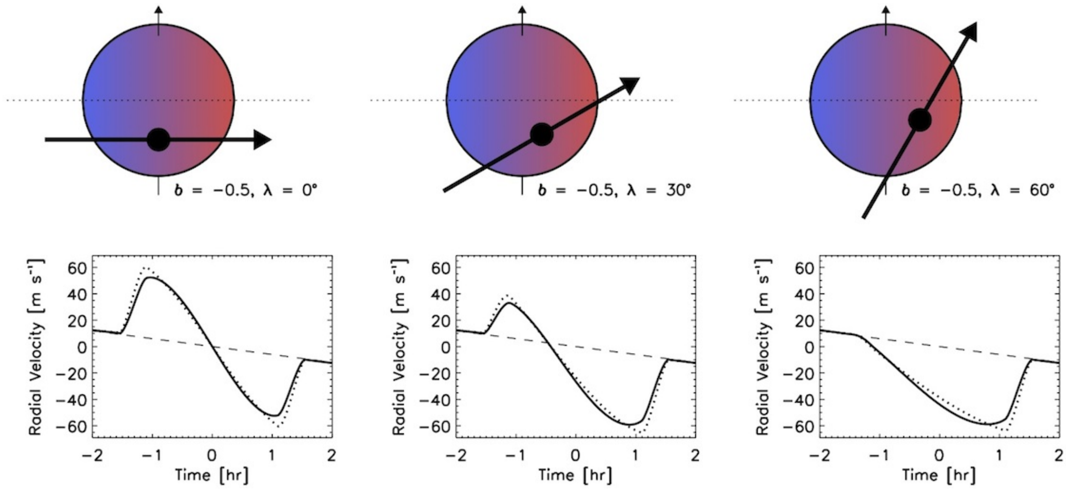

FIGURE 3.3: Figure taken from https://wasp-planets.net/tag/rossiter-mclaughlin-effect/ based on Fig. 2 in Gaudi et al. (2017), showcasing three distinct orbital configurations, with $\lambda = 0°$, $30°$ and $60°$ and $b = 0.5$, from left to right. The dashed line corresponds to the Keplerian velocity of the star while the solid and dotted lines to the observed stellar RV considering limb darkening and disregarding it, respectively.

spots and plages. For instance, star spots are darker and cooler than the non-active (quiet) stellar surface and thus when they are in the visible hemisphere the star may appear dimmer and redder, which affects exoplanet transit observations and leads to contaminated estimations of its radius, for example (Boldt et al., 2020; Oshagh et al., 2014). Photometry observations on the Kepler 51 system showed radii estimations for the Kepler 51 b and Kepler 51 d scattered by around 10 % of the previous literature value, likely due to spot crossings (Libby-Roberts et al., 2020). Active regions are known to affect spectral lines of the star, such as their CCF's RV, FWHM and line bisector span (Dumusque et al., 2014). On the hot Jupiter WASP-19 b, (Sedaghati et al., 2017) reported the detection of TiO and photochemical hazes in its atmosphere, however later studies by Espinoza et al. (2019) revealed a featureless atmosphere, associating this discrepancy to large active region crossing contamination. The study presented in Oshagh et al. (2014) showed the effect of active region crossings in the transmission spectrum, mainly in the blue portion of the spectrum where they found a signal that can be falsely interpreted as scattering from the planet's atmosphere (Oshagh et al., 2014). Due to the relatively short lifetime of active regions, large variations can be seen between separate observing nights' data, caused by the presence and crossing of magnetic activity phenomena (Priest, 2014). The discrepancy between the mean stellar spectrum containing the effect of unocculted active regions is greater when the planet crosses one of such regions, since in this case the master-out should ideally be the spectrum of the active region. To minimize the effect of magnetic activity on transmission spectroscopy observations one may remove exposures coinciding with spot crossings, if the amount of data allows for such. Alternatively, carefully accounting for the effects of magnetic activity via modelling tools also allows to circumvent activity contamination (Espinoza et al., 2019; Boldt et al., 2020). For transmission spectroscopy observations it is frequent to conduct simultaneous photometry measurements, among other purposes, to monitor any stellar variability, including spot crossings (Seidel et al., 2019, 2020b; Zhang et al., 2022; Steiner et al., 2023).

Stellar activity is a consequence of the star's magnetic field, which is predicted to be caused by the dynamo effect due to the movement of ionised gas within the convective region of the star (Priest, 2014). Small late-type stars, such as M or K, are either fully convective or have a large convective envelope, which allows for stronger magnetic activity close to the surface. Massive stars either have a thin convective envelope or none at all, which implies little to no activity (Kippenhahn, 2012). As such, stellar activity is more prominent on later-type stars, however, it is still possible to occur and detect on earlier-type stars (Balona, 2011; Rackham et al., 2019).

Another effect originated by stellar rotation, though less prominent, is gravity darkening. If stars rotate fast enough their shape becomes slightly oblate, extending around the equator and pinched at the poles due to the centrifugal force. The change in shape causes the local effective gravity to increase near the poles and to decrease near the equator. The local gravity relates to the effective temperature positively in a power law (von Zeipel, 1924; Lucy, 1967), meaning the poles will appear hotter and brighter while the equator appears cooler and dimmer. This also leaves a mark for planets that transit with a non-null obliquity. A study on the effect of gravity darkening on high-resolution transmission spectroscopy concluded the magnitude of this effect is comparable to the magnitude of the typical noise levels, and can thus be ignored for most cases (Cauley and Ahlers, 2022).

All these effects contribute to the contamination in transmission spectroscopy and should be cautiously accounted for.

Chapter 4

WASP-178 b transmission spectroscopy

In the previous Chapter, we described a general overview of the base principles of transmission spectroscopy and some of its common caveats. Each target and observation, however, brings particular challenges which require the methods to be tailored accordingly.

In the current Chapter, we describe the procedures taken in the particular case of our WASP-178 b observations with ESPRESSO. We apply the data correction steps addressed in Chapter 3 and follow the framework described in Chapter 2 to the ESPRESSO transit data sets, treating each night separately to obtain both transmission spectra.

4.1 ESPRESSO data description

To understand the information hidden in the data we must first understand how the data is measured, formatted and reduced, in this case, for the ESPRESSO spectrograph. In Section 1.1.2.1 the instrument was described from a more mechanical point of view, what follows is how the data is stored and processed.

Observations made with ESPRESSO come as two-dimensional images, referred to as S2D, with a cross-dispersion axis, which separates the various portions or orders of the spectrum, and a dispersion axis, which goes along the wavelength interval of each portion of the spectrum. ESPRESSO data has 85 orders with distinct wavelength intervals, taking into account that the total number of orders is doubled due to the pupil slicer mentioned in Section 1.1.2.1. In Figure 4.1 is one of the S2D spectra from our data set with the 170 orders in the vertical axis and the wavelength bins in the horizontal axis. On each order,

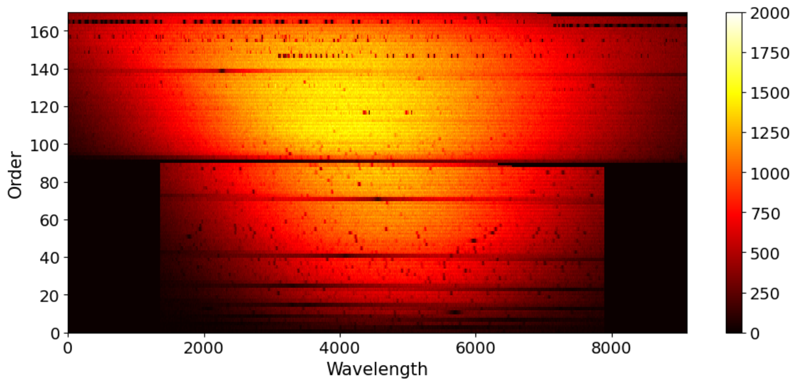

FIGURE 4.1: S2D spectrum measured from fibre A with ESPRESSO during the first transit. The vertical axis represents the several orders caused by the cross-dispersion while the horizontal axis corresponds to the wavelength bins in each order.

the intensity gradient between the centre and the edges is denoted as the blaze function, which is a characteristic of the instrument's optics. Additionally, several spectral features can be seen throughout the spectrum, including tellurics. During observations the optical fibre A is placed on the target of interest while fibre B can be placed either on the sky, to monitor any telluric emission lines, or with a wavelength calibration frame, to better determine the wavelength axis at the time of the observations. The observations used for this work were executed with fibre B observing the sky.

The very initial steps of calibration and data reduction are performed using the ESPRESSO Data Reduction Software (DRS*), including the extraction of the orders, wavelength calibration, blaze correction and sky subtraction with fibre B, in case it is set on sky.

4.2 Observations of WASP-178

The data studied throughout this thesis is composed of two transit observations of WASP-178 b taken with the ESPRESSO instrument in HR21 mode as part of the ESPRESSO GTO programme 1104.C-0350. The observations were conducted on 2021 May 03 and 2021 July 09, with the UT4 and UT2 telescopes of the VLT, respectively. WASP-178 is a bright type A1 IV-V star with a magnitude in the V band of 9.95 and at a distance of 418 ± 16 pc (Gaia Collaboration et al., 2018). WASP-178, with a stellar mass of 2.169 ± 0.089 $M_{\odot}$ and an effective temperature of 9350 ± 150 K, is the second hottest star known to host an exoplanet. Its only child, WASP-178 b, is an UHJ with an equilibrium temperature of 2470 ± 60 K and an orbital period of 3.3448371 ± 0.0000011 days (Hellier et al., 2019;

*https://www.eso.org/sci/software/pipelines/espresso/espresso-pipe-recipes.html

Pagano et al., 2023), making it an ideal target for atmospheric studies. The target system and previous research on it are further described in the following Section 4.3.

On the first night of observations, a total of 48 exposures were taken, of which 23 were during transit and the remaining 25 were out-of-transit. The second night resulted in 61 exposures, 35 in-transit and 25 out-of-transit. Both observations captured the full transit event, as well as out-of-transit spectra before and after. During the first night, the first 13 exposures were taken with an exposure time of 300 s while the remaining 35 had an exposure time of 500 s. This change was done in order to increase the S/N of these measurements, possibly due to unfavourable conditions during the observation, as indicated by the high level of seeing. On the second night, an exposure time of 300 s was used for all measurements. In Figure 4.2 are the observing conditions of each exposure taken during both nights, with information on the airmass, seeing, and the S/N. We can verify the first round of observations is generally more reliable as the S/N is more consistent and higher on average than on the second night, which shows lower values of the S/N, partly as a consequence of the reduced exposure time. We defined a lower threshold for the S/N of 15 to avoid low-quality data from affecting the results. The signal of the second night's observations is also compromised by the passage of clouds above the observatory. The S2D spectra were obtained through the DACE* platform and reduced using the ESPRESSO DRS (version 3.0.0). During the reduction of the data, the blaze function was corrected for both nights.

We focus our study on the ESPRESSO orders containing the Na I D doublet (116 and 117), Mg I b triplet (86 and 87), Hα (138 and 139) and Li I resonance doublet (142 and 143) lines. The ESPRESSO DRS corrects for the majority of cosmic rays, however, some are still present on the reduced data. For the orders relevant to this work we removed cosmic rays via a 6 σ clipping routine. The algorithm evaluates the flux difference between adjacent wavelength bins and rejects points with sharp and excessive variation (beyond 6 times the standard deviation of the consecutive bins' flux differences), which is characteristic of cosmic rays. These points were then replaced by the mean of the adjacent 6 points (3 on each side). Accounting for both nights and all exposures, this process affected a total of 24 points in orders 86 and 87, 75 points in orders 116 and 117, 65 points in orders 138 and 139 and 75 points in orders 142 and 143. This totals to less than 0.0002 % of the reduced data contained in these orders.

*https://dace.unige.ch/

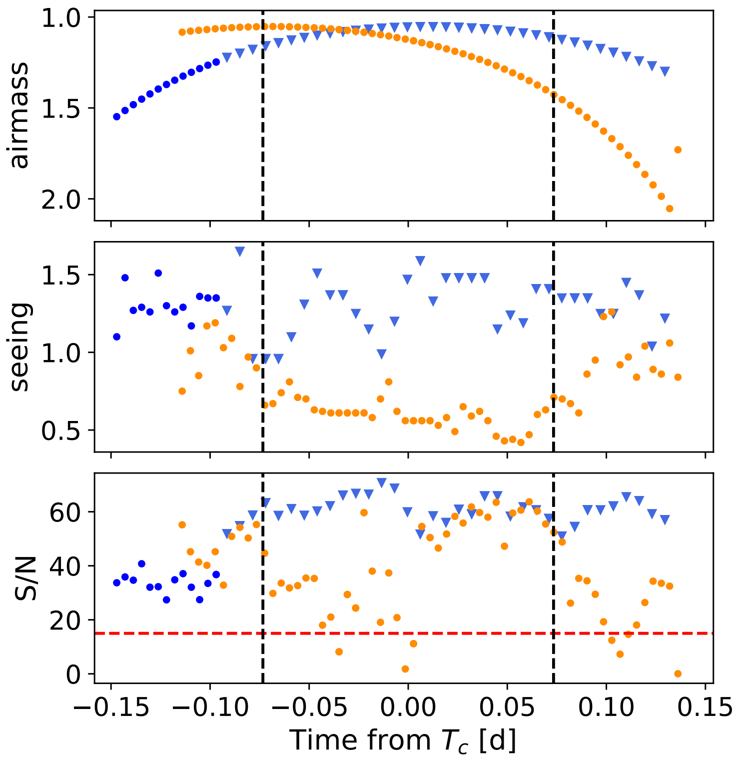

FIGURE 4.2: Observing conditions for each exposure taken on the first (blue) and second (orange) nights. The exposures marked as dots were taken with an exposure time of 300 s while the triangular markers are assigned to 500 s of exposure time. The dashed red line on the S/N plot (bottom) represents the threshold below which the data was discarded.

4.3 WASP-178 system parameters and properties

Upon correcting for outliers and filtering the S/N of the data (see Section 4.2), we gathered information on the target system, which is composed by stellar, planetary and orbital parameters. The parameters for the system's position and stellar magnitude have previously been obtained by the GAIA survey (Gaia Collaboration et al., 2018), with WASP-178 b's planetary and orbital parameters determined by Hellier et al. (2019) and Rodríguez Martínez et al. (2020) through the analysis of transit photometry and radial velocities. Recently the target was also observed with CHEOPS* and TESS† to study its reflective studies (Pagano et al., 2023), which yielded a more precise determination of a few stellar parameters.

*CHaracterising ExOPlanets Satellite
†Transiting Exoplanet Survey Satellite

On the dates of our ESPRESSO observations, simultaneous photometry measurements of WASP-178 b were made with the EulerCam imager mounted on the Swiss 1.2-metre Leonhard Euler Telescope (Lendl et al., 2012). Along with these two transits, two more were observed on the nights of 2021 June 29 and 2023 April 02. These datasets were used by our collaborator A. Psaridi* in coordination with this work to determine updated parameters with a higher degree of precision. The combined lightcurves were modelled and the system parameters determined with the `CONAN` code (Lendl et al., 2020), a Markov Chain Monte Carlo (MCMC) framework, while the quadratic LDC were estimated by the `LDCU`† code (Deline et al., 2022). Figure 4.3 shows all four lightcurves analysed along with the best-fit model. In Table 4.1 we present the parameters adopted throughout this work based on the previously mentioned literature. We derived the scale height of WASP-178 b using the reported equilibrium temperature T_{eq}, as in Equation 4.1, shown in Table 4.1, assuming a Jupiter-type atmosphere with mean molecular weight $\mu = 2.3\ \mathrm{m_H}$ (Sing et al., 2016; Wyttenbach et al., 2020), where $\mathrm{m_H}$ is the atomic mass of hydrogen, and the equilibrium temperature reported in Hellier et al. (2019).

$$H = \frac{k_B T_{eq}}{g\mu} \tag{4.1}$$

An important parameter to monitor is the $v \sin i_\star$, as it is related to multiple sources of stellar contamination, such as the RM effect and the gravity darkening. Stars of the same spectral class as WASP-178 typically present higher rotational velocities, around 10^2, which makes WASP-178's $v \sin i_\star$ relatively small in comparison. The study conducted by Rodríguez Martínez et al. (2020) led to the hypothesis that WASP-178 is in a near pole-on orientation, which would justify the reduced $v \sin i_\star$ reported in the literature. This was recently backed up by the results from Pagano et al. (2023), who estimated roughly a 15° angle between the stellar rotational axis and the LOS. We additionally notice the orbit to be misaligned, with an obliquity of $\lambda = 91.3°$. Combined with the impact parameter of $b = 0.539$ we arrive at the orbital architecture reported in literature illustrated in Figure 4.4, represented by the black dashed line. The Figure includes the effect of a quadratic limb darkening law given by the LDC in Table 4.1.

The orbital velocities can be derived by the two-body problem, simplified by the fact we assume a null eccentricity. The projected planetary orbital velocity is obtained as

*Observatoire de Genève, Département d'Astronomie, Université de Genève
†https://github.com/delinea/LDC

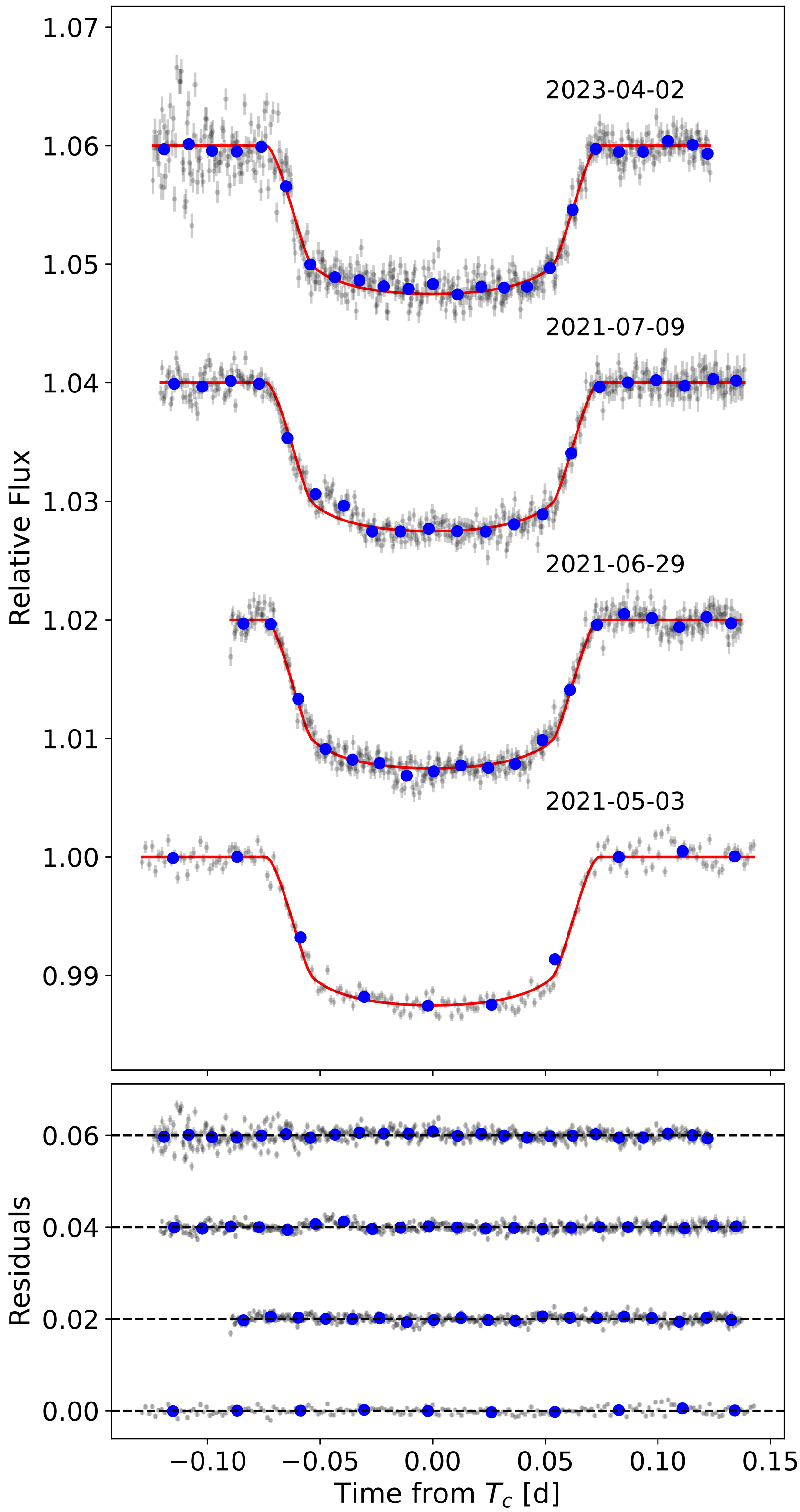

FIGURE 4.3: Lightcurves of four WASP-178 b transits measured with EulerCam, two of which were done simultaneously with this work's ESPRESSO data. An offset of 0.2 was consecutively added to each observation for better visibility. The best-fit model to the combined data is shown by the red lines. The residuals are presented in the lower panel in the same order as the respective lightcurve.
Reference: A. Psaridi

TABLE 4.1: Stellar and planetary parameters of the WASP-178 system from literature adopted in this study.

WASP-178 System parameters		
RA_{2000}	15:09:04.89	[5]
DEC_{2000}	-42:42:17.8	[5]
Parallax p [mas]	2.3119 ± 0.0600	[5]
Magnitude [V_{mag}]	9.95	[5]
Systemic velocity (v_{sys}) [$km\,s^{-1}$]	-23.908 ± 0.007	[2]
Stellar parameters		
Star radius ($R_\star$) [$R_\odot$]	1.772 ± 0.020	[4]
Star mass ($M_\star$) [$M_\odot$]	$2.169^{+0.083}_{-0.089}$	[4]
Proj. rot. velocity ($v \sin i_\star$) [$km\,s^{-1}$]	8.2 ± 0.6	[2]
Age [Gyr]	$0.05^{+0.06}_{-0.05}$	[4]
Effective Temperature (T_{eff}) [K]	9350 ± 150	[2]
Surface gravity ($\log g_\star$) [$\log g_\odot$]	4.35 ± 0.15	[2]
Metallicity ([Fe/H]) [$[Fe/H]_\odot$]	0.21 ± 0.16	[2]
Planetary parameters		
Planet radius (R_p) [R_{Jup}]	1.796 ± 0.022	[1]
Planet mass (M_p) [M_{Jup}]	1.66 ± 0.12	[2]
Eq. temperature (T_{eq}) [K]	2470 ± 60	[2]
Orbital and transit parameters		
Transit centre time (T_0) [HJD (UTC)]	$2459338.19728^{+0.00007}_{-0.00015}$	[1]
Period (P) [d]	$3.3448371^{+0.0000010}_{-0.0000011}$	[1]
Orbital semi-major axis (a) [au]	$0.0561^{+0.0005}_{-0.0013}$	[1]
Scaled semi-major axis ($a/R_\star$)	$7.00^{+0.03}_{-0.13}$	[1]
Orbital inclination (i) [°]	$85.50^{+0.09}_{-0.29}$	[1]
Proj. orbital obliquity (λ) [°]	$91.3^{+6.5}_{-6.3}$	[3]
Impact parameter (b)	$0.549^{+0.025}_{-0.008}$	[1]
Eclipse duration (T_{14}) [h]	$3.532^{+0.019}_{-0.004}$	[1]
Radius ratio ($R_p/R_\star$)	$0.10716^{+0.00047}_{-0.00039}$	[1]
RV semi-amplitude ($K_\star$) [$km\,s^{-1}$]	0.139 ± 0.009	[2]
Eccentricity (e)	0 (fixed)	-
Derived parameters		
Density (ρ) [$g\,cm^{-3}$]	0.632 ± 0.051	
Surface gravity ($\log g_p$) [cgs]	3.106 ± 0.033	
Planetary orbital velocity (v_{orb}) [$km\,s^{-1}$]	182.3 ± 2.6	
Approx. scale height (H) [km]	732 ± 59	
Transit depth of H ($\delta F/F$) [$\times 10^{-5}$]	13.1 ± 1.1	

References: [1] A. Psaridi, [2] Hellier et al. (2019), [3] Rodríguez Martínez et al. (2020), [4] Pagano et al. (2023), [5] Gaia Collaboration et al. (2018)

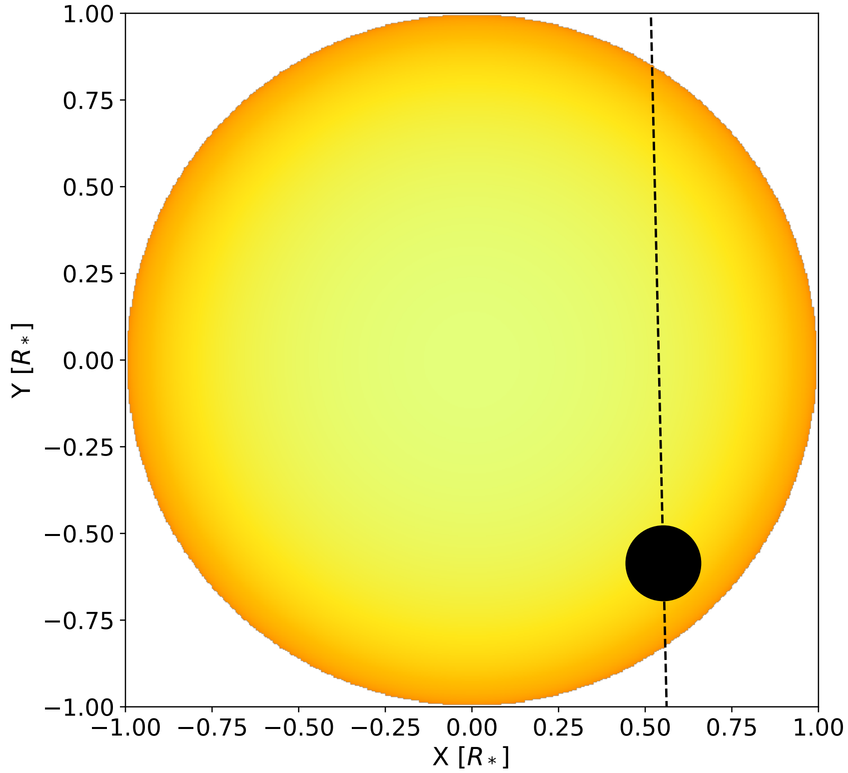

FIGURE 4.4: Illustration of the orbit architecture of WASP-178 b, marked by the dashed black line, from the observer's perspective assuming the star is seen equator-on. According to the literature, the orbit is misaligned with an obliquity of $\lambda = 91.3°$ and an impact parameter of $b = 0.539$. The colour or the stellar disk represents the effect of limb darkening, according to the LDC in Table 4.1.

stated in Section 2.1, while we use the semi-amplitude $K_\star$ from Hellier et al. (2019) to derive the projected stellar orbital velocity. The velocities for each spectrum are shown in function of the orbital phase in Figure 4.5, indicating as well the ingress and egress phases for reference. We note that during transit the planet's radial velocity varies by nearly 50 km s^{-1}.

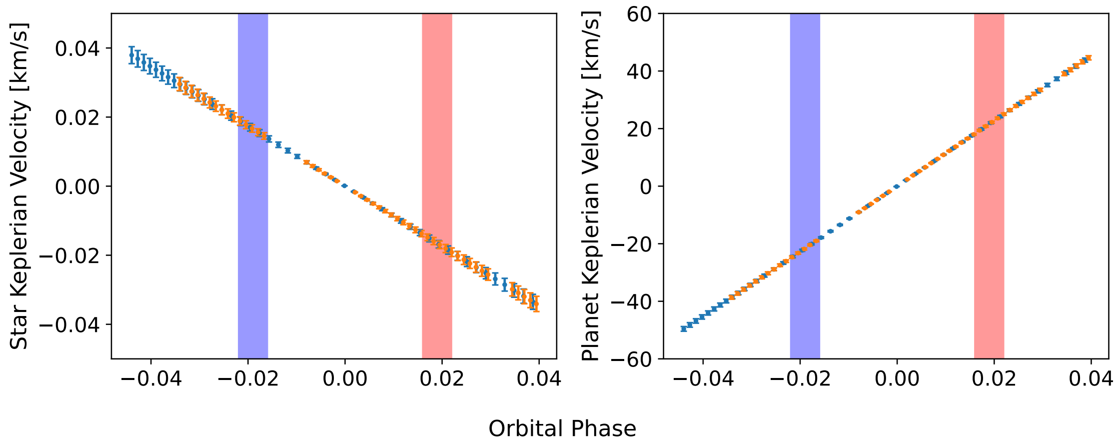

FIGURE 4.5: Keplerian radial velocities derived from the two-body circular orbit at the orbital phase of each observation point. The blue and red shaded regions mark the ingress and egress phases, respectively. Both transit observations are represented by the blue (first transit) and orange (second transit) markers and their uncertainties.

4.4 Data corrections applied

Before and during the construction of the transmission spectrum the data was carefully monitored in order to keep track of any consistent or sporadic sources of error. As mentioned above, the first necessary step is to correct telluric contamination by applying the concepts addressed in Chapter 3. Further on, more data correction steps are employed to remove contamination sources, such as low S/N regions, stellar variability and instrumental effects.

4.4.1 Telluric correction

To correct for telluric absorption in our data we relied on `molecfit`. The inclusion regions were fitted considering only H_2O as this is the most relevant species to correct for the visible spectral range we intended to study. The values in Table 4.2 were used as initial input parameters to run the telluric fit on both nights. The python package `Tayph`* was used as a wrapper for `molecfit` to run the correction for all exposures and orders automatically. The telluric corrected spectra were obtained by dividing the raw data by the respective fitted telluric model spectrum, for each exposure. In figure 4.7 we present the results of the telluric correction, displaying the mean spectrum before and after the procedure, along with the model fit by `molecfit`. From the visual analysis of Figure 4.7 we verify that the telluric contamination was corrected down to noise level.

*https://github.com/Hoeijmakers/tayph

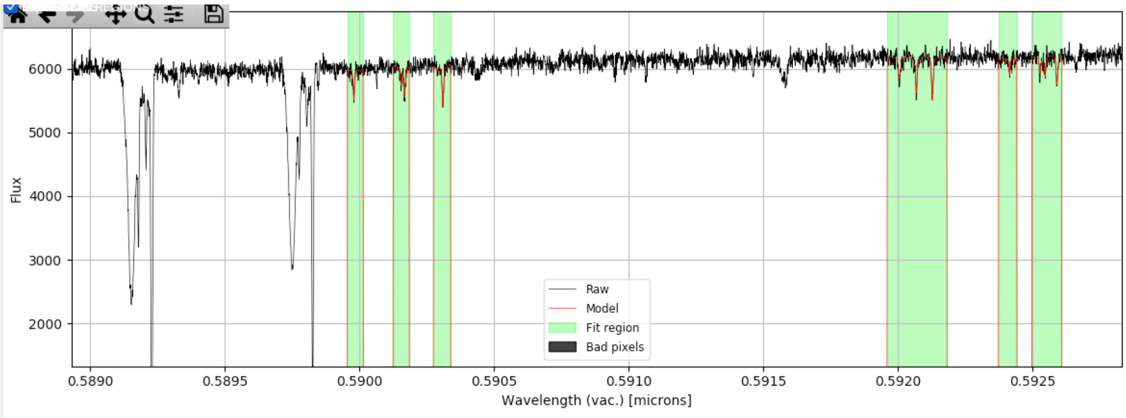

FIGURE 4.6: Image of the `molecfit` interface. The wavelength range near the sodium doublet is shown, with the wavelength axis given in vacuum and μm. The black line represents an observed spectrum. The green shaded areas mark the regions that were used to fit the telluric model. The result of the fit in these regions is shown by the red line.

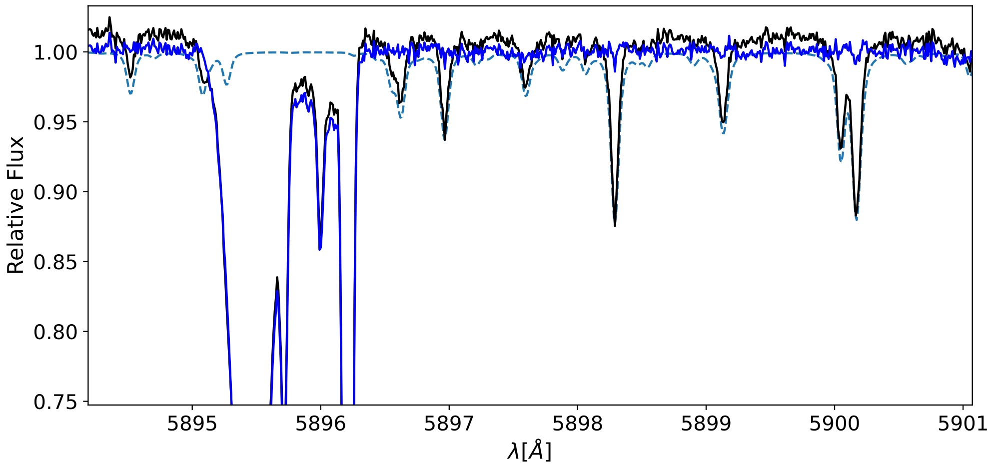

FIGURE 4.7: Mean spectrum before (black line) and after (solid blue line) the telluric correction, for the first night, averages over all exposures. The telluric model, also averaged over all exposures, is represented by the dashed blue line.

At this point, the spectra are in the SSB rest frame, have been corrected for telluric contamination and cosmic rays and remain unnormalised. Proceeding with unnormalised spectra to construct the transmission carries the advantage of natural S/N weights since the S/N directly relates to the flux level. As the transmission is a differential spectrum we expect it to assume a flat shape. By skipping the normalisation during the initial stages we avoid the added uncertainty of the process, simply performing the stacking of transmission spectra making use of the intrinsic S/N weight and dodging the risk of a faulty continuum fit interfering with the results. The use of unnormalised spectra is to be assumed unless stated otherwise.

TABLE 4.2: Initial input parameters for `molecfit` used for both nights.

Parameters	Values	Description
FTOL	10^{-9}	χ^2 Convergence criterion
XTOL	10^{-9}	Parameter convergence criterion
LIST_MOLEC	H_2O, O_2	Molecules included in the model
WAVELENGTH_FRAME	air	Wavelength reference frame
CONTINUUM_N	1	Degree of polynomial for the continuum
CONTINUUM_CONST	2000	Constant of polynom for the continuum
WLC_N	3	Chebyschev degree for wavelength calibration
WLC_CONST	0	Constant Chebyschev for wavelength calibration
RES_GAUSS	3.5	Gaussian FWHM in pixel
KERNFAC	15	Kernel size in FWHM units
PIX_SCALE_VALUE	0.16	Pixel scale in arcsec
SLIT_WIDTH_VALUE	1.0	Slit width of data in arcsec
REFERENCE_ATMOSPHERIC	equ	Equatorial MIPAS profile
LAYERS	0	Natural atmospheric profile
PWV	-1	No value taking into account

4.4.2 ISM absorption and low S/N masking

At a first visual evaluation of all spectra, we notice two sets of four lines in the sodium doublet orders. We display in Figure 4.8 these two sets of lines separately for both nights. The out-of-transit spectra were averaged between orders 116 and 117. Evaluating the shift each line has from the closest sodium doublet line, we observe between both transits the shifts are the same which rules out telluric origin because if it were the case they would be shifted differently according to the BERV on each night. The features for each set of lines also show consistent shifts from the sodium D lines, which indicates they are all in fact Na I D doublet lines from separate absorption sources at different radial velocities. We can identify the stellar sodium lines as being shifted by the systemic velocity, which for WASP-178 is -23.907 km s^{-1}, represented by the dashed black line in 4.8. We suspect the remaining three doublets to be caused by separate ISM clouds.

We fit a Gaussian profile to each of the lines through a least squares algorithm, done using the function `curve_fit` from the `Scipy` python package. To do so, we obtained each night's mean out-of-transit spectrum and normalised it with a second-degree polynomial fit in the intervals $[5880, 5886]$ and $[5898, 5910]$ $\AA$. The mean radial velocities for both nights are estimated to be -10.418 ± 0.018, 3.987 ± 0.075 and 14.7195 ± 0.0043 km s^{-1}. For the stellar line, we estimated a shift of -23.431 ± 0.019 km s^{-1}, which is deviated by ~ 0.5 km s^{-1} from the systemic velocity reported in Hellier et al. (2019). This corresponds

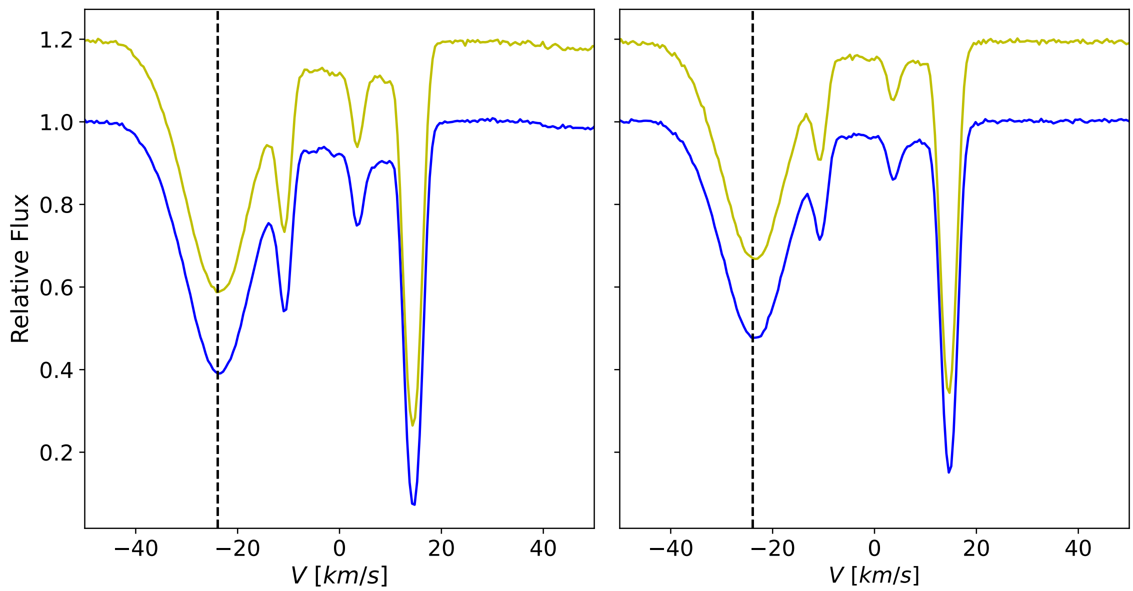

FIGURE 4.8: Mean out-of-transit spectrum for the first (blue) and second (yellow) nights in the rest frame of the SSB. The spectra are shown in terms of the shift velocity with respect to the expected Na I D2 (left panel) and D1 (right panel) lines' wavelength. The vertical dashed black lines are placed at the systemic velocity, $V = -23.908\,\mathrm{km\,s^{-1}}$, marking the expected position of the stellar Na I D doublet lines.

to the wavelength bin size of ESPRESSO, thus we take this result as consistent with the bibliography, and onward we use the literature value. We observe the variation of the ISM features between exposures is minimal, so we treat them as stellar lines, including them in the master-out correction.

The right-most ISM line shows the strongest absorption, eliminating 95.3% and 87.5% of the flux level on the first and second transits, respectively. In the core of these strong features, we verify a lack of photon counts, which results in a huge S/N drop near the line core. In this low S/N region, instrumental readout noise becomes relevant and comparable to the photon white noise. We avoid contamination from the low flux level by masking a 0.22 $\mathring{A}$ interval around the line centre. The masked values were replaced by the continuum mean of the adjacent 1 $\mathring{A}$ arm towards the red since the arm towards the blue is affected by more ISM lines. According to the derived planet velocities, we do not expect any atmospheric absorption signal to be lost due to the masked region by a margin of nearly 9 $\mathrm{km\,s^{-1}}$. The final in-transit sodium line would only be lost in the mask if the line is broadened by around 18 $\mathrm{km\,s^{-1}}$ or more.

4.4.3 Active region crossing

In order to verify the presence of stellar inhomogeneities we inspected WASP-178's observed RV at each exposure, as measured by the ESPRESSO DRS and stated in the headers of the data. Figure 4.9 shows the star's RV for both nights and the expected Keplerian radial velocity added to the literature systemic velocity, distinguishing the in-transit and out-of-transit measurements. We verify from the residuals, however, that the out-of-transit values have a constant offset from 0. Fitting these RV values with a least-squares algorithm we arrive at a systemic velocity of $v_{sys} = -24.0590 \pm 0.0021$ km s^{-1}, which differs from the literature value by 0.1510 km s^{-1}. This is an indication that the systemic velocity at the time of our observations might have increased slightly in magnitude since the time of the observations used in Hellier et al. (2019). This discrepancy can also be due to the different instrument RV offsets. Nonetheless, this separation is negligible given it is well below the bin size of ESPRESSO and thus will have no noticeable effect on the results.

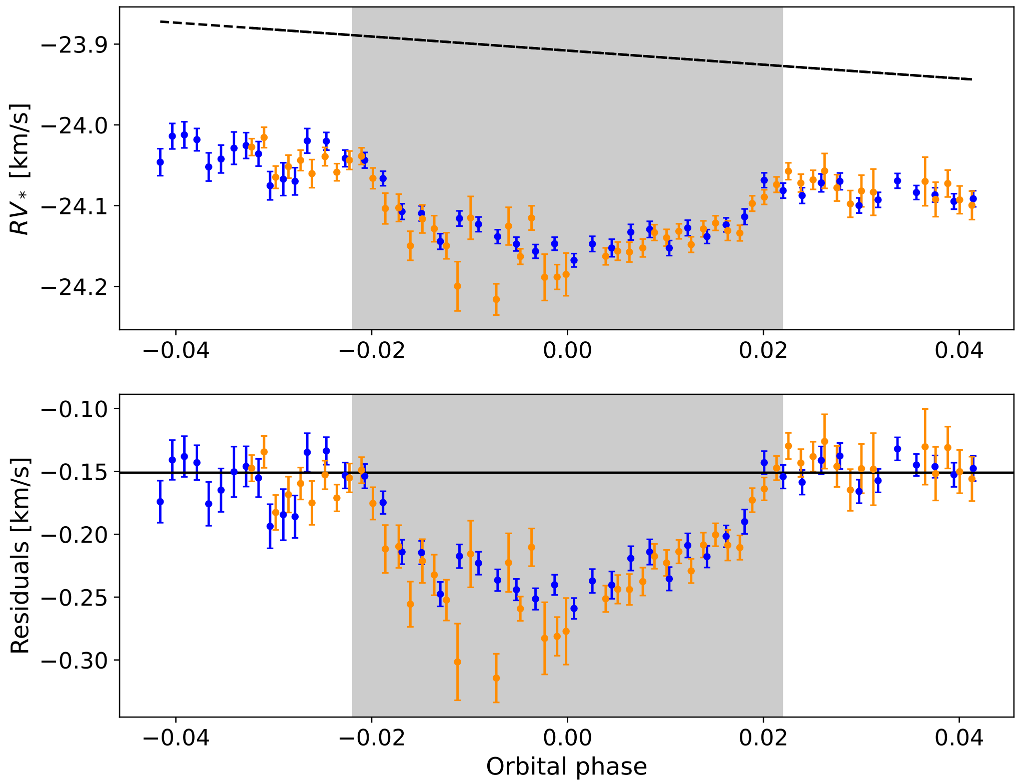

FIGURE 4.9: Radial velocities of WASP-178 for the first (blue points) and second (orange points) transits. The expected Keplerian velocity considering the literature systemic velocity value is represented by the dashed black line. The lower window contains the residuals as well as the fitted offset of the out-of-transit points, shown by the solid black line. The duration of the transit is marked as the darker-shaded region.

Additionally, we can observe two particularities in the RV values, the first is the bump present throughout the transit, which is caused by the RM effect, which will be discussed in the next section, and the second is the localised larger dispersion on the second night within the phase interval $0.015 < \phi < 0.007$. These measurements have a lower S/N, which leads to large error bars and dispersion, similar to what we verify after the transit. It can also be caused by the presence of stellar activity phenomena, such as with the crossing of the planet in front of a star spot. As discussed in section 3.3, activity for stars like WASP-178 is unlikely due to the lack of a convective envelope, however, it is still possible. The lightcurves analysed by A. Psaridi show a slight flux bump during the same interval of the second transit. The nearly coinciding time stamps of these aspects build further the argument in favour of stellar contamination, possibly due to an active region crossing, although it is not enough to validate the presence of an active region on the stellar surface.

To safeguard the results from the influence of a possible star spot the exposures within $0.015 < \phi < 0.007$ were discarded. As a consequence, a total of 6 in-transit spectra were discarded. It is important to note this may still leave a slight influence of the active region on the transmission since it can contribute to the master-out spectrum, which is assumed to be equal to the spectrum behind the planet.

4.4.4 Rossiter-McLaughlin and limb darkening correction

The presence of the RM effect was verified for our dataset through the RV provided in the ESPRESSO reduced data headers, plotted in Figure 4.9. During the transit, the bump observed in the RV is a clear mark of the effect of the planet crossing the redshifted side of the stellar disk, as demonstrated in Figure 4.11. The Figure illustrates the local shifts induced by the star's rotation and the particular path of WASP-178 b during transit. By definition, the obliquity is defined as the angle between the orbit plane and the star's rotation axis, and so it is frequent to display the transit as done in Figure 4.11. We can verify WASP-178 b only crosses the redshifted area of the star, making it appear overall more blueshifted during the transit, which is equivalent to observing lower RV values, which is precisely what is verified from Figure 4.9. This dataset's RV signals were used by our collaborators E. Esparza-Borges[*†] and M. Stangret[‡] to study the RM effect, in context of the ESPRESSO cooperation. They used RM models from the `ARoME`[§] library (Boué et al.,

[*] Instituto de Astrofísica de Canarias
[†] Departamento de Astrofísica, Universidad de La Laguna
[‡] INAF – Osservatorio Astronomico di Padova, Vicolo dell'Osservatorio 5, 35122, Padova, Italy
[§] http://www.astro.up.pt/resources/arome/

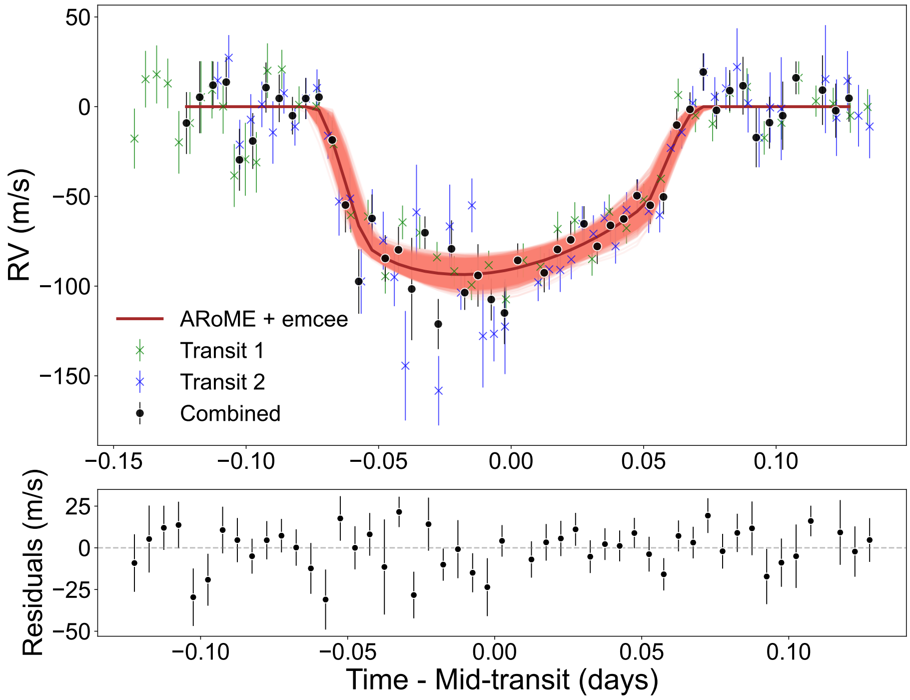

FIGURE 4.10: Rossiter-McLaughlin signal in the first transit (green crosses), second transit (blue crosses) and combined (black dots) RV time series. Additionally, the best RM model from the ARoME fitting and models within 1 σ are shown in magenta and light pink, respectively.
Reference: E. Esparza-Borges & M. Stangret

2013), implemented in Python via `PyARoME`*, and fitted these with the `emcee` MCMC code (Foreman-Mackey et al., 2013), achieving the profiles shown in Figure 4.10. By modelling the star's two RV time series combined they were able to obtain updated values for the transit centre, rotational velocity and obliquity angles, shown in Table 4.3. The transit centre presented is the variation relative to the value reported in Hellier et al. (2019), which is in agreement with the value obtained via the lightcurves analysis of A. Psaridi.

TABLE 4.3: Updated parameters from the fit to WASP-178's RV.

Transit centre shift (ΔT_0) [d]	$0.0013^{+0.0012}_{-0.0013}$	[1]
Proj. rot. velocity ($v \sin i_\star$) [km s^{-1}]	$10.48^{+0.63}_{-0.56}$	[1]
Proj. orbital obliquity (λ) [°]	$105.7^{+3.6}_{-4.2}$	[1]

References: [1] E. Esparza-Borges & M. Stangret

To assess how the RM effect and limb darkening impact the transmission spectrum we resorted to the `StarRotator`† code. `StarRotator` generates a simulated $N \times N$ grid,

*https://github.com/andres-jordan/PyARoME
†https://github.com/Hoeijmakers/StarRotator

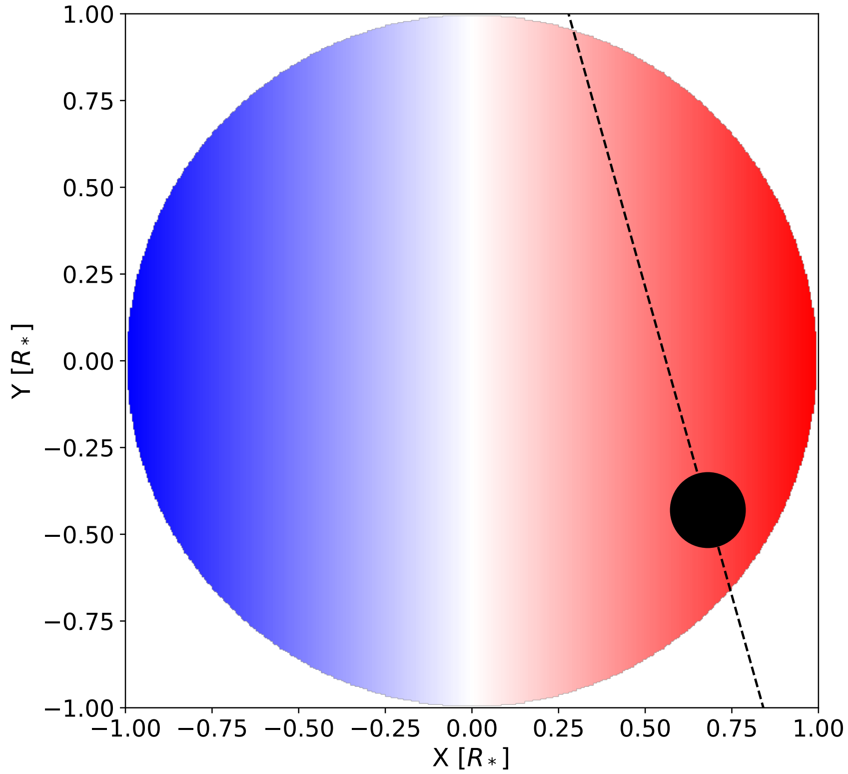

FIGURE 4.11: Illustration of the orbital architecture, similar to that in Figure 4.4, assuming an equator-on view of the star and the updated parameters in Table 4.3. The colour gradient represents the local $v \sin i_\star$ along the stellar surface, with the red shade corresponding to values of $v \sin i_\star > 0$ and the blue shade to the values of $v \sin i_\star < 0$.

where N is the diameter of the simulated stellar disk in pixels. A model spectrum is then adopted based on the values of the effective temperature T_{eff}, the surface gravity $\log(g)$ and the metallicity [Fe/H]. For each pixel, the stellar spectrum is locally estimated taking into account a quadratic limb darkening law as well as the local shift due to rotation. The code then simulates the transit and, for a defined sequence of orbital phases, estimates the observed integrated stellar spectrum, i.e. not blocked by the planet, and the residuals, which correspond to the fraction between the spectrum behind the planet and the mean out-of-transit spectrum. By dividing the unstacked transmission spectra by the returned residuals we are essentially attempting to obtain the stellar spectrum behind the planet and as such approach the true definition of the transmission spectrum.

For this work, we simulated the star on a 400×400 grid, with stellar spectral models from the PHOENIX database (Husser et al., 2013). We adopted the parameters as listed in Tables 4.1 and 4.3, except for the T_{eff}, $\log(g)$ and [Fe/H], since these had to be rounded to the nearest available model spectrum, which had $T_{eff} = 9400$ (K), $\log g_* = 4.5$ ($\log g_\odot$) and [Fe/H] $= 0.0$ ([Fe/H]$_\odot$). The model calculated relative absorptions in the SRF are shown in Figure 4.12 for each exposure. The signature left on the sets of lines studied is shown on the different panels, the pattern is identical for all, varying only the intensity and width. Since the parameters used were the same for both nights (except for the phase list) and the effect shown is model-obtained, these will be identical between both transits and as such we only show them for the first transit in Figure 4.12. The amplitude and width of the signal depend on the depth and width of the associated stellar lines, where sharp and deep stellar lines generate a deep and sharper residual. We can verify this from the panels in Figure 4.12. The Na I doublet and Mg I triplet are deep and narrow yielding the signal with the largest amplitude, while Hα presents a smaller effect amplitude but broader and there is practically no signal for Li I owing to the lack of this line in the star's spectrum. Taking the model results and stacking them in the PRF, we reach the relative absorption patterns in Figure 4.13. It is worth noting that the difference between both nights is the fact the phase list of the first is continuous and evenly spaced, while due to the removal of some exposures, the second's phase list is uneven, which gives rise to the sharp and repeating peaks. The first transit curve represents more accurately the line profile induced by the RM effect. These results imply the transmission spectrum would be contaminated by the RM effect, inducing variation of up to 0.03 %, capable of leading to a false detection or altering the shape of an existing planetary feature.

4.4.5 ESPRESSO interference patterns

The optical elements of ESPRESSO are made to provide extremely stable and precise measurements, however, an interference pattern has been noticed of instrumental origin (Allart et al., 2020; Sedaghati et al., 2021; Tabernero et al., 2021). This interference is generated in the Coudé Train optics and its amplitude depends on the UT used for the observations and on the direction in which we are pointing the telescope. The pattern is composed of two pseudo-sinusoidals, one with a higher frequency (~ 1 $\AA$ period) and the other with a lower frequency (~ 30 $\AA$ period). This interference is different for each observation, wavelength dependent and can be seen on each spectra when corrected for the stellar spectrum. When stacked in the PRF it can build up, leaving a significant pattern in the transmission which, in literature, is regularly treated as a "wiggle".

In our observations, the wiggles are not present in the orders containing the Mg I triplet, Hα nor the Li I lines, however, the lower frequency wiggles are present in the Na I doublet orders (116 and 117). In Figure 4.14 are shown each spectrum binned after

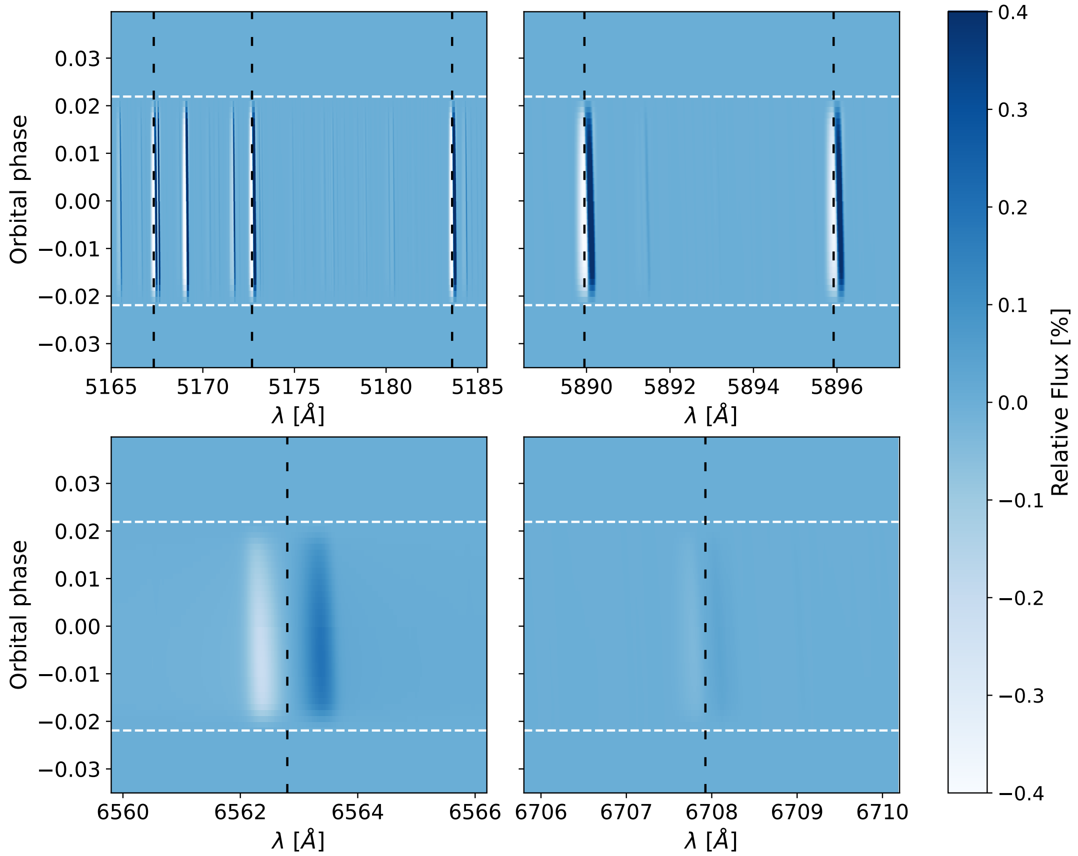

FIGURE 4.12: Model estimated relative absorption obtained via `StarRotator` and PHEONIX spectra due to the RM effect for the first transit in the SRF. Each panel shows a different set of lines. Top-left: the Mg I b triplet, Top-right: the Na I D doublet, Bottom-left: the Hα line and Bottom-right: the Li I resonant line. The white dashed lines mark the beginning and end of transit and the black dashed lines are the expected positions of the respective lines in the SRF.

dividing the master-out, with grid lines to aid their visualisation. The high-frequency wiggles are not visible in our data and can be ignored, on the other hand, the lower frequency patterns appear with a large amplitude, significantly impacting the continuum of the transmission spectrum and must be accounted for. During the first transit, the wiggles are larger in amplitude and focused towards the end of the Na I order. On the second observed transit, the interference creates a downward bump around the doublet. These patterns were corrected on orders 116 and 117 using a cubic splines fit to the data binned by x500. The process of dividing the spectra with a cubic splines fit adds error to the measurements so it is more effective to correct the wiggles in each night's stacked transmission spectrum in the PRF than to correct each individual exposure and afterwards stacking these, which accumulates the error associated to each correction. The wavelength intervals [5888, 5892] and [5894, 5898] were masked to prevent possible planetary

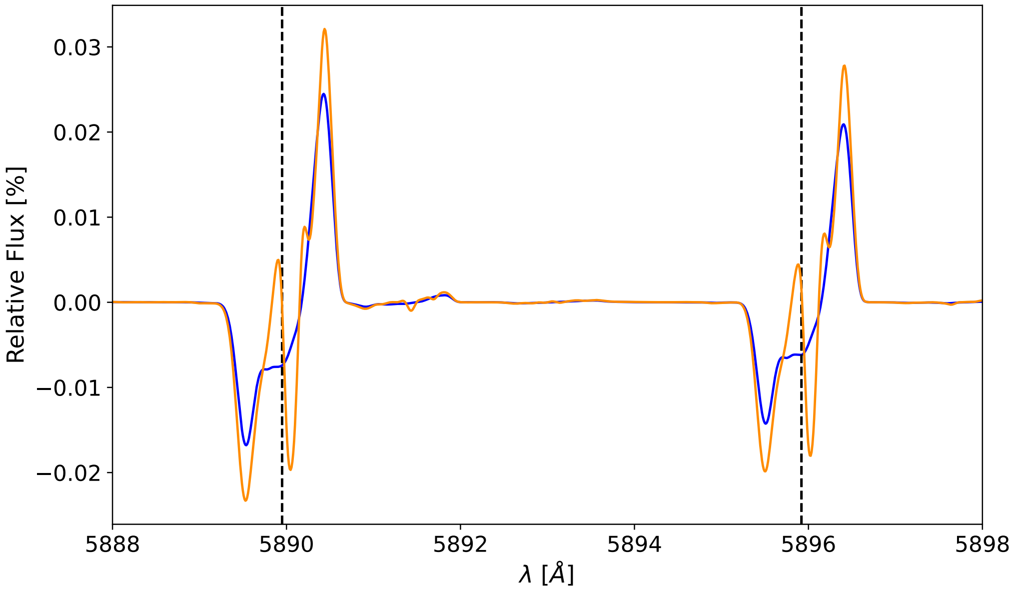

FIGURE 4.13: Model estimated relative absorption stacked in the PRF for the first (blue) and second (orange) transits around the Na I D doublet. The second transit's curve shows abrupt variations due to the removal of certain exposures.

sodium features from affecting the fit.

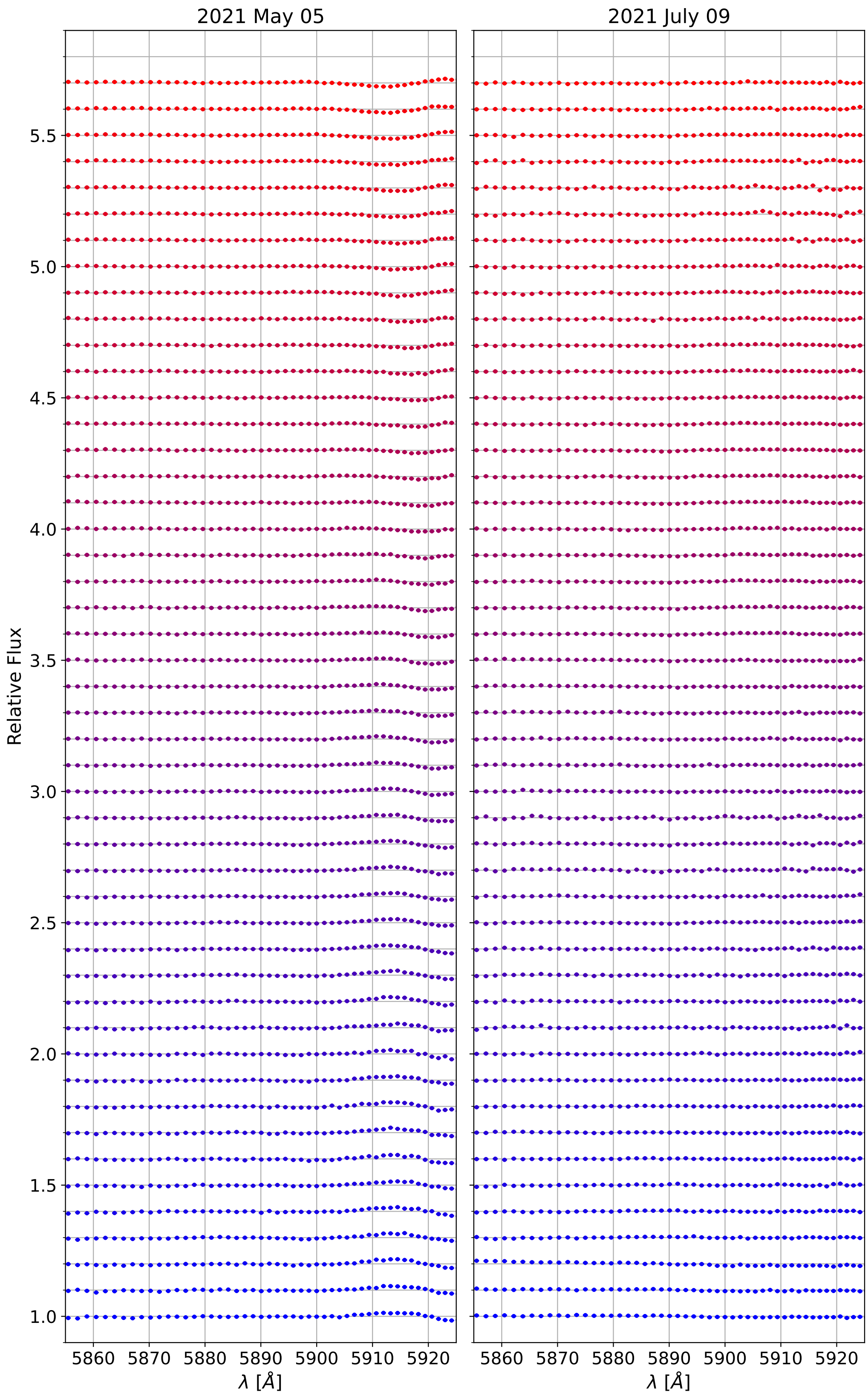

FIGURE 4.14: Master-out divided spectra from the first (left panel) and second (right panel) observed transits in the Na I D doublet orders and binned by x150. Each spectrum has an added offset of 0.1 and a horizontal grid line to aid its visualisation.

4.5 Stacked planetary absorption features

Upon dividing all exposures by their respective night's master-out, we obtained the transmission spectra in different moments of the transit. The data in this phase can be very useful to study the time-resolved transmission of the target atmosphere (Prinoth et al., 2023). By doing so, the study of how the atmosphere behaves with time becomes possible. This information is however limited by the S/N and overall quality of each exposure. In our case, the observations did not allow for a time-resolved study of WASP-178 b's atmosphere. Figures 4.15 and 4.16 contain all transmission spectra in the SRF around the lines studied in this work, along with each line's expected planetary trace based on the derived Keplerian velocity and the induced wavelength shift. These spectra were corrected for the several effects discussed in the previous sections, except for the instrumental wiggles. A planetary trace is not evident from these results since our observations do not possess high enough S/N to reveal the absorption on each exposure. It is clear these must be stacked in the PRF to achieve the necessary line strength for detection.

The spectra were shifted onto the PRF, interpolated onto a common wavelength grid, arbitrarily selected as the first exposure's grid, and then stacked to form each night's global transmission spectrum, shown in Figures 4.17 and 4.18. From visual verification, the Na I and Hα lines can be recognised, particularly for the first transit's data which is expected considering it has the highest S/N. The Li I order for both transits shows the absence of any planetary absorption signature, indicating the lack of lithium in the atmosphere of WASP-178 b. The most troublesome result is that of the Mg I b triplet orders, which show faint signals on the first night, however, the Mg I b2 and b3 lines seem to not be present for the second night, as well as the Mg I b1 line being considerably blueshifted. Nonetheless, the signals achieved are yet not strong enough for a detection claim on each spectrum, so these were combined into a single high S/N transmission spectrum. At this point, the temporal information contained in the data has been fully lost, at the trade-off for a higher S/N spectrum. The combined transmission spectrum was normalised at this stage with a linear fit to bring the continuum to 0 and avoid any trends. We verified the slope values to be at the noise level (at absolute most). These results around the lines of interest are presented in Figure 4.19.

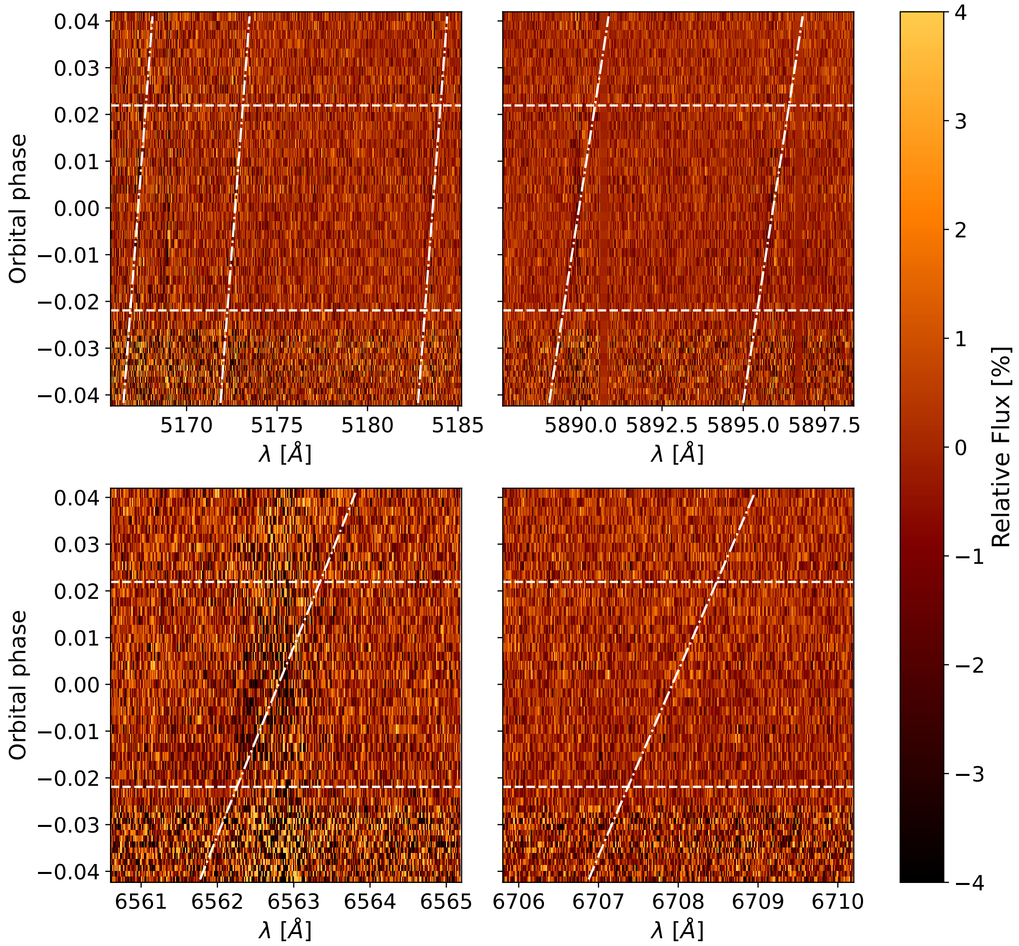

FIGURE 4.15: Transmission spectra in the SRF of the first observed transit with wavelength, phase and relative absorption represented by the colour. Each panel shows a different set of lines. Top-left: the Mg I b triplet, Top-right: the Na I D doublet, Bottom-left: the Hα line and Bottom-right: the Li I resonant line. The transit duration is marked by the horizontal dashed white lines while the dot-dashed white line shows the expected planetary line position based on the derived Keplerian velocity shift.

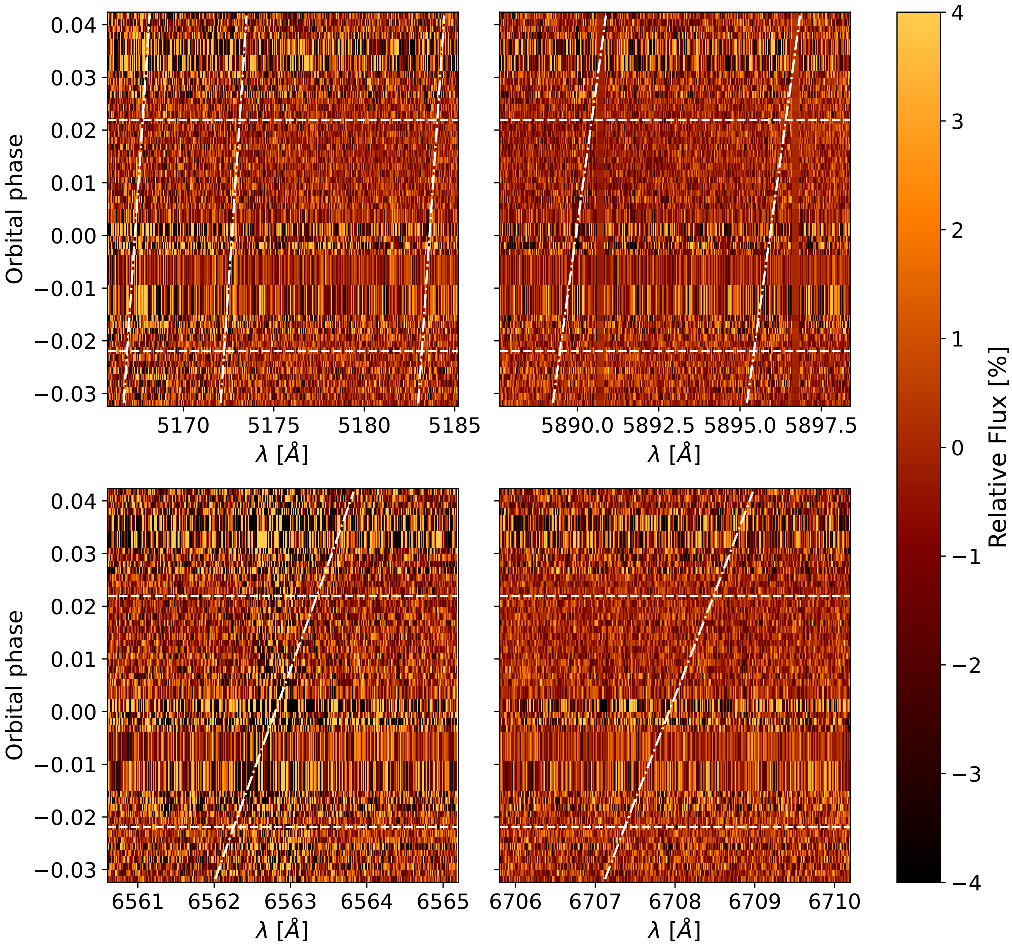

FIGURE 4.16: The same as Figure 4.15 for the second transit observations.

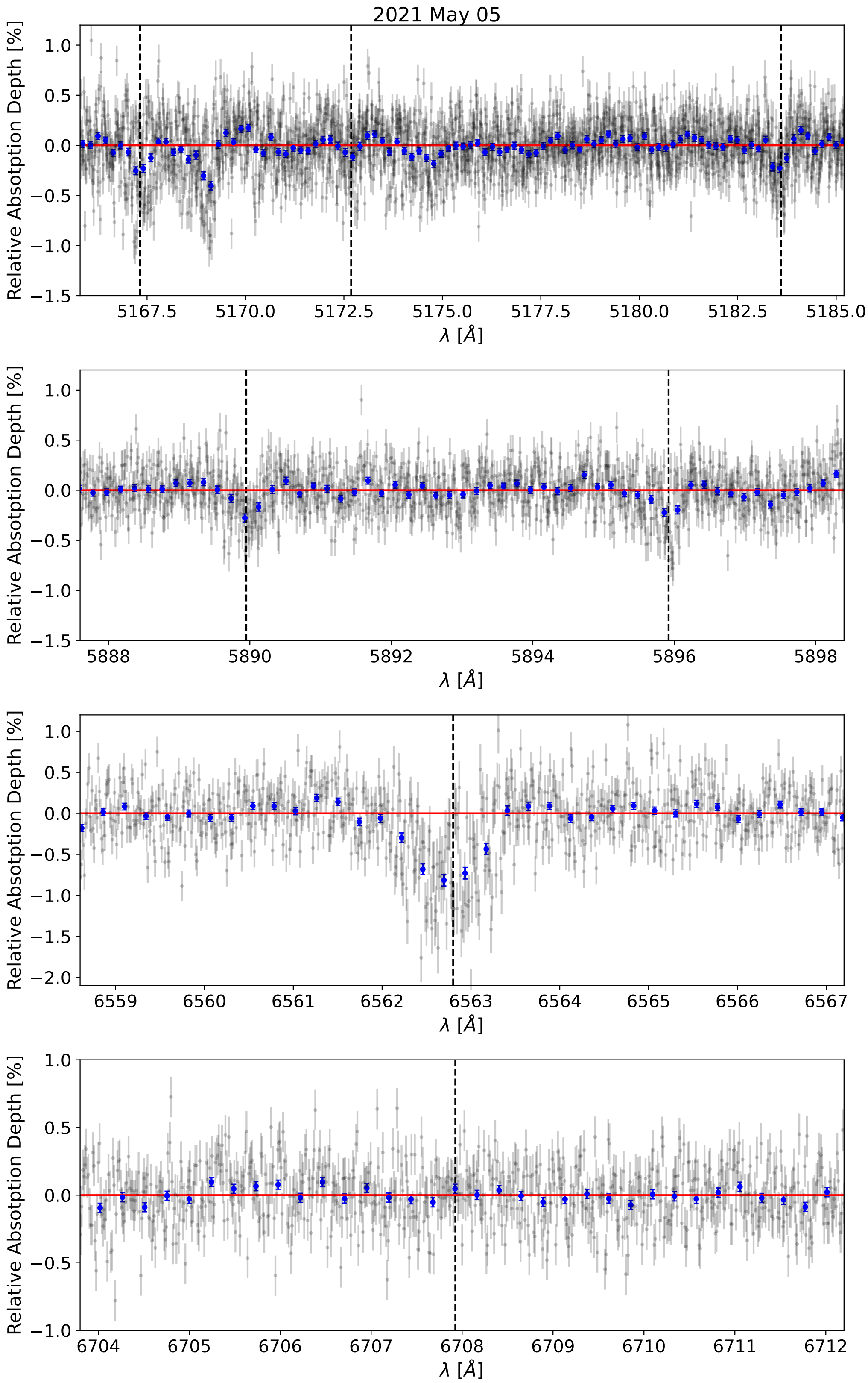

FIGURE 4.17: Stacked transmission spectrum of the first observed transit in the PRF near the Mg I b triplet, Na I D doublet, Hα and Li I resonant lines, respectively from top to bottom. A black dashed line is added on each feature's expected rest frame position.

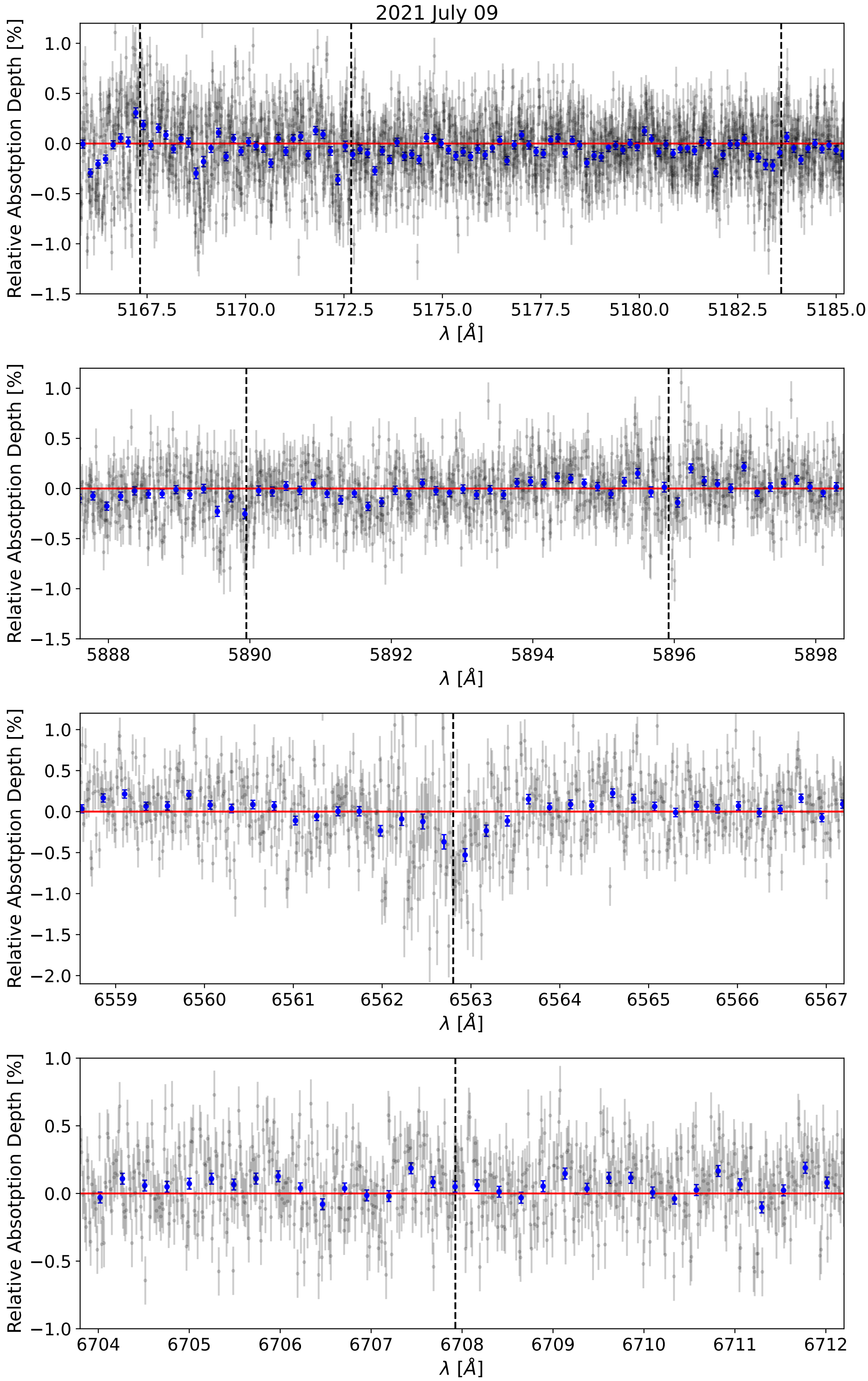

FIGURE 4.18: The same as Figure 4.17 for the second transit observations.

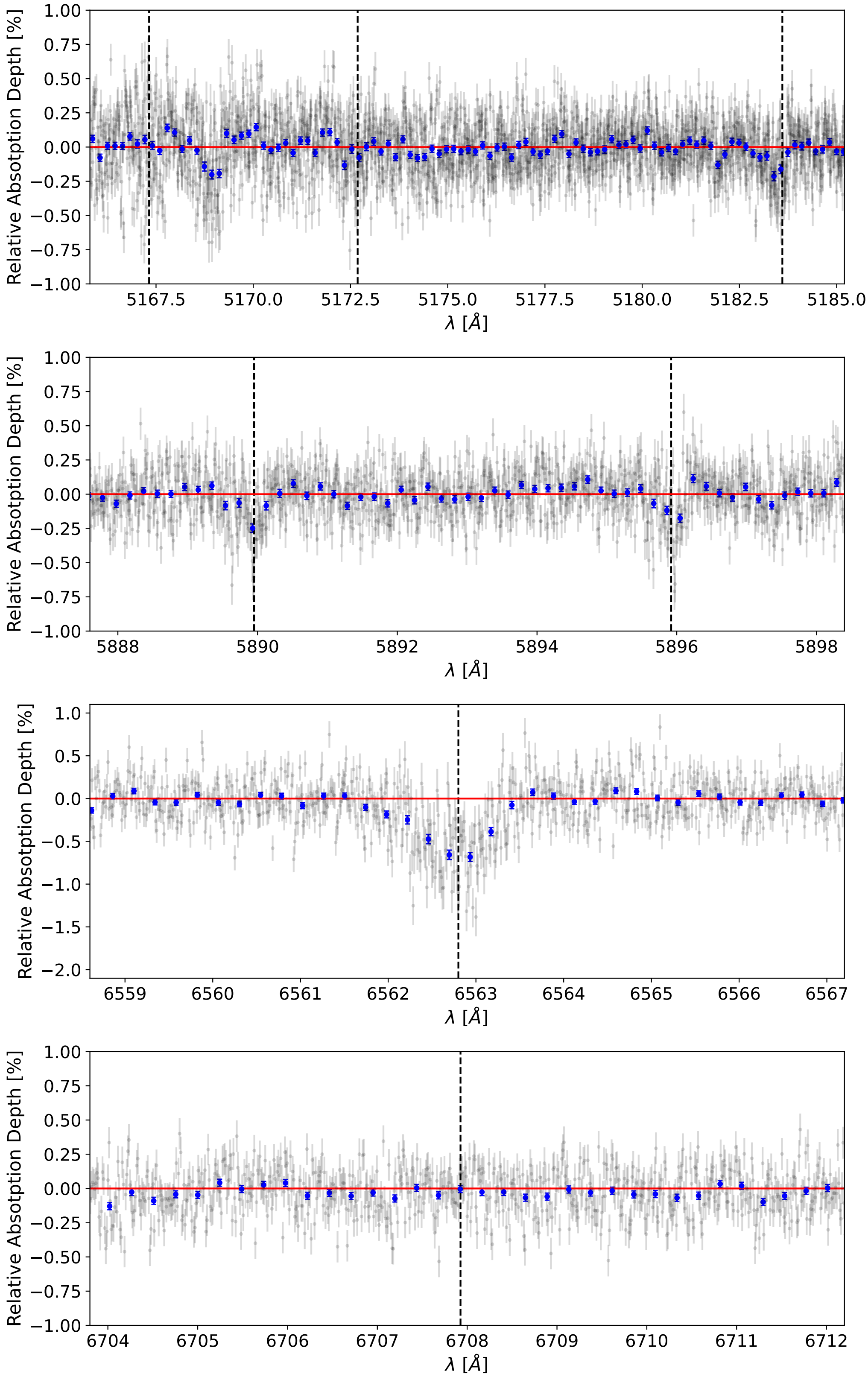

FIGURE 4.19: Combined transmission spectrum of WASP-178 b in the PRF near the Mg I b triplet, Na I D doublet, Hα and Li I resonant lines, respectively from top to bottom. Each feature's rest frame expected position is marked by the dashed black line. The red line corresponds to the continuum level after the linear normalisation.

Chapter 5

Analysis of the planetary absorptions

In the previous Chapter, we constructed the combined transmission spectrum for the two ESPRESSO observed transits. In the current Chapter, we use those results to detect the atmospheric absorption features of WASP-178 b and understand how these may be affected by the conditions and dynamics within while describing the analysis steps undergone. We begin with the detection of the atmosphere's components.

From this point onwards, we will focus on the detections of the Mg I b triple, Na I D doublet, Hα and Li I resonance lines. In order to detect these features, we relied on a Bayesian analysis with recourse to an MCMC routine implemented using the `emcee` Python package. Prior to the MCMC process, an initial least squares optimisation step is executed as a means to initiate the MCMC walkers close to the probability distribution's maximum. To improve the exploration of the parameter space, we added to the output of the optimisation method a random deviation for each walker up to 0.01% of the respective parameter's value. Subsequently, we ran the MCMC routine with 50 walkers, building chains with 10.000 iterations after a burn-in phase of 2.000 iterations. For each line, we attempt to fit a Gaussian profile, determined by the amplitude, FWHM and centre position. With this, we are implying the dominant broadening mechanism is the Doppler or thermal broadening, shaping the absorption line profiles into predominantly a Gaussian form. We used uniform priors for all parameters with the limits shown in Table 5.1. We note that the amplitude was allowed to decrease in magnitude until 0, corresponding to a non-detection, and the FWHM down to the thermal broadening of each element at a temperature of 2000 K, as this should be the smallest expected FWHM from a gas at such temperature. The temperature value chosen for the FWHM lower limit is slightly lower than the previously estimated temperatures of WASP-178 b and, although we do not expect to find a solution below it, the current choice allows for a more complete search of the parameter space.

TABLE 5.1: Uniform prior intervals used for the MCMC Gaussian line fits.

	Amplitude [%]	FWHM [Å]	Line centre [Å]
Mg I b3	[-1.0, 0]	[0.048, 2.0]	[5166.3, 5168.3]
Mg I b2	[-1.0, 0]	[0.048, 2.0]	[5171.6, 5173.6]
Mg I b1	[-1.0, 0]	[0.048, 2.0]	[5182.6, 5184.6]
Na I D2	[-0.75, 0]	[0.056, 2.0]	[5889.0, 5891.0]
Na I D1	[-0.75, 0]	[0.056, 2.0]	[5895.0, 5897.0]
Hα	[-1.5, 0]	[0.30, 2.0]	[6561.8, 6563.8]
Li I resonance line	[-0.75, 0]	[0.12, 2.0]	[6706.9, 6708.9]

The median values for each parameter's probability distribution as well as their 68% confidence interval can be found in Table 5.2. The best-fit model is plotted over the data points in Figures 5.1 to 5.4. The amplitude found is below 0 by a margin larger than 4 σ for the Mg I b1, Na I D2 and D1, Hα and Li I resonance lines. The Mg I b3 and b2 lines are only 1.0 σ and 2.3 σ below 0, therefore these cannot be detected for our dataset. The detection of only one of the Mg I b triplet lines is unlikely, given the complete absence of the b2 and b3 lines and that they should all have similar intensities. This leaves open the possibility that the b1 line might have been caused by a build-up of stellar and/or instrumental contamination. In any case, we continue analysing the lines with an amplitude below 0 by at least 4 σ. The FWHM and line centre can be translated in terms of velocity broadening and shift, granting the results shown in Table 5.3.

TABLE 5.2: Median values and respective 68% confidence intervals from the probability distributions of the Gaussian line fits.

	Amplitude [%]	FWHM [Å]	Line centre [Å]
Mg I b3	$-0.079^{+0.075}_{-0.144}$	$0.085^{+0.856}_{-0.033}$	$5166.63^{+1.06}_{-0.28}$
Mg I b2	$-0.130^{+0.056}_{-0.087}$	$0.183^{+0.272}_{-0.094}$	$5172.362^{+0.197}_{-0.037}$
Mg I b1	$-0.201^{+0.032}_{-0.034}$	$0.476^{+0.97}_{-0.77}$	$5183.426^{+0.035}_{-0.039}$
Na I D2	$-0.324^{+0.061}_{-0.060}$	$0.239^{+0.107}_{-0.054}$	$5889.951^{+0.015}_{-0.022}$
Na I D1	$-0.333^{+0.057}_{-0.077}$	$0.137^{+0.040}_{-0.043}$	$5895.969^{+0.010}_{-0.015}$
Hα	$-0.711^{+0.038}_{-0.039}$	$0.894^{+0.048}_{-0.047}$	$6562.727^{+0.023}_{-0.023}$
Li I resonance line	$-0.050^{+0.012}_{-0.017}$	$1.78^{+0.17}_{-0.82}$	$6708.43^{+0.37}_{-1.30}$

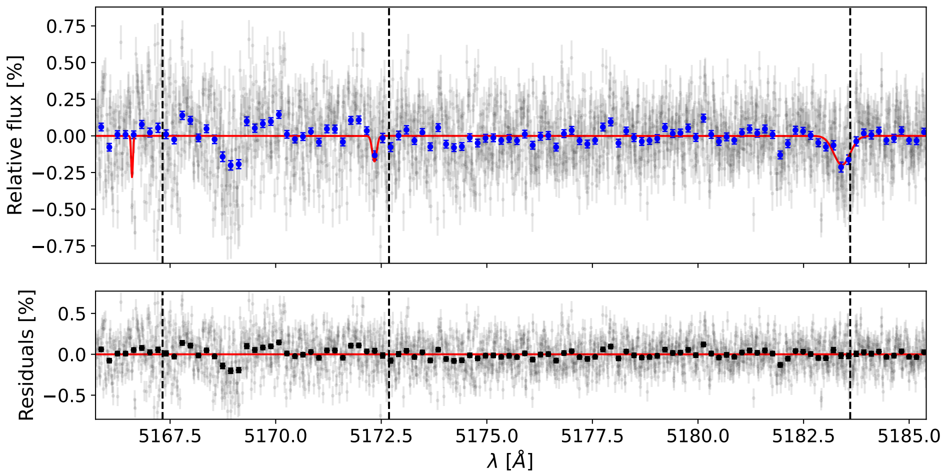

FIGURE 5.1: In the upper panel is shown the combined transmission spectrum data points (grey dots) and the x20 binned data (blue dots) plotted with the best-fit Gaussian models to the Mg I b triplet lines, shown by the solid red line. The lower panel contains the residuals from the Gaussian fit with a red line to indicate the 0 level.

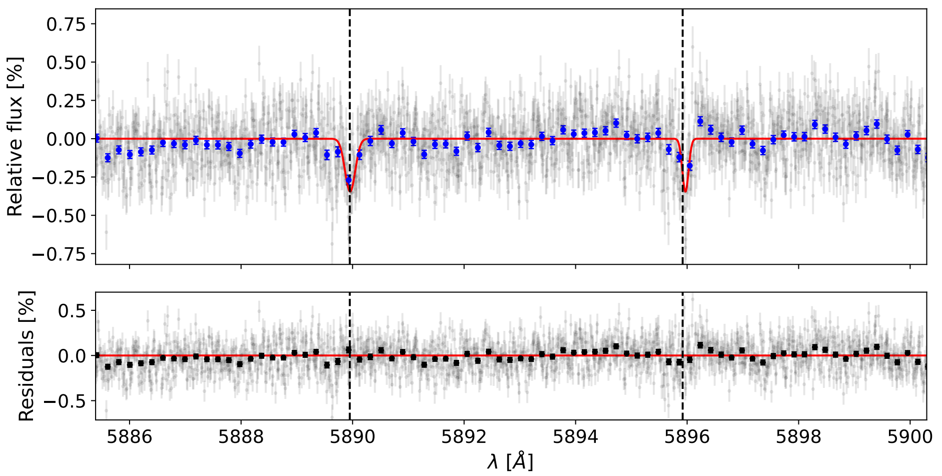

FIGURE 5.2: Same as Figure 5.1 for the Na I D doublet lines.

The probability distributions of the Li I and Mg I b2 and b2 lines' parameters did not converge and the final parameters were not determined, indicating their non-detection on our data set. A useful way of displaying the lines is by translating the wavelength axis into velocity shift from the reference wavelength value and by converting the absorption depth into the equivalent height, with the formulation in Equation 2.10. For singular lines, this process is a simple conversion, yet for multiple lines, as was the case for the sodium doublet, we co-added them by averaging in the velocity grids with reference on each line. Figures 5.5 to 5.7 show the relative height R_{atm} in function of velocity shift for the Mg I b1, Hα and co-added Na I D doublet lines, plotted with the instrumental broadening (2 km s^{-1}) and the escape velocity (Equation 1.7) for comparison. The Gaussian line fits

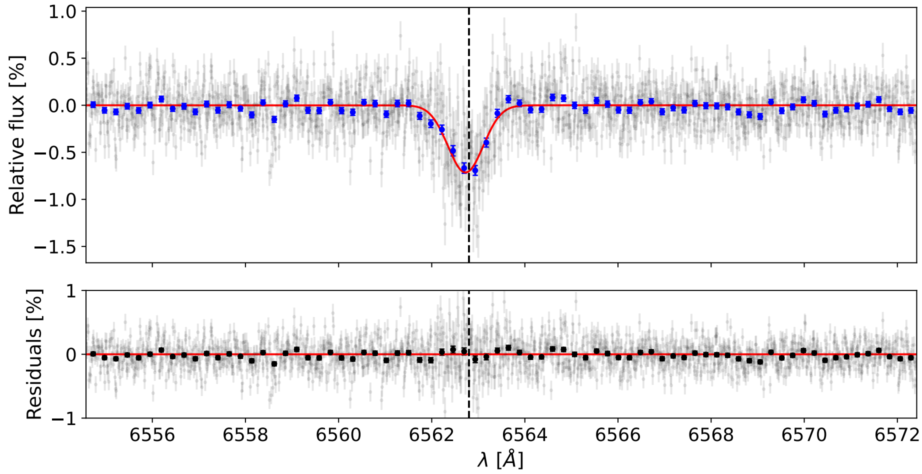

FIGURE 5.3: Same as Figure 5.1 for the Hα line.

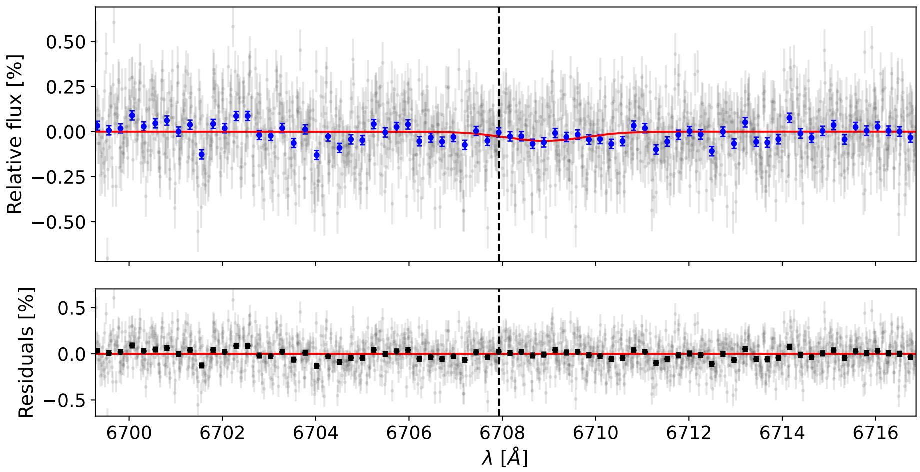

FIGURE 5.4: Same as Figure 5.1 for the Li I resonance line.

TABLE 5.3: Derived properties of the line fits from the retrieved parameters presented in Table 5.2.

	Amplitude [σ]	FWHM [km s^{-1}]	Line centre [km s^{-1}]
Mg I b3	1.0	$4.9^{+49.7}_{-1.9}$	$-40.4^{+61.2}_{-1.6}$
Mg I b2	2.3	$10.6^{+15.8}_{-5.5}$	$-18.6^{+11.4}_{-2.2}$
Mg I b1	6.4	$27.6^{+5.6}_{-4.5}$	$-10.3^{+2.0}_{-2.3}$
Na I D2	5.3	$12.2^{+5.4}_{-2.8}$	$0.1^{+0.8}_{-1.1}$
Na I D1	5.8	$7.0^{+2.0}_{-2.2}$	$2.50^{+0.52}_{-0.76}$
Hα	19	$40.8^{+2.2}_{-2.1}$	$-3.4^{+1.0}_{-1.0}$
Li I resonance line	4.1	$79.4^{+7.7}_{-37.8}$	22^{+17}_{-58}

were made once again, resulting in slightly different parameters due to fitting in velocity space instead of wavelength space, however, all are compatible within 3 σ. Notably, the co-added Na I D lines yielded a height with a significance of 11 σ. The signals of Mg I, Na I and Hα extend for 15, 22 and 49 scale heights, which we predict to be high enough for pressure broadening to be negligible. The differences between each line can be an indication of varying atmospheric dynamics, as will be discussed further in Chapter 6.

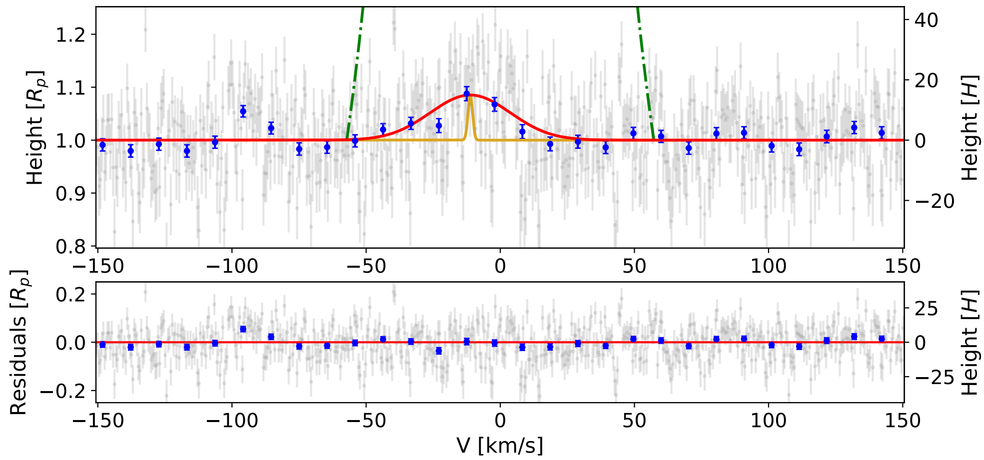

FIGURE 5.5: Combined transmission spectrum data points (grey dots) and the x20 binned data (blue dots) plotted in terms of the atmosphere's height in function of Doppler shift. The height is shown both in units of the planet's radius, R_p, and in scale heights, H. The best-fit Gaussian models to the Mg I b1 line are represented by the solid red line. The green dot-dashed line corresponds to the escape velocity, while the solid yellow line illustrates the resolution of ESPRESSO. The lower panel contains the residuals from the Gaussian fit with a red line to indicate the 0 level.

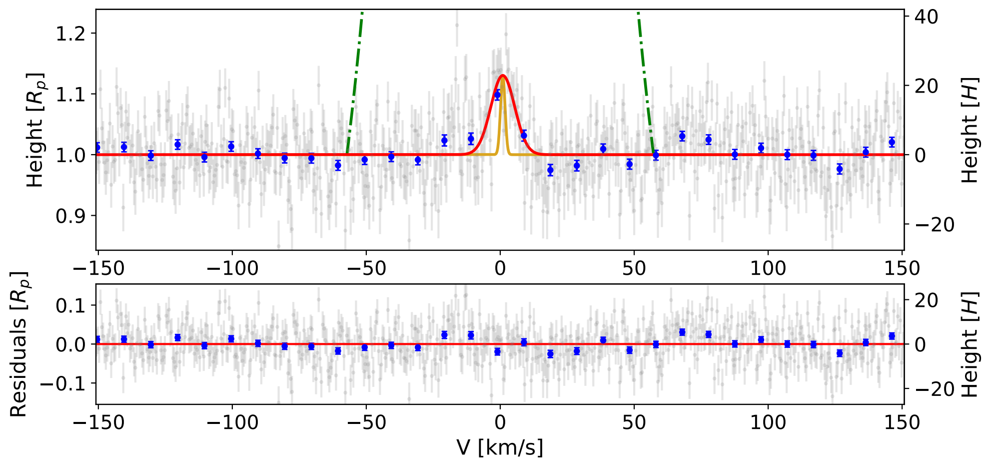

FIGURE 5.6: Same as Figure 5.5 for the co-added Na I D doublet lines.

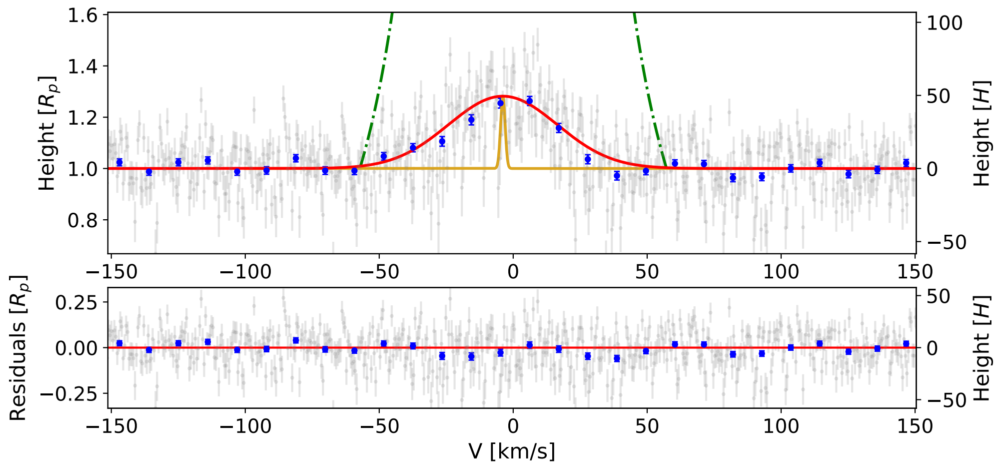

FIGURE 5.7: Same as Figure 5.5 for the Hα line.

5.1 Relative lightcurves

A method of increasing the signal while still being able to study the planetary features temporally is binning in the wavelength direction, forming a relative lightcurve by sacrificing spectral resolution (Wyttenbach et al., 2015; Seidel et al., 2019). This can be done by averaging the data points within a wavelength interval centred around the target absorption line(s) to have a better determined mean absorption depth and subsequently binning these values by a number of exposures. During the wavelength binning it is convenient to divide the mean absorption by the local continuum, defined by adjacent intervals. We performed this succession of processes for all detected lines, using the bands specified in Table 5.4. The Li I resonance line was not included in this analysis due to its non-detection, as well as the Mg I b2 and b3 lines, however, we still employed it for the Mg I b1 line. The Na I D doublet lines were inserted in the same 12 Å wide absorption band. Even binning in wavelength and in phase, the signals are weak and very sensitive to how the continuum is determined, for this reason, the bands were chosen carefully to minimise the effect of the wiggles on the lightcurves of Na I. For each set of bands, we obtained the spectra's mean relative absorption for both nights and arranged them in Figures 5.8 to 5.10. The two transits' data are graphed separately and then together, to inspect any variations between them.

The relative lightcurve of Mg I shows scattered absorption levels which may indicate the presence of stellar contamination, possibly behind the detection of the Mg I b1 line. For the Li I line, we notice similar results, with the points scattered around 0 indicating a lack of an absorption signal. The results for Na I and Hα show clearer signals. Curiously,

Table 5.4: Absorption and continuum bands used to create the relative lightcurves for each set of lines.

	Absorption band	Continuum bands
Mg I b1	[5180.6, 5186.6]	[5174.6, 5180.6] and [5186.6, 5192.6]
Na I D doublet	[5886.9, 5898.9]	[5880.9, 5886.9] and [5898.9, 5904.9]
Hα	[6557.8, 6567.8]	[6547.8, 6557.8] and [6567.8, 6577.8]
Li I resonance line	[6704.9, 6710.9]	[6699.9, 6704.9] and [6710.9, 6715.9]

Note: Due to the non-detection of the Mg I b2, Mg I b3 and Li I resonant lines, we did not build the relative lightcurve for these elements.

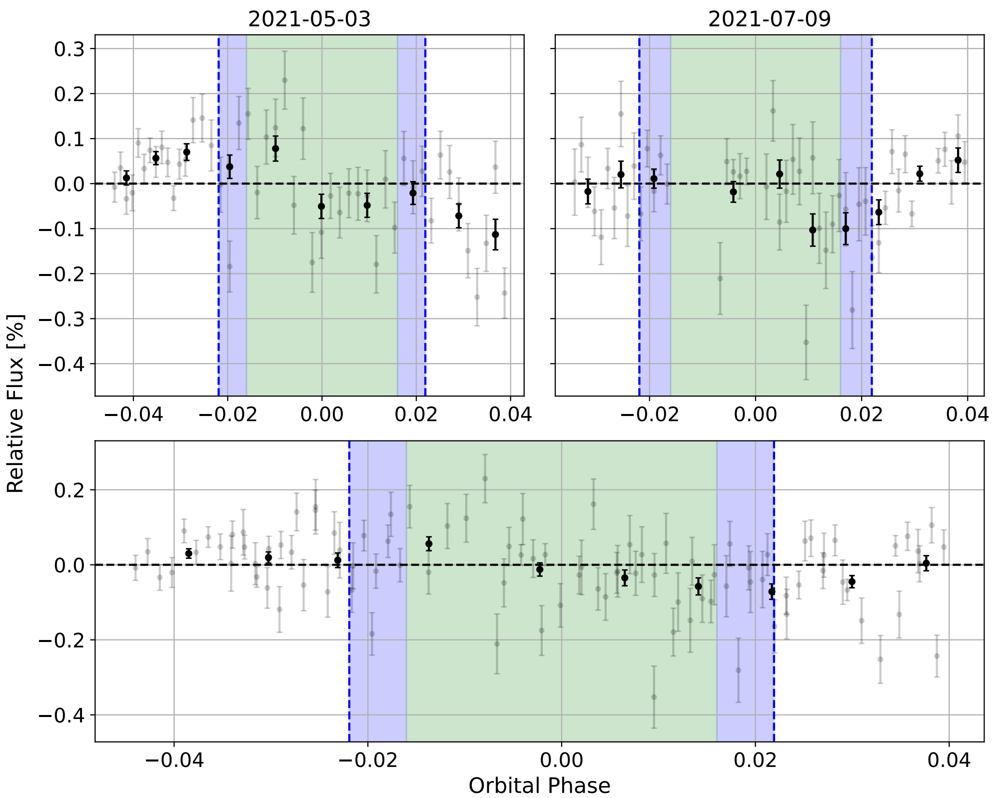

Figure 5.8: Relative lightcurves of the Mg I b1 line. The top panels show the relative absorption in each exposure in grey along with the x5 binned points in black for the nights 2021 May 05 and 2021 July 09, respectively from left to right. The bottom panel contains the joint data in grey and the x10 binned points marked as black. The dashed lines mark the start and finish of transit, at the first and fourth contact points. The central green shade marks the phases between the second and third contact points, with the blue-shaded regions indicating ingress and egress.

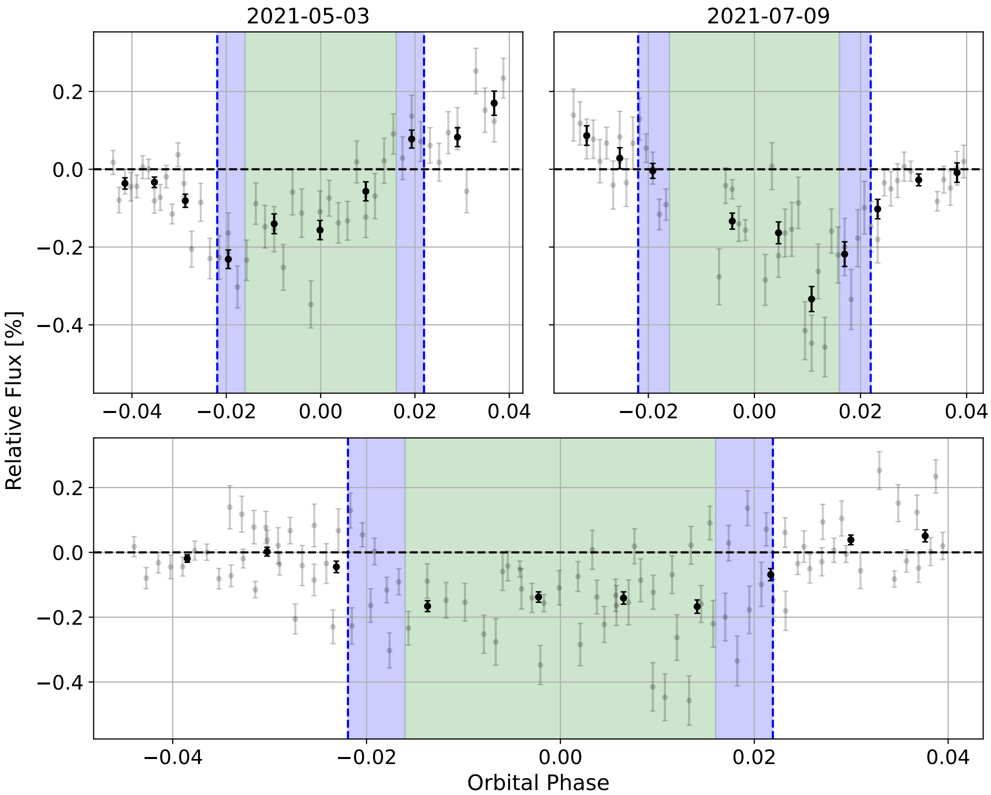

FIGURE 5.9: Same as Figure 5.8 for the Na I D doublet lines.

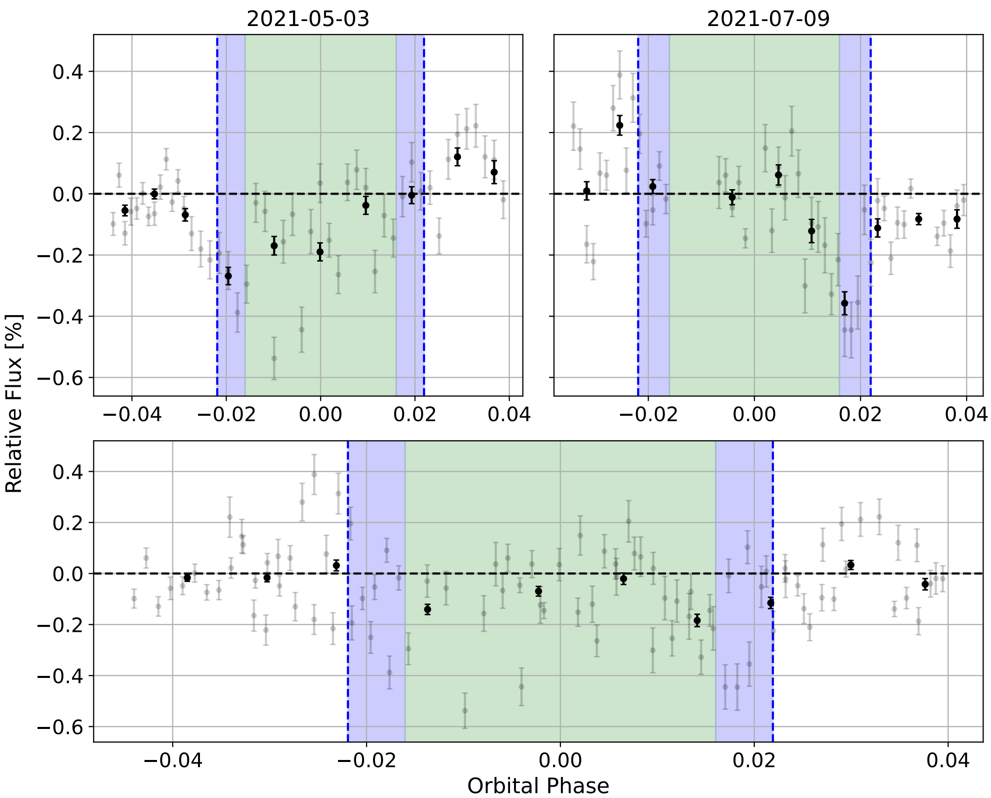

FIGURE 5.10: Same as Figure 5.8 for the Hα line.

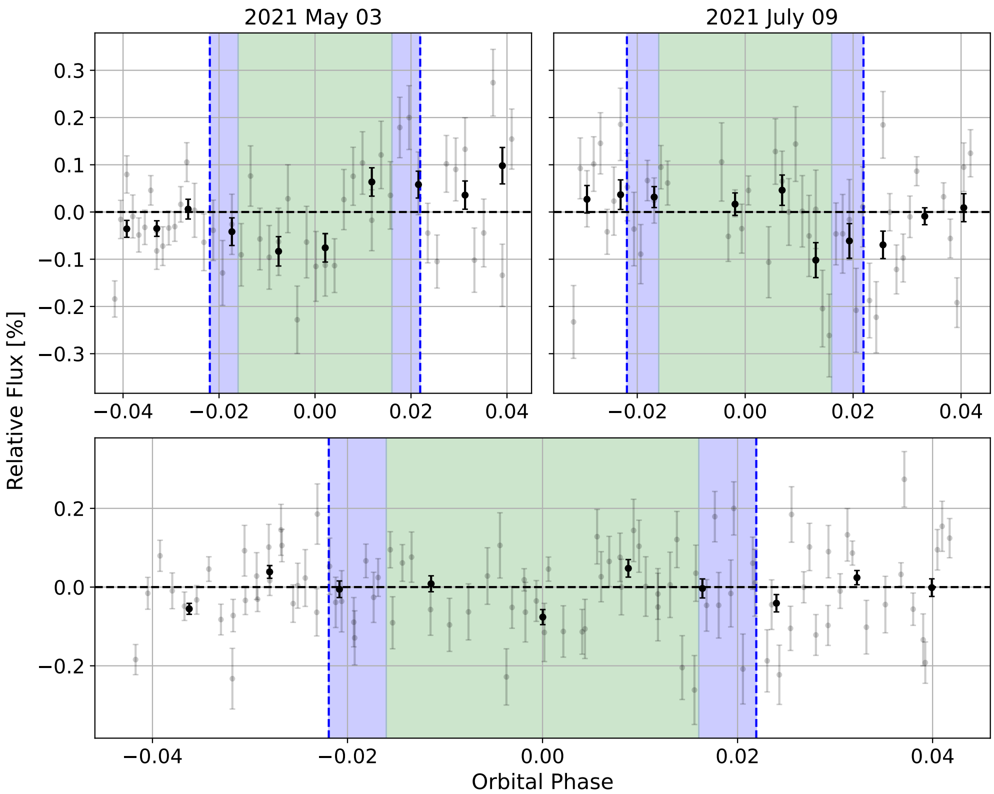

FIGURE 5.11: Same as Figure 5.8 for the Li I resonance line.

during the first transit, the absorptions are largest in the first half, while the opposite is verified during the second transit, although we cannot draw conclusions from the first half of the transit due to the removed spectra. The joint plot reveals lower absorptions near the transit centre. These results provide some insight into the temporal variation of the absorption depths, however, they are merely indicative due to the large scatter and weak signal.

5.2 Bootstrapping verification

In order to validate the previous detections we employed an empirical Monte Carlo (EMC) method. The EMC or bootstrapping methods conducted follow the procedure described in Redfield et al. (2008) and are used frequently in exoplanet atmospheres studies, such as in Wyttenbach et al. (2015); Seidel et al. (2019, 2022, 2023); Casasayas-Barris et al. (2020, 2021); Sedaghati et al. (2021). The procedure is designed to verify whether the signal observed is of planetary origin or if it is caused by systematic errors or spurious signals in the data. If the detections are in fact of planetary origin they should be found in the difference between the in-transit and the out-of-transit exposures. Following the same logic, in the absence of systematic error, we expect there to be no difference between the out-of-transit spectra as well as between the in-transit spectra, on average.

The EMC method consists of generating three simulated scenarios, each with virtual in-transit and out-of-transit data. In the first scenario, we sample with repetition from our in-transit set of spectra to form the virtual in-transit set and sample from the real out-of-transit into the virtual out-of-transit. This is the 'in-out' scenario and it simulates what we expect from the transmission spectroscopy. The second scenario is the 'out-out', in which we generate both virtual in- and out-of-transit sets from the real out-of-transit data. The third 'in-in' scenario is similar to the previous, consisting of only in-transit data. For the last two scenarios, we expect not to see any absorption signal in their transmissions. Since fluctuations are natural between exposures, the relative absorption will be close to 0 with some variance. Due to this and by repeating the sampling and mean absorption calculation over several iterations we should have distributions for each scenario centered around the mean absorption. Assuming white noise dominated data the distributions are essentially described by a normal distribution or Gaussian profile. The absorption for each sample is calculated in a similar way as described in Section 5.1 for the relative lightcurves.

We carried out the verification by forming virtual in- and out-of-transit sets with 18 spectra each, sampled with repetition from each night's spectra, separately. The absorption of the three scenarios was calculated for 10.000 iterations and the distributions were fitted with Gaussian profiles to retrieve their amplitude, centre and standard deviation parameters. The fit was done using the `Scipy` least squares fitting algorithm `curve_fit`. One of the important quantities to extract from this analysis is the standard deviation of the out-out distributions $\sigma_{\text{out}-\text{out}}$ since it depicts the absorption levels that can be measured from a non-planetary origin. When corrected for the real number of in- and out-of-transit spectra, N_{in} and N_{out} respectively, as described in Equation 5.1 we obtain the false-positive probability $\mathcal{P}_{\text{FP}}$.

$$\mathcal{P}_{\text{FP}} = \sigma_{\text{out}-\text{out}} \sqrt{\frac{N_{\text{out}}}{N_{\text{out}} + N_{\text{in}}}} \tag{5.1}$$

The bands used to calculate the mean absorption are the same as used in Section 5.1 listed in Table 5.4.

The results of the bootstrap analysis are shown in Figures 5.12 to 5.15. In all cases we verify the 'in-in' and 'out-out' distributions are all centred around 0, deviating at most

0.005%, corresponding to non-detections, as was expected. For the Na I and Hα the 'in-out' distributions are considerably deviated from 0, by at least -0.17 and -0.14 % respectively, which is beyond their false-positive probabilities (at most 0.044 and 0.058 %). This suggests the signals are indeed of planetary origin and not caused by systematic errors. For Mg I, however, the 'in-out' distributions are centred at -0.010 and 0.012 %, with the first night's distributions slightly shifted to the negative or absorption side and the second night's shifted to the positive or emission side, both within their $\mathcal{P}_{\rm FP}$ (0.043 %). This provides further evidence of either a lack of Mg I in the atmosphere of WASP-178 b or the presence of a signature too faint to be properly detected with our observations. The main results of the fit to the distributions are presented in Table 5.5. The results for the Li I resonance line are similar to those for the Mg I b1 line, with the distributions centred around -0.016 and 0.018 %, with a false-positive probability of at least 0.033 %. These results support once again the absence of systematic error as well as a non-detection of lithium in the planet's atmosphere. We use the two nights' derived false-positive probabilities, averaged quadratically and propagated with the positive uncertainty, σ_{A+}, of the respective line's fitted amplitude A, to obtain the detection level of each line as $\frac{A}{\sqrt{\sigma_{A+}^2 + \sum_{i=1}^{N_n=2}(\mathcal{P}_{\rm FP,\ i}/N_n)^2}}$, with N_n representing the number of observed nights. In Table 5.6 the final detection levels are presented for all lines, excluding the Mg I b2 and b3 lines.

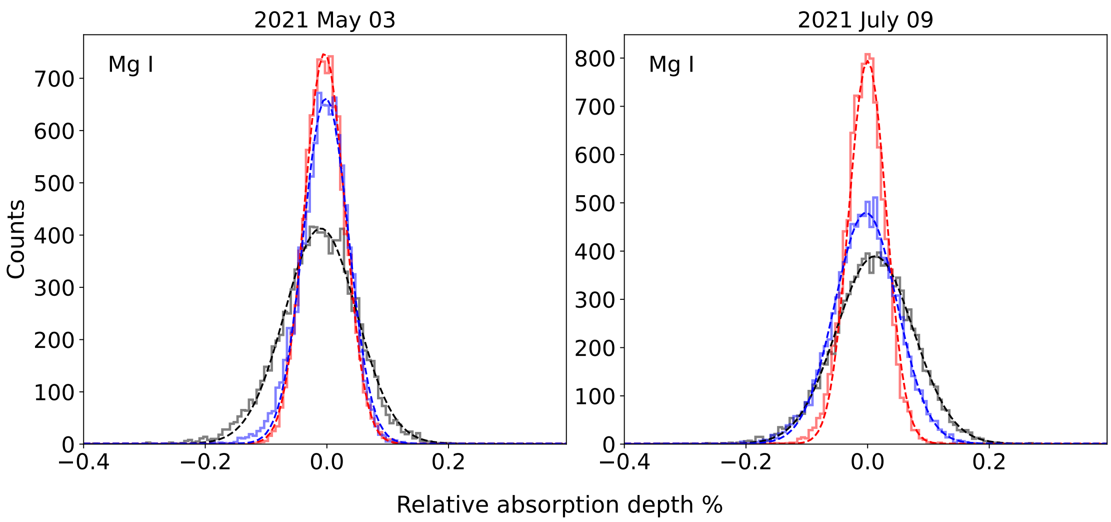

FIGURE 5.12: Distributions of the empirical Monte Carlo analysis for the Mg I b1 line on the first (left panel) and second (right panel) nights' spectra. The 'in-in', 'out-out' and 'in-out' distributions are marked in red, blue and black, respectively. The Gaussian profile fits are plotted as dashed lines with the corresponding colour.

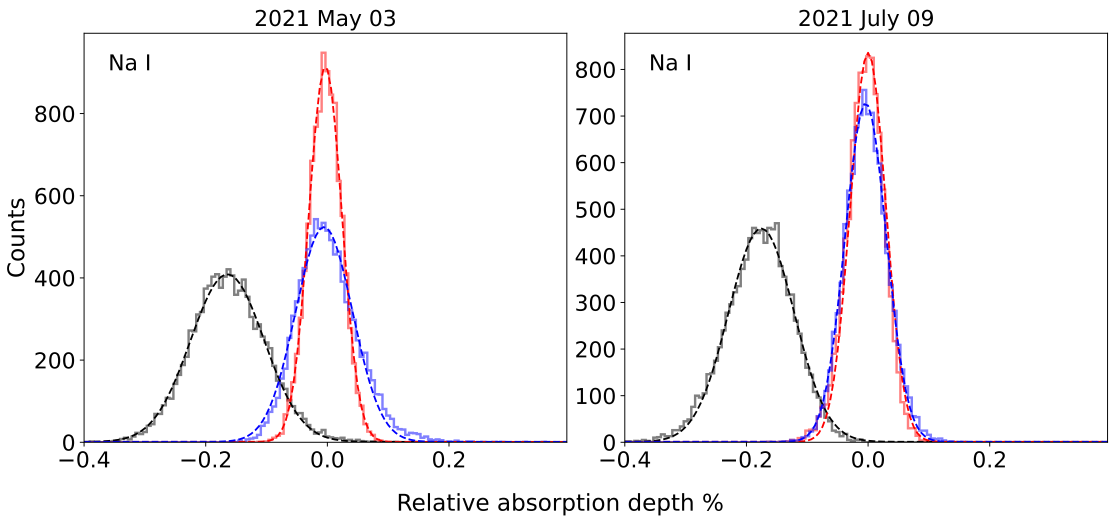

FIGURE 5.13: Same as Figure 5.12 for the Na I D doublet lines.

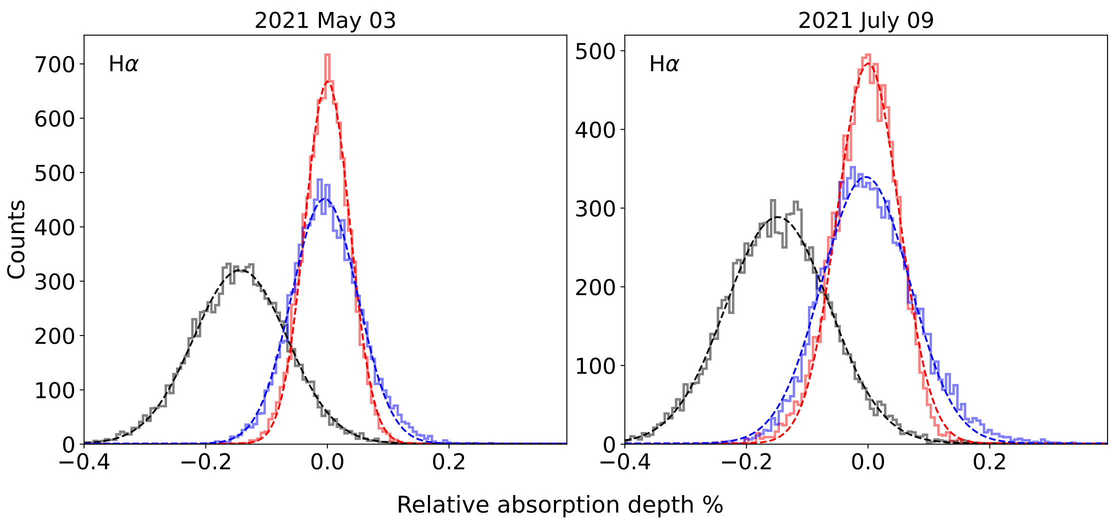

FIGURE 5.14: Same as Figure 5.12 for the Hα line.

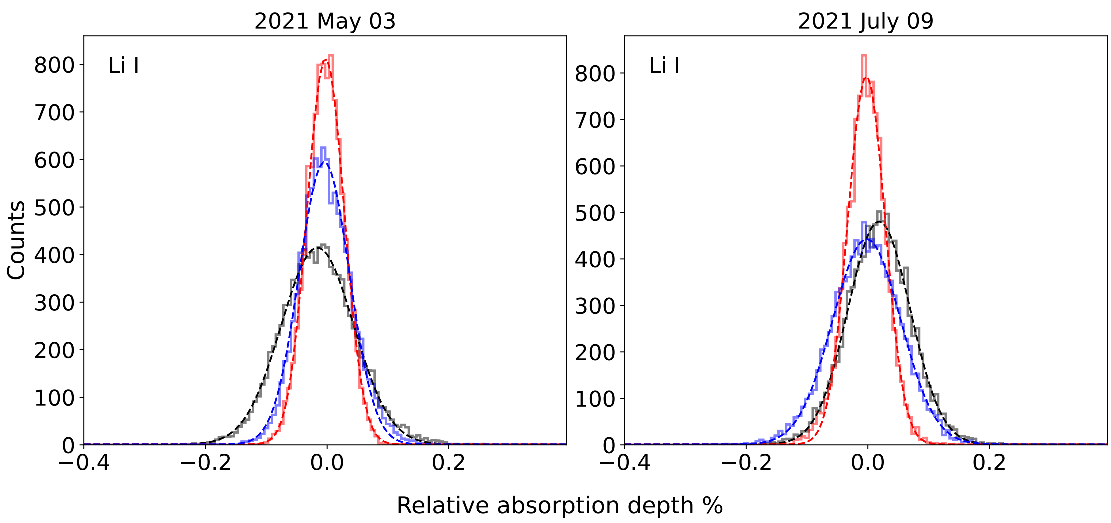

FIGURE 5.15: Same as Figure 5.12 for the Li I resonance line.

TABLE 5.5: Principal results from the Gaussian fit to the bootstrap distributions.

		in-out centre [%]	$\sigma_{out-out}$ [%]	$\mathcal{P}_{\mathrm{FP}}$ [%]
Mg I b1	2021 May 03	-0.010	0.059	0.043
	2021 July 09	0.012	0.063	0.043
Na I	2021 May 03	-0.17	0.061	0.044
	2021 July 09	-0.18	0.054	0.037
Hα	2021 May 03	-0.14	0.077	0.056
	2021 July 09	-0.15	0.085	0.058
Li I resonance line	2021 May 03	-0.016	0.060	0.043
	2021 July 09	0.018	0.051	0.033

Note: The false-positive probability displayed was derived from the fitted 'out-out' standard deviation $\sigma_{\mathrm{out-out}}$.

TABLE 5.6: Detection levels of the spectral lines analysed with the bootstrapping method.

	Detection level
Mg I b1	4.6
Na I D2	4.8
Na I D1	5.2
Na I co-added	7.5
Hα	13
Li I resonance line	<3

Chapter 6

Conclusions and future work

The results gathered from the narrow-band spectroscopy reveal the presence of sodium and hydrogen in the atmosphere of WASP-178 b via the detection of the Na I D2 (4.8 σ detection level), Na I D1 (5.2 σ) and Hα (13 σ) lines, taking into account the detection level of the Na I doublet increased to 7.5 σ by co-adding the lines. Despite the Mg I b1 line's detection level of 4.6 σ, several doubts are risen regarding the detection of magnesium in the atmosphere. The absence of the remaining b triplet lines (both b2 and b3 below 3 σ), along with the inconclusive lightcurve and bootstrapping results impede us from claiming the existence of magnesium with confidence. With all factors in mind, we claim a tentative Mg I detection, requiring further investigation to confidently verify or refute this. We report as well the non-detection of Li I (below 3 σ) supported by the bootstrapping and relative lightcurve results, which is curious as this species has been found in other similar UHJ atmospheres, such as those of WASP-121 b (Borsa et al., 2021) and WASP-76 b (Tabernero et al., 2021) and its search for our target is aided by the lack of a lithium absorption feature from the star which leads to an absence of the RM effect signature or from reduced S/N due to reduced flux at the line centre. The non-detection may be due to insufficient S/N of our observations. In a previous study of WASP-121 b based on 1-UT and 4-UT data, the Li I resonance line was only detected on the high-quality 4-UT data, without being found on the 1-UT observations (Borsa et al., 2021).

The detected lines reveal different overall behaviours, connected by certain common traits. We notice the broadening of the detected lines is far larger than the instrumental and thermal broadening values. The least broadened of the detected lines are the Na I D2 and D1 lines with FWHM values of $12.2^{+5.4}_{-2.8}$ km s^{-1} and $7.0^{+2.0}_{-2.2}$ km s^{-1}, which are 3.3 σ

and 1.8 σ larger than their respective thermal broadening values at the equilibrium temperature reported in Hellier et al. (2019). The most broadened lines are Hα and the Mg I b1 line with FWHM of $40.8^{+2.2}_{-2.1}$ km s^{-1} and $27.6^{+5.6}_{-4.5}$ km s^{-1} which stand 12 σ and 5.5 σ above their expected thermal broadening. Regarding the line centres, we find varying results as well. The Na I doublet lines are barely shifted, with the D2 line essentially at its rest frame position ($0.1^{+0.8}_{-1.1}$ km s^{-1}) and the D2 line slightly redshifted by $2.50^{+0.52}_{-0.76}$ km s^{-1}, although consistent with 0 within 3.3 σ. The Hα line shows a slight blueshift of $3.4^{+1.0}_{-1.0}$, as well consistent with 0 within 3.4 σ. The most shifted line is the Mg I b1 line, off by $-10.3^{+2.0}_{-2.3}$, corresponding to a blueshift significant by 5.1 σ. These results provide evidence of atmospheric dynamics and high-speed winds, however not homogeneously across the atmosphere. Considering the various detected lines exist in different layers of the atmosphere the discrepancies between the retrieved properties might serve to understand the overall dynamics at different regions. The strongest line, Hα, is also produced by the lightest element and thus originates the highest up in the atmosphere, followed by the strong Na I D doublet and consecutively the Mg I b1 line, at the middle to lower regions. From Figures 5.5 to 5.7 we estimate the Hα line to be produced up to around 1.3 R_p, or 50 scale heights. We may observe from these plots that the fastest moving hydrogen particles exceed the escape velocity of $\sim$ 50 km s^{-1} around these altitudes. For FWHM values consistent with our results up to 5 σ, we estimate that at most 2.5% of particles have speeds above the escape velocity at the altitude of 1.3 R_p. This reveals the possibility of atmospheric escape of the lighter elements residing in the highest layers, which can be associated with the large observed broadening. For magnesium, however, this scenario is far less likely meaning other mechanisms must be driving the broadening and blueshift of its absorption features. In between these two layers, probed by the Na I D doublet, we notice relatively low broadening and shift, suggesting a lack of strong dynamics in this region.

Curiously, the Doppler shifts measured both by the line centres and widths indicate relatively weak dynamics when compared to other UHJ exoplanets. This discrepancy raises the question of whether winds are a global population feature for UHJ or if there are other factors involved. This opens up pathways for further research on UHJ atmospheres as a population study.

Recent results of emission spectroscopy on WASP-178 b using CRIRES+ data (Cont et al. 2024 in preparation, private communication) hint at strong winds in the lower layers of the atmosphere manifested by broad absorption features of H_2O and CO. Assuming the Mg I b1 line to stand, this suggests the existence of a gradient of wind speed, from strong lower layer winds to a slower moving mid-to-upper region and an escaping upper layer. Recent research on WASP-178 b revealed evidence for efficient energy recirculation (Pagano et al., 2023). This high recirculation was associated with the existence of zonal winds from the dayside to the nightside through the use of global circulation models (GCM) from Kataria et al. (2016). The relation between efficient day-to-nightside recirculation and the high irradiation of UHJ has been predicted by Zhang et al. (2018) and goes in agreement with the results obtained by Pagano et al. (2023). Zonal day-to-nightside winds are expected to cause a blueshift on absorption features, which we cannot confidently support. The clear broadening of our detected lines, on the other hand, supports rotational winds and, possibly, an expansion movement considering the scenario of atmospheric escape. Further observations would be necessary to better constrain these dynamical properties.

The verification steps covered in Sections 5.1 and 5.2 contain hints towards the temporal variation of the studied absorption features. Asymmetries in the absorption depth between both nights and throughout each transit were present in the relative lightcurves, raising questions when it comes to the distribution of the material in the atmosphere. Considering different portions of the planet are probed during a transit we can associate these asymmetries with distinct atmospheric compositions or distributions between the morning and evening terminators. The dispersion of absorption depths during transit is also manifested in the bootstrapping method, concretely in the 'in-in' distributions, as its width reflects the dispersion of absorption values between in-transit spectra. We notice the 'in-in' distributions are wider on the second night for all the cases, becoming even 1.4 times wider than the first night's distribution for Hα.

When it comes to future work multiple research paths are open and worth exploring. In the short-term, the current data can be explored to a larger extent adding further atomic species to the search in narrow-band, as well as expanding the study with the cross-correlation technique. Given the intriguing results presented here along with recent research, longer-term work includes follow-up observations of WASP-178 b transits. As a future James Webb Space Telescope (JWST) target, WASP-178 b is subject to interest from the science community and being able to determine atmospheric properties would be beneficial for current and future research on the target. With our lightcurve results hinting at possibly a variable absorption depth with time and our line fits suggesting a stratification regarding dynamics, we have a foundation for future observing proposals to properly resolve the imprints of WASP-178 b's atmosphere. Additional high-resolution 1-UT observations would allow us to resolve more atomic lines from different layers of the atmosphere in order to further enrich our knowledge of the composition of UHJ atmospheres. We may as well take advantage of the very high S/N of a 4-UT observation to better determine the absorption features' properties and from these derive the behaviour of the atmosphere. High S/N data can also be used to confirm our non-detections in narrow-band, such as lithium, and help to clarify the presence of magnesium. With such high-quality data, we would be able to study atmospheric dynamics through the application of GCM. These paths could be encompassed in a possible doctoral thesis project to follow.

Bibliography

W. S. Adams and J. Dunham, T., “Absorption Bands in the Infra-Red Spectrum of Venus,” , vol. 44, no. 260, pp. 243–245, Aug. 1932. [Cited on page 1.]

D. Charbonneau, T. M. Brown, R. W. Noyes, and R. L. Gilliland, “Detection of an Extrasolar Planet Atmosphere,” , vol. 568, no. 1, pp. 377–384, Mar. 2002. [Cited on pages 2, 14, and 37.]

I. A. G. Snellen, S. Albrecht, E. J. W. de Mooij, and R. S. Le Poole, “Ground-based detection of sodium in the transmission spectrum of exoplanet HD 209458b,” , vol. 487, no. 1, pp. 357–362, Aug. 2008. [Cited on pages 2, 8, and 37.]

A. Vidal-Madjar, A. Lecavelier des Etangs, J. M. Désert, G. E. Ballester, R. Ferlet, G. Hébrard, and M. Mayor, “An extended upper atmosphere around the extrasolar planet HD209458b,” , vol. 422, no. 6928, pp. 143–146, Mar. 2003. [Cited on page 2.]

A. Vidal-Madjar, J. M. Désert, A. Lecavelier des Etangs, G. Hébrard, G. E. Ballester, D. Ehrenreich, R. Ferlet, J. C. McConnell, M. Mayor, and C. D. Parkinson, “Detection of Oxygen and Carbon in the Hydrodynamically Escaping Atmosphere of the Extrasolar Planet HD 209458b,” , vol. 604, no. 1, pp. L69–L72, Mar. 2004. [Cited on page 2.]

S. Redfield, M. Endl, W. D. Cochran, and L. Koesterke, “Sodium Absorption from the Exoplanetary Atmosphere of HD 189733b Detected in the Optical Transmission Spectrum,” , vol. 673, no. 1, p. L87, Jan. 2008. [Cited on pages 2 and 75.]

D. Ehrenreich, G. Tinetti, A. Lecavelier Des Etangs, A. Vidal-Madjar, and F. Selsis, “The transmission spectrum of Earth-size transiting planets,” , vol. 448, no. 1, pp. 379–393, Mar. 2006. [Cited on page 2.]

D. Ehrenreich, A. Vidal-Madjar, T. Widemann, G. Gronoff, P. Tanga, M. Barthélemy, J. Lilensten, A. Lecavelier Des Etangs, and L. Arnold, "Transmission spectrum of Venus as a transiting exoplanet," , vol. 537, p. L2, Jan. 2012. [Cited on page 2.]

A. Wyttenbach, D. Ehrenreich, C. Lovis, S. Udry, and F. Pepe, "Spectrally resolved detection of sodium in the atmosphere of HD 189733b with the HARPS spectrograph," , vol. 577, p. A62, May 2015. [Cited on pages 2, 7, 8, 19, 26, 72, and 75.]

K. Heng, A. Wyttenbach, B. Lavie, D. K. Sing, D. Ehrenreich, and C. Lovis, "A Non-isothermal Theory for Interpreting Sodium Lines in Transmission Spectra of Exoplanets," , vol. 803, no. 1, p. L9, Apr. 2015. [Cited on pages 2 and 8.]

L. Pino, D. Ehrenreich, A. Wyttenbach, V. Bourrier, V. Nascimbeni, K. Heng, S. Grimm, C. Lovis, M. Malik, F. Pepe, and G. Piotto, "Combining low- to high-resolution transit spectroscopy of HD 189733b. Linking the troposphere and the thermosphere of a hot gas giant," , vol. 612, p. A53, Apr. 2018. [Cited on page 2.]

Seidel, J. V, "Exoplanet winds: Modelling atmospheric dynamics via resolved spectral lines," Geneva, CH, Standard doi: 10.13097/archive-ouverte/unige:152927, 2021. [Online]. Available: https://archive-ouverte.unige.ch//unige:152927 [Cited on pages xi, 2, and 21.]

T. Azevedo Silva, O. D. S. Demangeon, N. C. Santos, R. Allart, F. Borsa, E. Cristo, E. Esparza-Borges, J. V. Seidel, E. Palle, S. G. Sousa, H. M. Tabernero, M. R. Zapatero Osorio, S. Cristiani, F. Pepe, R. Rebolo, V. Adibekyan, Y. Alibert, S. C. C. Barros, F. Bouchy, V. Bourrier, G. Lo Curto, P. Di Marcantonio, V. D'Odorico, D. Ehrenreich, P. Figueira, J. I. González Hernández, C. Lovis, C. J. A. P. Martins, A. Mehner, G. Micela, P. Molaro, D. Mounzer, N. J. Nunes, A. Sozzetti, A. Suárez Mascareño, and S. Udry, "Detection of barium in the atmospheres of the ultra-hot gas giants WASP-76b and WASP-121b. Together with new detections of Co and Sr+ on WASP-121b," , vol. 666, p. L10, Oct. 2022. [Cited on pages 2, 9, and 11.]

G. W. Henry, G. W. Marcy, R. P. Butler, and S. S. Vogt, "A Transiting "51 Peg-like" Planet," , vol. 529, no. 1, pp. L41–L44, Jan. 2000. [Cited on page 3.]

D. Charbonneau, T. M. Brown, D. W. Latham, and M. Mayor, "Detection of Planetary Transits Across a Sun-like Star," , vol. 529, no. 1, pp. L45–L48, Jan. 2000. [Cited on page 3.]

I. de Pater and J. J. Lissauer, *Planetary Sciences*, 2nd ed. Cambridge University Press, 2015. [Cited on pages 3, 26, and 27.]

J. N. Winn, J. A. Johnson, N. Narita, Y. Suto, E. L. Turner, D. A. Fischer, R. P. Butler, S. S. Vogt, F. T. O'Donovan, and B. S. Gaudi, "The prograde orbit of exoplanet tres-2b*," *The Astrophysical Journal*, vol. 682, no. 2, p. 1283, aug 2008. [Online]. Available: https://dx.doi.org/10.1086/589235 [Cited on pages 4 and 37.]

J. N. Winn, "Exoplanet Transits and Occultations," in *Exoplanets*, S. Seager, Ed., 2010, pp. 55–77. [Cited on pages xi and 4.]

N. C. Santos, S. C. C. Barros, O. D. S. Demangeon, and J. P. Faria, "Detection and Characterization Methods of Exoplanets," in *Oxford Research Encyclopedia of Planetary Science*, 2020, p. 189. [Cited on page 5.]

F. Pepe, S. Cristiani, R. Rebolo, N. C. Santos, H. Dekker, A. Cabral, P. Di Marcantonio, P. Figueira, G. Lo Curto, C. Lovis, M. Mayor, D. Mégevand, P. Molaro, M. Riva, M. R. Zapatero Osorio, M. Amate, A. Manescau, L. Pasquini, F. M. Zerbi, V. Adibekyan, M. Abreu, M. Affolter, Y. Alibert, M. Aliverti, R. Allart, C. Allende Prieto, D. Álvarez, D. Alves, G. Avila, V. Baldini, T. Bandy, S. C. C. Barros, W. Benz, A. Bianco, F. Borsa, V. Bourrier, F. Bouchy, C. Broeg, G. Calderone, R. Cirami, J. Coelho, P. Conconi, I. Coretti, C. Cumani, G. Cupani, V. D'Odorico, M. Damasso, S. Deiries, B. Delabre, O. D. S. Demangeon, X. Dumusque, D. Ehrenreich, J. P. Faria, A. Fragoso, L. Genolet, M. Genoni, R. Génova Santos, J. I. González Hernández, I. Hughes, O. Iwert, F. Kerber, J. Knudstrup, M. Landoni, B. Lavie, J. Lillo-Box, J. L. Lizon, C. Maire, C. J. A. P. Martins, A. Mehner, G. Micela, A. Modigliani, M. A. Monteiro, M. J. P. F. G. Monteiro, M. Moschetti, M. T. Murphy, N. Nunes, L. Oggioni, A. Oliveira, M. Oshagh, E. Pallé, G. Pariani, E. Poretti, J. L. Rasilla, J. Rebordão, E. M. Redaelli, S. Santana Tschudi, P. Santin, P. Santos, D. Ségransan, T. M. Schmidt, A. Segovia, D. Sosnowska, A. Sozzetti, S. G. Sousa, P. Spanò, A. Suárez Mascareño, H. Tabernero, F. Tenegi, S. Udry, and A. Zanutta, "ESPRESSO at VLT. On-sky performance and first results," , vol. 645, p. A96, Jan. 2021. [Cited on page 6.]

J. V. Seidel, F. Borsa, L. Pino, D. Ehrenreich, M. Stangret, M. R. Zapatero Osorio, E. Palle, Y. Alibert, R. Allart, V. Bourrier, P. Di Marcantonio, P. Figueira, J. I. González Hernández, J. Lillo-Box, C. Lovis, C. J. A. P. Martins, A. Mehner, P. Molaro, N. J. Nunes,

F. Pepe, N. C. Santos, and A. Sozzetti, "Detection of a high-velocity sodium feature on the ultra-hot Jupiter WASP-121 b," , vol. 673, p. A125, May 2023. [Cited on pages 7, 10, 11, 28, 33, and 75.]

D. Deming, A. Wilkins, P. McCullough, A. Burrows, J. J. Fortney, E. Agol, I. Dobbs-Dixon, N. Madhusudhan, N. Crouzet, J.-M. Desert, R. L. Gilliland, K. Haynes, H. A. Knutson, M. Line, Z. Magic, A. M. Mandell, S. Ranjan, D. Charbonneau, M. Clampin, S. Seager, and A. P. Showman, "Infrared Transmission Spectroscopy of the Exoplanets HD 209458b and XO-1b Using the Wide Field Camera-3 on the Hubble Space Telescope," , vol. 774, no. 2, p. 95, Sep. 2013. [Cited on pages 7 and 8.]

D. K. Sing, A. Lecavelier des Etangs, J. J. Fortney, A. S. Burrows, F. Pont, H. R. Wakeford, G. E. Ballester, N. Nikolov, G. W. Henry, S. Aigrain, D. Deming, T. M. Evans, N. P. Gibson, C. M. Huitson, H. Knutson, A. P. Showman, A. Vidal-Madjar, P. A. Wilson, M. H. Williamson, and K. Zahnle, "HST hot-Jupiter transmission spectral survey: evidence for aerosols and lack of TiO in the atmosphere of WASP-12b," , vol. 436, no. 4, pp. 2956–2973, Dec. 2013. [Cited on page 7.]

P. R. McCullough, N. Crouzet, D. Deming, and N. Madhusudhan, "Water Vapor in the Spectrum of the Extrasolar Planet HD 189733b. I. The Transit," , vol. 791, no. 1, p. 55, Aug. 2014. [Cited on page 8.]

I. A. G. Snellen, E. J. W. de Mooij, and A. Burrows, "Bright optical day-side emission from extrasolar planet CoRoT-2b," , vol. 513, p. A76, Apr. 2010. [Cited on pages 8 and 14.]

M. Brogi, R. J. de Kok, S. Albrecht, I. A. G. Snellen, J. L. Birkby, and H. Schwarz, "Rotation and Winds of Exoplanet HD 189733 b Measured with High-dispersion Transmission Spectroscopy," , vol. 817, no. 2, p. 106, Feb. 2016. [Cited on page 8.]

B. Prinoth, H. J. Hoeijmakers, S. Pelletier, D. Kitzmann, B. M. Morris, A. Seifahrt, D. Kasper, H. H. Korhonen, M. Burheim, J. L. Bean, B. Benneke, N. W. Borsato, M. Brady, S. L. Grimm, R. Luque, J. Stürmer, and B. Thorsbro, "Time-resolved transmission spectroscopy of the ultra-hot Jupiter WASP-189 b," , vol. 678, p. A182, Oct. 2023. [Cited on pages 9, 16, and 61.]

A. Lecavelier Des Etangs, D. Ehrenreich, A. Vidal-Madjar, G. E. Ballester, J. M. Désert, R. Ferlet, G. Hébrard, D. K. Sing, K. O. Tchakoumegni, and S. Udry, "Evaporation of the planet HD 189733b observed in H I Lyman-α," , vol. 514, p. A72, May 2010. [Cited on page 10.]

V. Bourrier, A. Lecavelier des Etangs, H. Dupuy, D. Ehrenreich, A. Vidal-Madjar, G. Hébrard, G. E. Ballester, J. M. Désert, R. Ferlet, D. K. Sing, and P. J. Wheatley, "Atmospheric escape from HD 189733b observed in H I Lyman-α: detailed analysis of HST/STIS September 2011 observations," , vol. 551, p. A63, Mar. 2013. [Cited on page 10.]

B. S. Gaudi, S. Seager, and G. Mallen-Ornelas, "On the period distribution of close-in extrasolar giant planets," *The Astrophysical Journal*, vol. 623, no. 1, p. 472, apr 2005. [Online]. Available: https://dx.doi.org/10.1086/428478 [Cited on page 10.]

V. Parmentier, M. R. Line, J. L. Bean, M. Mansfield, L. Kreidberg, R. Lupu, C. Visscher, J.-M. Désert, J. J. Fortney, M. Deleuil, J. Arcangeli, A. P. Showman, and M. S. Marley, "From thermal dissociation to condensation in the atmospheres of ultra hot Jupiters: WASP-121b in context," , vol. 617, p. A110, Sep. 2018. [Cited on page 10.]

H. J. Hoeijmakers, D. Ehrenreich, D. Kitzmann, R. Allart, S. L. Grimm, J. V. Seidel, A. Wyttenbach, L. Pino, L. D. Nielsen, C. Fisher, P. B. Rimmer, V. Bourrier, H. M. Cegla, B. Lavie, C. Lovis, A. B. C. Patzer, J. W. Stock, F. A. Pepe, and K. Heng, "A spectral survey of an ultra-hot Jupiter. Detection of metals in the transmission spectrum of KELT-9 b," , vol. 627, p. A165, Jul. 2019. [Cited on pages 10 and 28.]

F. Borsa, R. Allart, N. Casasayas-Barris, H. Tabernero, M. R. Zapatero Osorio, S. Cristiani, F. Pepe, R. Rebolo, N. C. Santos, V. Adibekyan, V. Bourrier, O. D. S. Demangeon, D. Ehrenreich, E. Pallé, S. Sousa, J. Lillo-Box, C. Lovis, G. Micela, M. Oshagh, E. Poretti, A. Sozzetti, C. Allende Prieto, Y. Alibert, M. Amate, W. Benz, F. Bouchy, A. Cabral, H. Dekker, V. D'Odorico, P. Di Marcantonio, P. Figueira, R. Genova Santos, J. I. González Hernández, G. Lo Curto, A. Manescau, C. J. A. P. Martins, D. Mégevand, A. Mehner, P. Molaro, N. J. Nunes, M. Riva, A. Suárez Mascareño, S. Udry, and F. Zerbi, "Atmospheric Rossiter-McLaughlin effect and transmission spectroscopy of WASP-121b with ESPRESSO," , vol. 645, p. A24, Jan. 2021. [Cited on pages xii, 10, 28, 29, and 81.]

B. Prinoth, H. J. Hoeijmakers, D. Kitzmann, E. Sandvik, J. V. Seidel, M. Lendl, N. W. Borsato, B. Thorsbro, D. R. Anderson, D. Barrado, K. Kravchenko, R. Allart, V. Bourrier, H. M. Cegla, D. Ehrenreich, C. Fisher, C. Lovis, A. Guzmán-Mesa, S. Grimm,

M. Hooton, B. M. Morris, M. Oreshenko, L. Pino, and K. Heng, "Titanium oxide and chemical inhomogeneity in the atmosphere of the exoplanet WASP-189 b," *Nature Astronomy*, vol. 6, pp. 449–457, Jan. 2022. [Cited on pages xi, 10, and 12.]

F. Borsa, M. Rainer, A. S. Bonomo, D. Barbato, L. Fossati, L. Malavolta, V. Nascimbeni, A. F. Lanza, M. Esposito, L. Affer, G. Andreuzzi, S. Benatti, K. Biazzo, A. Bignamini, M. Brogi, I. Carleo, R. Claudi, R. Cosentino, E. Covino, M. Damasso, S. Desidera, A. Garrido Rubio, P. Giacobbe, E. González-Álvarez, A. Harutyunyan, C. Knapic, G. Leto, R. Ligi, A. Maggio, J. Maldonado, L. Mancini, A. F. M. Fiorenzano, S. Masiero, G. Micela, E. Molinari, I. Pagano, M. Pedani, G. Piotto, L. Pino, E. Poretti, G. Scandariato, R. Smareglia, and A. Sozzetti, "The GAPS Programme with HARPS-N at TNG. XIX. Atmospheric Rossiter-McLaughlin effect and improved parameters of KELT-9b," , vol. 631, p. A34, Nov. 2019. [Cited on pages 10 and 28.]

D. Ehrenreich, C. Lovis, R. Allart, M. R. Zapatero Osorio, F. Pepe, S. Cristiani, R. Rebolo, N. C. Santos, F. Borsa, O. Demangeon, X. Dumusque, J. I. González Hernández, N. Casasayas-Barris, D. Ségransan, S. Sousa, M. Abreu, V. Adibekyan, M. Affolter, C. Allende Prieto, Y. Alibert, M. Aliverti, D. Alves, M. Amate, G. Avila, V. Baldini, T. Bandy, W. Benz, A. Bianco, É. Bolmont, F. Bouchy, V. Bourrier, C. Broeg, A. Cabral, G. Calderone, E. Pallé, H. M. Cegla, R. Cirami, J. M. P. Coelho, P. Conconi, I. Coretti, C. Cumani, G. Cupani, H. Dekker, B. Delabre, S. Deiries, V. D'Odorico, P. Di Marcantonio, P. Figueira, A. Fragoso, L. Genolet, M. Genoni, R. Génova Santos, N. Hara, I. Hughes, O. Iwert, F. Kerber, J. Knudstrup, M. Landoni, B. Lavie, J.-L. Lizon, M. Lendl, G. Lo Curto, C. Maire, A. Manescau, C. J. A. P. Martins, D. Mégevand, A. Mehner, G. Micela, A. Modigliani, P. Molaro, M. Monteiro, M. Monteiro, M. Moschetti, E. Müller, N. Nunes, L. Oggioni, A. Oliveira, G. Pariani, L. Pasquini, E. Poretti, J. L. Rasilla, E. Redaelli, M. Riva, S. Santana Tschudi, P. Santin, P. Santos, A. Segovia Milla, J. V. Seidel, D. Sosnowska, A. Sozzetti, P. Spanò, A. Suárez Mascareño, H. Tabernero, F. Tenegi, S. Udry, A. Zanutta, and F. Zerbi, "Nightside condensation of iron in an ultrahot giant exoplanet," , vol. 580, no. 7805, pp. 597–601, Apr. 2020. [Cited on pages 10, 16, and 28.]

J. V. Seidel, D. Ehrenreich, V. Bourrier, R. Allart, O. Attia, H. J. Hoeijmakers, M. Lendl, E. Linder, A. Wyttenbach, N. Astudillo-Defru, D. Bayliss, H. M. Cegla, K. Heng, B. Lavie, C. Lovis, C. Melo, F. Pepe, L. A. dos Santos, D. Ségransan, and S. Udry, "Hot Exoplanet Atmospheres Resolved with Transit Spectroscopy (HEARTS). V. Detection of sodium on the bloated super-Neptune WASP-166b," , vol. 641, p. L7, Sep. 2020. [Cited on pages 10, 28, and 31.]

S. Gandhi, A. Kesseli, I. Snellen, M. Brogi, J. P. Wardenier, V. Parmentier, L. Welbanks, and A. B. Savel, "Spatially resolving the terminator: variation of Fe, temperature, and winds in WASP-76 b across planetary limbs and orbital phase," , vol. 515, no. 1, pp. 749–766, Sep. 2022. [Cited on page 10.]

N. P. Gibson, S. K. Nugroho, J. Lothringer, C. Maguire, and D. K. Sing, "Relative abundance constraints from high-resolution optical transmission spectroscopy of WASP-121b, and a fast model-filtering technique for accelerating retrievals," , vol. 512, no. 3, pp. 4618–4638, May 2022. [Cited on page 10.]

L. Pino, J.-M. Désert, M. Brogi, L. Malavolta, A. Wyttenbach, M. Line, J. Hoeijmakers, L. Fossati, A. S. Bonomo, V. Nascimbeni, V. Panwar, L. Affer, S. Benatti, K. Biazzo, A. Bignamini, F. Borsa, I. Carleo, R. Claudi, R. Cosentino, E. Covino, M. Damasso, S. Desidera, P. Giacobbe, A. Harutyunyan, A. F. Lanza, G. Leto, A. Maggio, J. Maldonado, L. Mancini, G. Micela, E. Molinari, I. Pagano, G. Piotto, E. Poretti, M. Rainer, G. Scandariato, A. Sozzetti, R. Allart, L. Borsato, G. Bruno, L. Di Fabrizio, D. Ehrenreich, A. Fiorenzano, G. Frustagli, B. Lavie, C. Lovis, A. Magazzù, D. Nardiello, M. Pedani, and R. Smareglia, "Neutral Iron Emission Lines from the Dayside of KELT-9b: The GAPS Program with HARPS-N at TNG XX," , vol. 894, no. 2, p. L27, May 2020. [Cited on page 10.]

L. Pino, M. Brogi, J. M. Désert, V. Nascimbeni, A. S. Bonomo, E. Rauscher, M. Basilicata, K. Biazzo, A. Bignamini, F. Borsa, R. Claudi, E. Covino, M. P. Di Mauro, G. Guilluy, A. Maggio, L. Malavolta, G. Micela, E. Molinari, M. Molinaro, M. Montalto, D. Nardiello, M. Pedani, G. Piotto, E. Poretti, M. Rainer, G. Scandariato, D. Sicilia, and A. Sozzetti, "The GAPS Programme at TNG. XLI. The climate of KELT-9b revealed with a new approach to high-spectral-resolution phase curves," , vol. 668, p. A176, Dec. 2022. [Cited on page 10.]

A. C. M. Correia and P. Robutel, "Spin-Orbit Coupling and Chaotic Rotation for Coorbital Bodies in Quasi-circular Orbits," , vol. 779, no. 1, p. 20, Dec. 2013. [Cited on page 10.]

A. Wyttenbach, P. Mollière, D. Ehrenreich, H. M. Cegla, V. Bourrier, C. Lovis, L. Pino, R. Allart, J. V. Seidel, H. J. Hoeijmakers, L. D. Nielsen, B. Lavie, F. Pepe, X. Bonfils, and I. A. G. Snellen, "Mass-loss rate and local thermodynamic state of the KELT-9 b thermosphere from the hydrogen Balmer series," , vol. 638, p. A87, Jun. 2020. [Cited on pages 11, 16, 28, and 45.]

Y. Miguel and L. Kaltenegger, "Exploring Atmospheres of Hot Mini-Neptunes and Extrasolar Giant Planets Orbiting Different Stars with Application to HD 97658b, WASP-12b, CoRoT-2b, XO-1b, and HD 189733b," , vol. 780, no. 2, p. 166, Jan. 2014. [Cited on page 11.]

J. D. Lothringer and T. Barman, "The influence of host star spectral type on ultra-hot jupiter atmospheres," *The Astrophysical Journal*, vol. 876, no. 1, p. 69, may 2019. [Online]. Available: https://dx.doi.org/10.3847/1538-4357/ab1485 [Cited on page 11.]

L. Delrez, A. Santerne, J. M. Almenara, D. R. Anderson, A. Collier-Cameron, R. F. Díaz, M. Gillon, C. Hellier, E. Jehin, M. Lendl, P. F. L. Maxted, M. Neveu-VanMalle, F. Pepe, D. Pollacco, D. Queloz, D. Ségransan, B. Smalley, A. M. S. Smith, A. H. M. J. Triaud, S. Udry, V. Van Grootel, and R. G. West, "WASP-121 b: a hot Jupiter close to tidal disruption transiting an active F star," , vol. 458, no. 4, pp. 4025–4043, Jun. 2016. [Cited on page 11.]

R. G. West, C. Hellier, J. M. Almenara, D. R. Anderson, S. C. C. Barros, F. Bouchy, D. J. A. Brown, A. Collier Cameron, M. Deleuil, L. Delrez, A. P. Doyle, F. Faedi, A. Fumel, M. Gillon, Y. Gómez Maqueo Chew, G. Hébrard, E. Jehin, M. Lendl, P. F. L. Maxted, F. Pepe, D. Pollacco, D. Queloz, D. Ségransan, B. Smalley, A. M. S. Smith, J. Southworth, A. H. M. J. Triaud, and S. Udry, "Three irradiated and bloated hot Jupiters:. WASP-76b, WASP-82b, and WASP-90b," , vol. 585, p. A126, Jan. 2016. [Cited on page 11.]

H. M. Tabernero, M. R. Zapatero Osorio, R. Allart, F. Borsa, N. Casasayas-Barris, O. Demangeon, D. Ehrenreich, J. Lillo-Box, C. Lovis, E. Pallé, S. G. Sousa, R. Rebolo, N. C. Santos, F. Pepe, S. Cristiani, V. Adibekyan, C. Allende Prieto, Y. Alibert, S. C. C. Barros, F. Bouchy, V. Bourrier, V. D'Odorico, X. Dumusque, J. P. Faria, P. Figueira, R. Génova Santos, J. I. González Hernández, S. Hojjatpanah, G. Lo Curto, B. Lavie, C. J. A. P. Martins, J. H. C. Martins, A. Mehner, G. Micela, P. Molaro, N. J. Nunes, E. Poretti, J. V. Seidel, A. Sozzetti, A. Suárez Mascareño, S. Udry, M. Aliverti, M. Affolter, D. Alves, M. Amate, G. Avila, T. Bandy, W. Benz, A. Bianco, C. Broeg, A. Cabral, P. Conconi, J. Coelho, C. Cumani, S. Deiries, H. Dekker, B. Delabre, A. Fragoso, M. Genoni, L. Genolet, I. Hughes, J. Knudstrup, F. Kerber, M. Landoni, J. L. Lizon, C. Maire, A. Manescau,

P. Di Marcantonio, D. Mégevand, M. Monteiro, M. Monteiro, M. Moschetti, E. Mueller, A. Modigliani, L. Oggioni, A. Oliveira, G. Pariani, L. Pasquini, J. L. Rasilla, E. Redaelli, M. Riva, S. Santana-Tschudi, P. Santin, P. Santos, A. Segovia, D. Sosnowska, P. Spanò, F. Tenegi, O. Iwert, A. Zanutta, and F. Zerbi, "ESPRESSO high-resolution transmission spectroscopy of WASP-76 b," , vol. 646, p. A158, Feb. 2021. [Cited on pages 11, 16, 26, 57, and 81.]

M. Lendl, D. R. Anderson, A. Collier-Cameron, A. P. Doyle, M. Gillon, C. Hellier, E. Jehin, T. A. Lister, P. F. L. Maxted, F. Pepe, D. Pollacco, D. Queloz, B. Smalley, D. Ségransan, A. M. S. Smith, A. H. M. J. Triaud, S. Udry, R. G. West, and P. J. Wheatley, "WASP-42 b and WASP-49 b: two new transiting sub-Jupiters," , vol. 544, p. A72, Aug. 2012. [Cited on pages 12 and 45.]

B. S. Gaudi, K. G. Stassun, K. A. Collins, T. G. Beatty, G. Zhou, D. W. Latham, A. Bieryla, J. D. Eastman, R. J. Siverd, J. R. Crepp, E. J. Gonzales, D. J. Stevens, L. A. Buchhave, J. Pepper, M. C. Johnson, K. D. Colon, E. L. N. Jensen, J. E. Rodriguez, V. Bozza, S. C. Novati, G. D'Ago, M. T. Dumont, T. Ellis, C. Gaillard, H. Jang-Condell, D. H. Kasper, A. Fukui, J. Gregorio, A. Ito, J. F. Kielkopf, M. Manner, K. Matt, N. Narita, T. E. Oberst, P. A. Reed, G. Scarpetta, D. C. Stephens, R. R. Yeigh, R. Zambelli, B. J. Fulton, A. W. Howard, D. J. James, M. Penny, D. Bayliss, I. A. Curtis, D. L. Depoy, G. A. Esquerdo, A. Gould, M. D. Joner, R. B. Kuhn, J. Labadie-Bartz, M. B. Lund, J. L. Marshall, K. K. McLeod, R. W. Pogge, H. Relles, C. Stockdale, T. G. Tan, M. Trueblood, and P. Trueblood, "A giant planet undergoing extreme-ultraviolet irradiation by its hot massive-star host," , vol. 546, no. 7659, pp. 514–518, Jun. 2017. [Cited on pages xii, 12, 16, and 38.]

H. J. Hoeijmakers, D. Ehrenreich, K. Heng, D. Kitzmann, S. L. Grimm, R. Allart, R. Deitrick, A. Wyttenbach, M. Oreshenko, L. Pino, P. B. Rimmer, E. Molinari, and L. Di Fabrizio, "Atomic iron and titanium in the atmosphere of the exoplanet KELT-9b," , vol. 560, no. 7719, pp. 453–455, Aug. 2018. [Cited on pages 12 and 16.]

N. W. Borsato, H. J. Hoeijmakers, B. Prinoth, B. Thorsbro, R. Forsberg, D. Kitzmann, K. Jones, and K. Heng, "The Mantis Network. III. Expanding the limits of chemical searches within ultra-hot Jupiters: New detections of Ca I, V I, Ti I, Cr I, Ni I, Sr II, Ba II, and Tb II in KELT-9 b," , vol. 673, p. A158, May 2023. [Cited on page 12.]

D. Deming, S. Seager, L. J. Richardson, and J. Harrington, "Infrared radiation from an extrasolar planet," , vol. 434, no. 7034, pp. 740–743, Mar. 2005. [Cited on page 14.]

N. Madhusudhan, H. Knutson, J. J. Fortney, and T. Barman, "Exoplanetary Atmospheres," in *Protostars and Planets VI*, H. Beuther, R. S. Klessen, C. P. Dullemond, and T. Henning, Eds., Jan. 2014, pp. 739–762. [Cited on page 14.]

R. Alonso, T. Guillot, T. Mazeh, S. Aigrain, A. Alapini, P. Barge, A. Hatzes, and F. Pont, "The secondary eclipse of the transiting exoplanet CoRoT-2b," , vol. 501, no. 3, pp. L23–L26, Jul. 2009. [Cited on page 14.]

F. Rodler, M. Kürster, M. López-Morales, and I. Ribas, "The return of the mummy: Evidence for starlight reflected from the massive hot Jupiter τ Boo b?" *Astronomische Nachrichten*, vol. 334, no. 1-2, p. 188, Feb. 2013. [Cited on page 14.]

J. H. C. Martins, N. C. Santos, P. Figueira, J. P. Faria, M. Montalto, I. Boisse, D. Ehrenreich, C. Lovis, M. Mayor, C. Melo, F. Pepe, S. G. Sousa, S. Udry, and D. Cunha, "Evidence for a spectroscopic direct detection of reflected light from ¡ASTROBJ¿51 Pegasi b¡/ASTROBJ¿," , vol. 576, p. A134, Apr. 2015. [Cited on page 14.]

I. A. G. Snellen, R. J. de Kok, E. J. W. de Mooij, and S. Albrecht, "The orbital motion, absolute mass and high-altitude winds of exoplanet HD209458b," , vol. 465, no. 7301, pp. 1049–1051, Jun. 2010. [Cited on page 15.]

H. J. Hoeijmakers, J. V. Seidel, L. Pino, D. Kitzmann, J. P. Sindel, D. Ehrenreich, A. V. Oza, V. Bourrier, R. Allart, A. Gebek, C. Lovis, S. N. Yurchenko, N. Astudillo-Defru, D. Bayliss, H. Cegla, B. Lavie, M. Lendl, C. Melo, F. Murgas, V. Nascimbeni, F. Pepe, D. Ségransan, S. Udry, A. Wyttenbach, and K. Heng, "Hot Exoplanet Atmospheres Resolved with Transit Spectroscopy (HEARTS) IV. A spectral inventory of atoms and molecules in the high-resolution transmission spectrum of WASP-121 b," *A&A*, vol. 641, p. A123, Sep. 2020. [Cited on page 15.]

S. K. Nugroho, H. Kawahara, K. Masuda, T. Hirano, T. Kotani, and A. Tajitsu, "High-resolution Spectroscopic Detection of TiO and a Stratosphere in the Day-side of WASP-33b," , vol. 154, no. 6, p. 221, Dec. 2017. [Cited on page 16.]

J. L. Birkby, R. J. de Kok, M. Brogi, E. J. W. de Mooij, H. Schwarz, S. Albrecht, and I. A. G. Snellen, "Detection of water absorption in the day side atmosphere of HD 189733 b using ground-based high-resolution spectroscopy at 3.2μm." , vol. 436, pp. L35–L39, Nov. 2013. [Cited on page 16.]

J. L. Birkby, R. J. de Kok, M. Brogi, H. Schwarz, and I. A. G. Snellen, "Discovery of Water at High Spectral Resolution in the Atmosphere of 51 Peg b," , vol. 153, no. 3, p. 138, Mar. 2017. [Cited on page 16.]

N. W. Borsato, H. J. Hoeijmakers, D. Cont, D. Kitzmann, J. Ehrhardt, C. Gössl, C. Ries, B. Prinoth, K. Molaverdikhani, B. Ercolano, H. Kellerman, and K. Heng, "Small but mighty: High-resolution spectroscopy of ultra-hot Jupiter atmospheres with compact telescopes. Transmission spectrum of KELT-9 b with Wendelstein's FOCES spectrograph," , vol. 683, p. A98, Mar. 2024. [Cited on page 16.]

J. V. Seidel, D. Ehrenreich, A. Wyttenbach, R. Allart, M. Lendl, L. Pino, V. Bourrier, H. M. Cegla, C. Lovis, D. Barrado, D. Bayliss, N. Astudillo-Defru, A. Deline, C. Fisher, K. Heng, R. Joseph, B. Lavie, C. Melo, F. Pepe, D. Ségransan, and S. Udry, "Hot Exoplanet Atmospheres Resolved with Transit Spectroscopy (HEARTS). II. A broadened sodium feature on the ultra-hot giant WASP-76b," , vol. 623, p. A166, Mar. 2019. [Cited on pages 16, 19, 26, 39, 72, and 75.]

C. Hellier, D. R. Anderson, K. Barkaoui, Z. Benkhaldoun, F. Bouchy, A. Burdanov, A. Collier Cameron, L. Delrez, M. Gillon, E. Jehin, L. D. Nielsen, P. F. L. Maxted, F. Pepe, D. Pollacco, F. J. Pozuelos, D. Queloz, D. Ségransan, B. Smalley, A. H. M. J. Triaud, O. D. Turner, S. Udry, and R. G. West, "WASP-South hot Jupiters: WASP-178b, WASP-184b, WASP-185b, and WASP-192b," , vol. 490, no. 1, pp. 1479–1487, Nov. 2019. [Cited on pages 16, 42, 44, 45, 47, 48, 51, 53, 55, and 82.]

R. Rodríguez Martínez, B. S. Gaudi, J. E. Rodriguez, G. Zhou, J. Labadie-Bartz, S. N. Quinn, K. Penev, T.-G. Tan, D. W. Latham, L. A. Paredes, J. F. Kielkopf, B. Addison, D. J. Wright, J. Teske, S. B. Howell, D. Ciardi, C. Ziegler, K. G. Stassun, M. C. Johnson, J. D. Eastman, R. J. Siverd, T. G. Beatty, L. Bouma, T. Bedding, J. Pepper, J. Winn, M. B. Lund, J. Villanueva, Steven, D. J. Stevens, E. L. N. Jensen, C. Kilby, J. D. Crane, A. Tokovinin, M. E. Everett, C. G. Tinney, M. Fausnaugh, D. H. Cohen, D. Bayliss, A. Bieryla, P. A. Cargile, K. A. Collins, D. M. Conti, K. D. Colón, I. A. Curtis, D. L. Depoy, P. Evans, D. L. Feliz, J. Gregorio, J. Rothenberg, D. J. James, M. D. Joner, R. B. Kuhn, M. Manner, S. Khakpash, J. L. Marshall, K. K. McLeod, M. T. Penny, P. A. Reed, H. M. Relles, D. C. Stephens, C. Stockdale, M. Trueblood, P. Trueblood, X. Yao, R. Zambelli, R. Vanderspek, S. Seager, J. M. Jenkins, T. J. Henry, H.-S. James, W.-C. Jao, S. X. Wang, P. Butler, I. Thompson, S. Shectman, R. Wittenmyer, B. P. Bowler, J. Horner, S. R.

Kane, M. W. Mengel, T. D. Morton, J. Okumura, P. Plavchan, H. Zhang, N. J. Scott, R. A. Matson, A. W. Mann, D. Dragomir, M. Günther, E. B. Ting, A. Glidden, and E. V. Quintana, "KELT-25 b and KELT-26 b: A Hot Jupiter and a Substellar Companion Transiting Young A Stars Observed by TESS," , vol. 160, no. 3, p. 111, Sep. 2020. [Cited on pages 16, 44, 45, and 47.]

I. Pagano, G. Scandariato, V. Singh, M. Lendl, D. Queloz, A. E. Simon, S. G. Sousa, A. Brandeker, A. Collier Cameron, S. Sulis, V. Van Grootel, T. G. Wilson, Y. Alibert, R. Alonso, G. Anglada, T. Bárczy, D. Barrado Navascues, S. C. C. Barros, W. Baumjohann, M. Beck, T. Beck, W. Benz, N. Billot, X. Bonfils, L. Borsato, C. Broeg, G. Bruno, L. Carone, S. Charnoz, C. Corral van Damme, S. Csizmadia, P. E. Cubillos, M. B. Davies, M. Deleuil, A. Deline, L. Delrez, O. D. S. Demangeon, B. O. Demory, D. Ehrenreich, A. Erikson, A. Fortier, L. Fossati, M. Fridlund, D. Gandolfi, M. Gillon, M. Güdel, M. N. Günther, C. Helling, S. Hoyer, K. G. Isaak, L. L. Kiss, E. Kopp, K. W. F. Lam, J. Laskar, A. Lecavelier des Etangs, D. Magrin, P. F. L. Maxted, C. Mordasini, M. Munari, V. Nascimbeni, G. Olofsson, R. Ottensamer, E. Pallé, G. Peter, G. Piotto, D. Pollacco, R. Ragazzoni, N. Rando, H. Rauer, C. Reimers, I. Ribas, M. Rieder, N. C. Santos, D. Ségransan, A. M. S. Smith, M. Stalport, M. Steller, G. M. Szabó, N. Thomas, S. Udry, J. Venturini, and N. A. Walton, "Constraining the reflective properties of WASP-178b using Cheops photometry," *arXiv e-prints*, p. arXiv:2309.09037, Sep. 2023. [Cited on pages 16, 43, 44, 45, 47, and 83.]

A. M. Silva, J. P. Faria, N. C. Santos, S. G. Sousa, P. T. P. Viana, J. H. C. Martins, P. Figueira, C. Lovis, F. Pepe, S. Cristiani, R. Rebolo, R. Allart, A. Cabral, A. Mehner, A. Sozzetti, A. Suárez Mascareño, C. J. A. P. Martins, D. Ehrenreich, D. Mégevand, E. Palle, G. Lo Curto, H. M. Tabernero, J. Lillo-Box, J. I. González Hernández, M. R. Zapatero Osorio, N. C. Hara, N. J. Nunes, P. Di Marcantonio, S. Udry, V. Adibekyan, and X. Dumusque, "A novel framework for semi-Bayesian radial velocities through template matching," , vol. 663, p. A143, Jul. 2022. [Cited on page 23.]

J. V. Seidel, H. M. Cegla, L. Doyle, M. Lafarga, M. Brogi, S. Gandhi, D. R. Anderson, R. Allart, N. Buchschacher, C. Lovis, and D. Sosnowska, "The hot Neptune WASP-166 b with ESPRESSO II: confirmation of atmospheric sodium," , vol. 513, no. 1, pp. L15–L19, Jun. 2022. [Cited on pages 26, 33, and 75.]

J. V. Seidel, D. Ehrenreich, R. Allart, H. J. Hoeijmakers, C. Lovis, V. Bourrier, L. Pino, A. Wyttenbach, V. Adibekyan, Y. Alibert, F. Borsa, N. Casasayas-Barris, S. Cristiani, O. D. S. Demangeon, P. Di Marcantonio, P. Figueira, J. I. González Hernández, J. Lillo-Box, C. J. A. P. Martins, A. Mehner, P. Molaro, N. J. Nunes, E. Palle, F. Pepe, N. C. Santos, S. G. Sousa, A. Sozzetti, H. M. Tabernero, and M. R. Zapatero Osorio, "Into the storm: diving into the winds of the ultra-hot Jupiter WASP-76 b with HARPS and ESPRESSO," , vol. 653, p. A73, Sep. 2021. [Cited on page 28.]

J. Žák, P. Kabáth, H. M. J. Boffin, V. D. Ivanov, and M. Skarka, "High-resolution Transmission Spectroscopy of Four Hot Inflated Gas Giant Exoplanets," , vol. 158, no. 3, p. 120, Sep. 2019. [Cited on page 31.]

J. V. Seidel, M. Lendl, V. Bourrier, D. Ehrenreich, R. Allart, S. G. Sousa, H. M. Cegla, X. Bonfils, U. Conod, A. Grandjean, A. Wyttenbach, N. Astudillo-Defru, D. Bayliss, K. Heng, B. Lavie, C. Lovis, C. Melo, F. Pepe, D. Ségransan, and S. Udry, "Hot Exoplanet Atmospheres Resolved with Transit Spectroscopy (HEARTS). VI. Non-detection of sodium with HARPS on the bloated super-Neptune WASP-127b," , vol. 643, p. A45, Nov. 2020. [Cited on pages 31 and 39.]

A. Vidal-Madjar, R. Ferlet, C. Gry, and R. Lallement, "Deuterium and the local interstellar cloud (s?)." , vol. 155, pp. 407–412, Feb. 1986. [Cited on page 32.]

W. D. Vacca, M. C. Cushing, and J. T. Rayner, "A Method of Correcting Near-Infrared Spectra for Telluric Absorption," , vol. 115, no. 805, pp. 389–409, Mar. 2003. [Cited on page 32.]

S. Ulmer-Moll, P. Figueira, J. J. Neal, N. C. Santos, and M. Bonnefoy, "Telluric correction in the near-infrared: Standard star or synthetic transmission?" , vol. 621, p. A79, Jan. 2019. [Cited on page 32.]

S. J. Adelman, I. Bikmaev, A. F. Gulliver, and B. Smalley, "Round Table Summary: Instrumentation and Data Processing," in *Modelling of Stellar Atmospheres*, N. Piskunov, W. W. Weiss, and D. F. Gray, Eds., vol. 210, Jan. 2003, p. 337. [Cited on page 32.]

E. Wood, "Telluric line removal in astrophysical spectroscopy," *ASEN/ATOC*, vol. 5235, p. 15, 2003. [Cited on page 32.]

A. Smette, H. Sana, S. Noll, H. Horst, W. Kausch, S. Kimeswenger, M. Barden, C. Szyszka, A. M. Jones, A. Gallenne, J. Vinther, P. Ballester, and J. Taylor, "Molecfit: A general tool for telluric absorption correction. I. Method and application to ESO instruments," , vol. 576, p. A77, Apr. 2015. [Cited on pages 32 and 33.]

W. Kausch, S. Noll, A. Smette, S. Kimeswenger, M. Barden, C. Szyszka, A. M. Jones, H. Sana, H. Horst, and F. Kerber, "Molecfit: A general tool for telluric absorption correction. II. Quantitative evaluation on ESO-VLT/X-Shooterspectra," , vol. 576, p. A78, Apr. 2015. [Cited on page 32.]

J. Remedios, J. Gille, and J. Barnett, "An investigation of the potential of the high-resolution dynamics limb sounder for upper tropospheric and lower stratospheric ozone and water vapour measurements: a minimum performance scenario," *Advances in Space Research*, vol. 27, no. 8, pp. 1479–1482, 2001. [Online]. Available: https://www.sciencedirect.com/science/article/pii/S0273117701002186 [Cited on page 32.]

S. A. Clough, M. W. Shephard, E. J. Mlawer, J. S. Delamere, M. J. Iacono, K. Cady-Pereira, S. Boukabara, and P. D. Brown, "Atmospheric radiative transfer modeling: a summary of the AER codes," , vol. 91, no. 2, pp. 233–244, Mar. 2005. [Cited on page 33.]

L. Rothman, I. Gordon, A. Barbe, D. Benner, P. Bernath, M. Birk, V. Boudon, L. Brown, A. Campargue, J.-P. Champion, K. Chance, L. Coudert, V. Dana, V. Devi, S. Fally, J.-M. Flaud, R. Gamache, A. Goldman, D. Jacquemart, I. Kleiner, N. Lacome, W. Lafferty, J.-Y. Mandin, S. Massie, S. Mikhailenko, C. Miller, N. Moazzen-Ahmadi, O. Naumenko, A. Nikitin, J. Orphal, V. Perevalov, A. Perrin, A. Predoi-Cross, C. Rinsland, M. Rotger, M. Šimečková, M. Smith, K. Sung, S. Tashkun, J. Tennyson, R. Toth, A. Vandaele, and J. Vander Auwera, "The hitran 2008 molecular spectroscopic database," *Journal of Quantitative Spectroscopy and Radiative Transfer*, vol. 110, no. 9, pp. 533–572, 2009, hITRAN. [Online]. Available: https://www.sciencedirect.com/science/article/pii/S0022407309000727 [Cited on page 33.]

L. S. Rothman, I. E. Gordon, Y. Babikov, A. Barbe, D. Chris Benner, P. F. Bernath, M. Birk, L. Bizzocchi, V. Boudon, L. R. Brown, A. Campargue, K. Chance, E. A. Cohen, L. H. Coudert, V. M. Devi, B. J. Drouin, A. Fayt, J. M. Flaud, R. R. Gamache, J. J. Harrison, J. M. Hartmann, C. Hill, J. T. Hodges, D. Jacquemart, A. Jolly, J. Lamouroux, R. J. Le Roy, G. Li, D. A. Long, O. M. Lyulin, C. J. Mackie, S. T. Massie, S. Mikhailenko, H. S. P. Müller,

O. V. Naumenko, A. V. Nikitin, J. Orphal, V. Perevalov, A. Perrin, E. R. Polovtseva, C. Richard, M. A. H. Smith, E. Starikova, K. Sung, S. Tashkun, J. Tennyson, G. C. Toon, V. G. Tyuterev, and G. Wagner, "The HITRAN2012 molecular spectroscopic database," , vol. 130, pp. 4–50, Nov. 2013. [Cited on page 33.]

C. B. Markwardt, "Non-linear Least-squares Fitting in IDL with MPFIT," in *Astronomical Data Analysis Software and Systems XVIII*, ser. Astronomical Society of the Pacific Conference Series, D. A. Bohlender, D. Durand, and P. Dowler, Eds., vol. 411, Sep. 2009, p. 251. [Cited on page 33.]

R. Allart, C. Lovis, L. Pino, A. Wyttenbach, D. Ehrenreich, and F. Pepe, "Search for water vapor in the high-resolution transmission spectrum of HD 189733b in the visible," , vol. 606, p. A144, Oct. 2017. [Cited on page 33.]

R. Allart, L. Pino, C. Lovis, S. G. Sousa, N. Casasayas-Barris, M. R. Zapatero Osorio, M. Cretignier, E. Palle, F. Pepe, S. Cristiani, R. Rebolo, N. C. Santos, F. Borsa, V. Bourrier, O. D. S. Demangeon, D. Ehrenreich, B. Lavie, M. Lendl, J. Lillo-Box, G. Micela, M. Oshagh, A. Sozzetti, H. Tabernero, V. Adibekyan, C. Allende Prieto, Y. Alibert, M. Amate, W. Benz, F. Bouchy, A. Cabral, H. Dekker, V. D'Odorico, P. Di Marcantonio, X. Dumusque, P. Figueira, R. Genova Santos, J. I. González Hernández, G. Lo Curto, A. Manescau, C. J. A. P. Martins, D. Mégevand, A. Mehner, P. Molaro, N. J. Nunes, E. Poretti, M. Riva, A. Suárez Mascareño, S. Udry, and F. Zerbi, "WASP-127b: a misaligned planet with a partly cloudy atmosphere and tenuous sodium signature seen by ESPRESSO," , vol. 644, p. A155, Dec. 2020. [Cited on pages 33 and 57.]

J. R. Barnes, C. A. Haswell, D. Staab, and G. Anglada-Escudé, "The origin of the excess transit absorption in the HD 189733 system: planet or star?" *Monthly Notices of the Royal Astronomical Society*, vol. 462, no. 1, pp. 1012–1028, 07 2016. [Online]. Available: https://doi.org/10.1093/mnras/stw1713 [Cited on page 35.]

F. Borsa and A. Zannoni, "Stellar contributions to the line profiles of high-resolution transmission spectra of exoplanets," , vol. 617, p. A134, Oct. 2018. [Cited on page 35.]

B. W. Carroll and D. A. Ostlie, *An Introduction to Modern Astrophysics*, 2nd ed. Cambridge University Press, 2017. [Cited on page 35.]

N. Espinoza and A. Jordán, "Limb darkening and exoplanets: testing stellar model atmospheres and identifying biases in transit parameters," , vol. 450, no. 2, pp. 1879–1899, Jun. 2015. [Cited on page 36.]

A. G. M. Pietrow and A. Pastor Yabar, "Center-to-limb variation of spectral lines and their effect on full-disk observations," *arXiv e-prints*, p. arXiv:2311.06200, Nov. 2023. [Cited on page 36.]

J. R. Holt, "Spectroscopic Determination of Stellar Rotation," *Astronomy and Astro-Physics (formerly The Sidereal Messenger)*, vol. 12, p. 646, Jan. 1893. [Cited on page 37.]

R. A. Rossiter, "On the detection of an effect of rotation during eclipse in the velocity of the brigher component of beta Lyrae, and on the constancy of velocity of this system." , vol. 60, pp. 15–21, Jul. 1924. [Cited on page 37.]

D. B. McLaughlin, "Some results of a spectrographic study of the Algol system." , vol. 60, pp. 22–31, Jul. 1924. [Cited on page 37.]

A. H. M. J. Triaud, "The Rossiter-McLaughlin Effect in Exoplanet Research," in *Handbook of Exoplanets*, H. J. Deeg and J. A. Belmonte, Eds., 2018, p. 2. [Cited on page 37.]

I. A. G. Snellen, "A new method for probing the atmospheres of transiting exoplanets," *Monthly Notices of the Royal Astronomical Society*, vol. 353, no. 1, pp. L1–L6, 09 2004. [Online]. Available: https://doi.org/10.1111/j.1365-2966.2004.08169.x [Cited on page 37.]

S. Albrecht, I. Snellen, E. de Mooij, and R. Le Poole, "Ground-based detections of sodium in HD 209458b's atmosphere in two data sets," in *Transiting Planets*, F. Pont, D. Sasselov, and M. J. Holman, Eds., vol. 253, Feb. 2009, pp. 520–523. [Cited on page 37.]

N. Casasayas-Barris, E. Pallé, F. Yan, G. Chen, R. Luque, M. Stangret, E. Nagel, M. Zechmeister, M. Oshagh, J. Sanz-Forcada, L. Nortmann, F. J. Alonso-Floriano, P. J. Amado, J. A. Caballero, S. Czesla, S. Khalafinejad, M. López-Puertas, J. López-Santiago, K. Molaverdikhani, D. Montes, A. Quirrenbach, A. Reiners, I. Ribas, A. Sánchez-López, and M. R. Zapatero Osorio, "Is there Na I in the atmosphere of HD 209458b?. Effect of the centre-to-limb variation and Rossiter-McLaughlin effect in transmission spectroscopy studies," , vol. 635, p. A206, Mar. 2020. [Cited on pages 37 and 75.]

D. McNally, “The distribution of angular momentum among main sequence stars,” *The Observatory*, vol. 85, pp. 166–169, Aug. 1965. [Cited on page 37.]

J.-L. Tassoul, *Stellar Rotation*, ser. Cambridge Astrophysics. Cambridge University Press, 2000. [Cited on page 37.]

M. B. Nielsen, L. Gizon, H. Schunker, and C. Karoff, “Rotation periods of 12 000 main-sequence Kepler stars: Dependence on stellar spectral type and comparison with v sin i observations,” , vol. 557, p. L10, Sep. 2013. [Cited on page 37.]

S. Boldt, M. Oshagh, S. Dreizler, M. Mallonn, N. C. Santos, A. Claret, A. Reiners, and E. Sedaghati, “Stellar activity consequence on the retrieved transmission spectra through chromatic Rossiter-McLaughlin observations,” , vol. 635, p. A123, Mar. 2020. [Cited on pages 38 and 39.]

M. Oshagh, N. C. Santos, D. Ehrenreich, N. Haghighipour, P. Figueira, A. Santerne, and M. Montalto, “Impact of occultations of stellar active regions on transmission spectra. Can occultation of a plage mimic the signature of a blue sky?” , vol. 568, p. A99, Aug. 2014. [Cited on page 38.]

J. E. Libby-Roberts, Z. K. Berta-Thompson, J.-M. Désert, K. Masuda, C. V. Morley, E. D. Lopez, K. M. Deck, D. Fabrycky, J. J. Fortney, M. R. Line, R. Sanchis-Ojeda, and J. N. Winn, “The Featureless Transmission Spectra of Two Super-puff Planets,” , vol. 159, no. 2, p. 57, Feb. 2020. [Cited on page 38.]

X. Dumusque, I. Boisse, and N. C. Santos, “Soap 2.0: A tool to estimate the photometric and radial velocity variations induced by stellar spots and plages*,” *The Astrophysical Journal*, vol. 796, no. 2, p. 132, nov 2014. [Online]. Available: https://dx.doi.org/10.1088/0004-637X/796/2/132 [Cited on page 38.]

E. Sedaghati, H. M. J. Boffin, R. J. MacDonald, S. Gandhi, N. Madhusudhan, N. P. Gibson, M. Oshagh, A. Claret, and H. Rauer, “Detection of titanium oxide in the atmosphere of a hot Jupiter,” , vol. 549, no. 7671, pp. 238–241, Sep. 2017. [Cited on page 38.]

N. Espinoza, B. V. Rackham, A. Jordán, D. Apai, M. López-Morales, D. J. Osip, S. L. Grimm, J. Hoeijmakers, P. A. Wilson, A. Bixel, C. McGruder, F. Rodler, I. Weaver, N. K. Lewis, J. J. Fortney, and J. Fraine, “ACCESS: a featureless optical transmission spectrum for WASP-19b from Magellan/IMACS,” , vol. 482, no. 2, pp. 2065–2087, Jan. 2019. [Cited on pages 38 and 39.]

E. Priest, *Magnetohydrodynamics of the Sun*. Cambridge University Press, 2014. [Cited on pages 38 and 39.]

Y. Zhang, I. A. G. Snellen, A. Wyttenbach, L. D. Nielsen, M. Lendl, N. Casasayas-Barris, G. Chaverot, A. Y. Kesseli, C. Lovis, F. A. Pepe, A. Psaridi, J. V. Seidel, S. Udry, and S. Ulmer-Moll, "Transmission spectroscopy of the ultra-hot Jupiter MASCARA-4 b. Disentangling the hydrostatic and exospheric regimes of ultra-hot Jupiters," , vol. 666, p. A47, Oct. 2022. [Cited on page 39.]

M. Steiner, O. Attia, D. Ehrenreich, M. Lendl, V. Bourrier, C. Lovis, J. V. Seidel, S. G. Sousa, D. Mounzer, N. Astudillo-Defru, X. Bonfils, V. Bonvin, W. Dethier, K. Heng, B. Lavie, C. Melo, G. Ottoni, F. Pepe, D. Ségransan, and A. Wyttenbach, "Hot Exoplanet Atmospheres Resolved with Transit Spectroscopy (HEARTS). VIII. Nondetection of sodium in the atmosphere of the aligned planet KELT-10b," , vol. 672, p. A134, Apr. 2023. [Cited on page 39.]

A. W. A. Kippenhahn, Rudolf; Weigert, *Stellar Structure and Evolution*. Springer, 2012. [Cited on page 39.]

L. A. Balona, "Rotational light variations in Kepler observations of A-type stars," *Monthly Notices of the Royal Astronomical Society*, vol. 415, no. 2, pp. 1691–1702, 07 2011. [Online]. Available: https://doi.org/10.1111/j.1365-2966.2011.18813.x [Cited on page 39.]

B. V. Rackham, D. Apai, and M. S. Giampapa, "The Transit Light Source Effect. II. The Impact of Stellar Heterogeneity on Transmission Spectra of Planets Orbiting Broadly Sun-like Stars," , vol. 157, no. 3, p. 96, Mar. 2019. [Cited on page 39.]

H. von Zeipel, "The radiative equilibrium of a rotating system of gaseous masses," , vol. 84, pp. 665–683, Jun. 1924. [Cited on page 39.]

L. B. Lucy, "Gravity-Darkening for Stars with Convective Envelopes," , vol. 65, p. 89, Jan. 1967. [Cited on page 39.]

P. W. Cauley and J. P. Ahlers, "The Effects of Stellar Gravity Darkening on High-resolution Transmission Spectra," , vol. 163, no. 3, p. 122, Mar. 2022. [Cited on page 39.]

Gaia Collaboration et al., "Gaia Data Release 2. Summary of the contents and survey properties," , vol. 616, p. A1, Aug. 2018. [Cited on pages 42, 44, and 47.]

M. Lendl, S. Csizmadia, A. Deline, L. Fossati, D. Kitzmann, K. Heng, S. Hoyer, S. Salmon, W. Benz, C. Broeg, D. Ehrenreich, A. Fortier, D. Queloz, A. Bonfanti, A. Brandeker, A. Collier Cameron, L. Delrez, A. Garcia Muñoz, M. J. Hooton, P. F. L. Maxted, B. M. Morris, V. Van Grootel, T. G. Wilson, Y. Alibert, R. Alonso, J. Asquier, T. Bandy, T. Bárczy, D. Barrado, S. C. C. Barros, W. Baumjohann, M. Beck, T. Beck, A. Bekkelien, M. Bergomi, N. Billot, F. Biondi, X. Bonfils, V. Bourrier, M. D. Busch, J. Cabrera, V. Cessa, S. Charnoz, B. Chazelas, C. Corral Van Damme, M. B. Davies, M. Deleuil, O. D. S. Demangeon, B. O. Demory, A. Erikson, J. Farinato, M. Fridlund, D. Futyan, D. Gandolfi, M. Gillon, P. Guterman, J. Hasiba, E. Hernandez, K. G. Isaak, L. Kiss, T. Kuntzer, A. Lecavelier des Etangs, T. Lüftinger, J. Laskar, C. Lovis, D. Magrin, L. Malvasio, L. Marafatto, H. Michaelis, M. Munari, V. Nascimbeni, G. Olofsson, H. Ottacher, R. Ottensamer, I. Pagano, E. Pallé, G. Peter, D. Piazza, G. Piotto, D. Pollacco, F. Ratti, H. Rauer, R. Ragazzoni, N. Rando, I. Ribas, M. Rieder, R. Rohlfs, F. Safa, N. C. Santos, G. Scandariato, D. Ségransan, A. E. Simon, V. Singh, A. M. S. Smith, M. Sordet, S. G. Sousa, M. Steller, G. M. Szabó, N. Thomas, M. Tschentscher, S. Udry, V. Viotto, I. Walter, N. A. Walton, F. Wildi, and D. Wolter, "The hot dayside and asymmetric transit of WASP-189 b seen by CHEOPS," , vol. 643, p. A94, Nov. 2020. [Cited on page 45.]

A. Deline, M. J. Hooton, M. Lendl, B. Morris, S. Salmon, G. Olofsson, C. Broeg, D. Ehrenreich, M. Beck, A. Brandeker, S. Hoyer, S. Sulis, V. Van Grootel, V. Bourrier, O. Demangeon, B. O. Demory, K. Heng, H. Parviainen, L. M. Serrano, V. Singh, A. Bonfanti, L. Fossati, D. Kitzmann, S. G. Sousa, T. G. Wilson, Y. Alibert, R. Alonso, G. Anglada, T. Bárczy, D. Barrado Navascues, S. C. C. Barros, W. Baumjohann, T. Beck, A. Bekkelien, W. Benz, N. Billot, X. Bonfils, J. Cabrera, S. Charnoz, A. Collier Cameron, C. Corral van Damme, S. Csizmadia, M. B. Davies, M. Deleuil, L. Delrez, T. de Roche, A. Erikson, A. Fortier, M. Fridlund, D. Futyan, D. Gandolfi, M. Gillon, M. Güdel, P. Gutermann, J. Hasiba, K. G. Isaak, L. Kiss, J. Laskar, A. Lecavelier des Etangs, C. Lovis, D. Magrin, P. F. L. Maxted, M. Munari, V. Nascimbeni, R. Ottensamer, I. Pagano, E. Pallé, G. Peter, G. Piotto, D. Pollacco, D. Queloz, R. Ragazzoni, N. Rando, H. Rauer, I. Ribas, N. C. Santos, G. Scandariato, D. Ségransan, A. E. Simon, A. M. S. Smith, M. Steller, G. M. Szabó, N. Thomas, S. Udry, I. Walter, and N. Walton, "The atmosphere and architecture of WASP-189 b probed by its CHEOPS phase curve," , vol. 659, p. A74, Mar. 2022. [Cited on page 45.]

D. K. Sing, J. J. Fortney, N. Nikolov, H. R. Wakeford, T. Kataria, T. M. Evans, S. Aigrain, G. E. Ballester, A. S. Burrows, D. Deming, J.-M. Désert, N. P. Gibson, G. W. Henry, C. M. Huitson, H. A. Knutson, A. Lecavelier Des Etangs, F. Pont, A. P. Showman, A. Vidal-Madjar, M. H. Williamson, and P. A. Wilson, "A continuum from clear to cloudy hot-Jupiter exoplanets without primordial water depletion," , vol. 529, no. 7584, pp. 59–62, Jan. 2016. [Cited on page 45.]

G. Boué, M. Montalto, I. Boisse, M. Oshagh, and N. C. Santos, "New analytical expressions of the Rossiter-McLaughlin effect adapted to different observation techniques," , vol. 550, p. A53, Feb. 2013. [Cited on page 54.]

D. Foreman-Mackey, D. W. Hogg, D. Lang, and J. Goodman, "emcee: The MCMC Hammer," , vol. 125, no. 925, p. 306, Mar. 2013. [Cited on page 55.]

T. O. Husser, S. Wende-von Berg, S. Dreizler, D. Homeier, A. Reiners, T. Barman, and P. H. Hauschildt, "A new extensive library of PHOENIX stellar atmospheres and synthetic spectra," , vol. 553, p. A6, May 2013. [Cited on page 56.]

E. Sedaghati, R. J. MacDonald, N. Casasayas-Barris, H. J. Hoeijmakers, H. M. J. Boffin, F. Rodler, R. Brahm, M. Jones, A. Sánchez-López, I. Carleo, P. Figueira, A. Mehner, and M. López-Puertas, "A spectral survey of WASP-19b with ESPRESSO," , vol. 505, no. 1, pp. 435–458, Jul. 2021. [Cited on pages 57 and 75.]

N. Casasayas-Barris, E. Palle, M. Stangret, V. Bourrier, H. M. Tabernero, F. Yan, F. Borsa, R. Allart, M. R. Zapatero Osorio, C. Lovis, S. G. Sousa, G. Chen, M. Oshagh, N. C. Santos, F. Pepe, R. Rebolo, P. Molaro, S. Cristiani, V. Adibekyan, Y. Alibert, C. Allende Prieto, F. Bouchy, O. D. S. Demangeon, P. Di Marcantonio, V. D'Odorico, D. Ehrenreich, P. Figueira, R. Génova Santos, J. I. González Hernández, B. Lavie, J. Lillo-Box, G. Lo Curto, C. J. A. P. Martins, A. Mehner, G. Micela, N. J. Nunes, E. Poretti, A. Sozzetti, A. Suárez Mascareño, and S. Udry, "The atmosphere of HD 209458b seen with ESPRESSO. No detectable planetary absorptions at high resolution," , vol. 647, p. A26, Mar. 2021. [Cited on page 75.]

T. Kataria, D. K. Sing, N. K. Lewis, C. Visscher, A. P. Showman, J. J. Fortney, and M. S. Marley, "The Atmospheric Circulation of a Nine-hot-Jupiter Sample: Probing Circulation and Chemistry over a Wide Phase Space," , vol. 821, no. 1, p. 9, Apr. 2016. [Cited on page 83.]

M. Zhang, H. A. Knutson, T. Kataria, J. C. Schwartz, N. B. Cowan, A. P. Showman, A. Burrows, J. J. Fortney, K. Todorov, J.-M. Desert, E. Agol, and D. Deming, "Phase Curves of WASP-33b and HD 149026b and a New Correlation between Phase Curve Offset and Irradiation Temperature," , vol. 155, no. 2, p. 83, Feb. 2018. [Cited on page 83.]